From Solvate to Cell: A Molecular Engineering Approach to the Lithium-Sulfur Battery

Dion Hubble

A dissertation

submitted in partial fulfillment of the

requirements for the degree of

Doctor of Philosophy

University of Washington

2019

Reading Committee:

Alex Jen, Chair

Jihui Yang

Lilo Pozzo

Program Authorized to Offer Degree:

Molecular Engineering

University of Washington

Abstract

From Solvate to Cell: A Molecular Engineering Approach to the Lithium-Sulfur Battery

Dion Hubble

Chair of the Supervisory Committee:
Alex K-Y. Jen
Materials Science & Engineering

The lithium-sulfur (Li-S) battery system has been widely lauded as a candidate to replace lithium-ion (Li-ion) technology in weight-critical applications such as electric vehicles, aerospace missions, and personal electronics. The attractiveness of this design comes from its titular active materials, which can theoretically store >2300 Wh/kg in comparison to ~400 Wh/kg for Li-ion. Additionally, sulfur is cheap and earth-abundant, reducing the potential cost and environmental impact of the system. However, despite decades of research, a commercially-competitive Li-S battery remains elusive. This is largely due to functional challenges such as poor conductivity, electrolyte-soluble reaction intermediates, and anode surface passivation, which reduce the capacity, efficiency and cycle life of practical cells. Although many of these issues are specific to Li-S chemistry, contemporary research often borrows heavily from Li-ion conventions in attempting to address them (to varying degrees of success). Alternately, Li-S

battery design may be approached from a “bottom-up” or “rational molecular design” perspective, in which the materials, fabrication techniques, and analytical methods are designed *de novo* based on the unique functional demands of the system.

This doctoral dissertation broadly details my efforts to develop and study free-standing gel electrolytes for the Li-S system, successfully integrate them into working devices, and demonstrate their effect on cell performance. Chapter 1 introduces the motivating factors behind this research, basic Li-S operating principles, and major functional challenges. Chapter 2 reviews the existing literature on Li-S chemistry and cell designs, including common strategies to improve cell performance. Chapter 3 presents the design, fabrication, and electrochemical properties of solvate ionogel (SIG) electrolytes based on solvate ionic liquid Li(G4)TFSI and functional poly(ethylene glycol) methacrylates. Chapter 4 explores the structure-property relationships of SIGs with regards to solvent additives and polymer molecular structures. Chapter 5 details the development of quasi-solid-state (QSS) Li-S battery designs through integration of SIGs into sulfur/carbon composite cathodes and porous polypropylene separators, the electrochemical performance of QSS cells, and the origin of their cycling characteristics. Finally, Chapter 6 summarizes these results and their impact, concluding with suggestions for future research that may build upon the work herein.

TABLE OF CONTENTS

LIST OF FIGURES

LIST OF TABLES

LIST OF COMMON ABBREVIATIONS/SYMBOLS

AIBN – azobisisobutyronitrile

$BETI^-$ – bis(pentafluoroethylsulfonyl)imide

BPO – benzoyl peroxide

CIP – contact ion pair

DME – 1,2-dimethoxyethane, also known as glyme

DOL – 1,3-dioxolane

DSC – differential scanning calorimetry

DSIG – diluted solvate ionogel

DSIL – diluted solvate ionic liquid

DMF – dimethyl formamide

DMSO – dimethyl sulfoxide

DN – Gutmann donor number

EIS – electrochemical impedance spectroscopy

EV – electric vehicle

FSI^- – bis(fluorosulfonyl)imide

G3 – triethylene glycol dimethyl ether, also known as triglyme

G4 – tetraethylene glycol dimethyl ether, also known as tetraglyme

HCE – high-concentration electrolyte

LIB – lithium-ion battery

Li(G4)TFSI – LiTFSI and G4 mixed in a 1:1 molar ratio

LIQ – a liquid mixture of poly(ethylene glycol) dimethyl ether and Li(G4)TFSI

LSB – lithium-sulfur battery

MeCN – acetonitrile

M_n – number-average molecular weight

MW – molecular weight

NMR – nuclear magnetic resonance

OCP – open circuit potential vs Li/Li^+

OE – organic electrolyte, specifically referring to a standard formulation containing 1M LiTFSI in DOL:DME (1:1 v/v) with 1%wt $LiNO_3$

OTf^- – trifluoromethanesulfonate, also known as triflate

P_{3500} – poly(ethylene glycol) dimethacrylate (M_n~3500Da)

P_{750} – poly(ethylene glycol) dimethacrylate (M_n~750Da)

PEG – poly(ethylene glycol)

PF_6^- – hexafluorophosphate

PGSE-NMR – pulsed gradient spin echo nuclear magnetic resonance

PIL – polymeric ionic liquid

PP_{1000} – poly(propylene glycol) dimethacrylate (M_n~1000Da)

PPG – poly(propylene glycol)

PTFE – poly(tetrafluoroethylene), also known as Teflon

PVDF – poly(vinylene difluoride)

PyrTFSIMA – N-[2-(2-(2-(methacryloyloxy)ethoxy)ethoxy)-ethyl]-N-methyl-pyrrolidinium bis(trifluoromethanesulfonyl)imide

QSS – quasi-solid-state

RTIL – room-temperature ionic liquid

SCE – saturated calomel electrode

SEI – solid-electrolyte interphase

SOC – state of charge

SIG – solvate ionogel

SIL – solvate ionic liquid

SS – stainless steel (SUS316L)

SSIP – solvent-separated ion pair

TEGMA – triethylene glycol methyl ether methacrylate

$TFSI^-$ – bis(trifluoromethanesulfonyl)imide

TGA – thermogravimetric analysis

THF – tetrahydrofuran

t_{Li+} - lithium transference number

T_{sc} – time-to-short-circuit

TTFE – 1,1,2,2-tetrafluoroethyl-2,2,3,3-tetrafluoropropyl ether

VTF – Volgel-Tammann-Fulcher

XPS – x-ray photoelectron spectroscopy

XRD – x-ray diffraction

ε – relative dielectric permittivity

κ – ionic conductivity, also known as electrolytic conductivity

σ – electrical conductivity

ACKNOWLEDGEMENTS

Most of this dissertation was written over a period of several weeks, and the research detailed herein was performed over roughly three years. It took me significantly longer, however, to become the person capable of writing this dissertation, and - as a lab-mate once told me – that was the most important part in the end. Unsurprisingly, I required more help with this task than all of the others combined. It would be impossible to acknowledge every metaphorical giant on whose shoulders I have stood; nonetheless, I will try to name a few of the tallest.

Thank you to my advisor Alex Jen and close collaborator Jihui Yang for putting your trust in me and allowing me so many opportunities to grow professionally as well as personally;

Thank you to Sei-Hum Jang for your mentorship and for keeping me grounded;

Thank you to my fellow students Jiaxu Qin, Ray Lin, Ian Murphy, and April Li, who shared the highs and lows of this project with me and materially contributed to many of the experiments discussed in this dissertation;

Thank you to my parents, who have sacrificed so much to afford me the luxury of becoming the first Ph.D. in our family;

Thank you to Doris Hamilton for making my first experience with chemistry a good one, and to all the other teachers who encouraged my love of science;

Thank you to my friends, who have kept me sane despite this decade's best efforts;

And thank you to my wonderful partner Zoe LePard for supporting me endlessly and bringing joy to my life through one of its most difficult parts.

This material is based in part upon work supported by the State of Washington through the University of Washington Clean Energy Institute and *via* funding from the Washington Research Foundation.

This research was conducted with Government support under and awarded by DoD, Air Force Office of Scientific Research, National Defense Science and Engineering Graduate (NDSEG) Fellowship, 32 CFR 168a.

This material is based upon work supported by the Department of Energy, Office of Energy Efficiency and Renewable Energy (EERE), under Award Number DE-EE0007791.

Chapter 1. INTRODUCTION

1.1 Energy Storage and the 21st Century World

In only fifteen short years from 2000-2015, worldwide energy consumption increased by over 40%, from 118 to 168 PWh.[1] The U.S. Energy Information Administration expects this figure to surpass 300 PWh by 2050.[2] As the 21st century continues to unfold, both people and information now travel faster than ever before, and we expect our energy to keep up with us. It's no wonder, then, that the 2019 Nobel Prize in Chemistry was awarded to the pioneers of the lithium-ion battery (LIB), which now powers most electric vehicles (EVs) and portable electronic devices. Lithium-ion cells in their various permutations are by far the fastest-growing secondary (*i.e.* rechargeable) battery technology, and they are second only to lead-acid batteries in terms of raw capacity produced annually.[3] Even with this current dominance, one of their most important potential applications is still developing. The looming specter of global climate change has made the need for grid-integrated renewable energy more apparent by the day. Yet many such sources are available only intermittently *i.e.* when the sun is shining or wind is blowing. Deploying these on a large scale requires networked storage capacity to soak up and release excess power during times of varying demand. Naturally, LIBs are among the best candidates to meet this challenge.

However, while lithium-ion technology continues to build momentum in the business sector, its technological momentum is slowing down. Designs based on the original "rocking chair" concept described in 1985[4] are now approaching their theoretical limit in terms of energy density and specific energy, and the production cost is dominated by raw materials,[3] making a significant price drop unlikely. This is a particularly troubling prospect for grid applications, since storage cost is the primary obstacle preventing large-scale deployment of renewable energy in the

United States.[5] Meanwhile, the U.S. Department of Energy has estimated in their "EV Everywhere" blueprint that widespread adoption of electric vehicles (EVs) will require pack costs at $125/kWh or below. As of 2017, EV pack cost remained at ~$225/kWh, nearly double the target.[3] There are other major concern concerns about LIBs as well, including their safety record[6] and the environmental impact of mining for cobalt and nickel, which are hazardous to extract and limited in abundance.[7]

In response to these concerns, researchers have devoted increasing attention to "beyond-lithium-ion" batteries in the past decade. These designs replace one or both traditional lithium-ion electrodes, which store energy through a reversible intercalation reaction, with higher-capacity materials based on alternative chemistry. This substitution, in theory, increases the total energy density of the cell. Silicon-based anodes have recently grown to prominence for this reason, and appear to be on the verge of replacing graphite as the anode *du jour* in commercial cells.[8] However, it is actually the cathode, not the anode, which contributes the majority of weight to a typical LIB,[9] as well as being the source of rare metal requirements. Therefore, the long-term future of lithium-based energy storage depends significantly on the emergence of a viable cathode replacement.

The lithium-sulfur (Li-S) battery, or LSB, is one possible candidate that may rise to this challenge. Using only the titular elements as electrode materials, the LSB has a theoretical specific energy of 2567 Wh/kg, nearly five times that of a state-of-the-art LIB. Its constituent materials are also earth-abundant and quite cheap as of the time of this writing.[10,11] These qualities make Li-S one of the most attractive batteries for next-generation electric vehicles, with a driving range >400km[12] and pack cost <$100/kWh[13] considered realistically achievable.

1.2 UNDERSTANDING THE LITHIUM-SULFUR BATTERY

In order to explain why LSBs possess so many appealing properties, it is necessary to understand their basic operating principles, which share many characteristics with LIBs but also differ in major ways. It is also helpful to define important performance metrics which describe secondary battery performance and allow comparison amongst various designs.

1.2.1 *Operating Principles*

Although the detailed chemistry of LSBs can be quite complex (see section 1.2.2), their basic principle of charge storage is quite simple. The battery consists of a lithium metal anode (negative terminal) and sulfur cathode (positive terminal), which are directly responsible for storing energy *i.e.* the "active materials." Upon discharge, electrons (e^-) are driven from anode to cathode by a difference in electrochemical potential, which manifests as a voltage (~2.2V). This current may be directed through a load to produce work. Internally, loss of electrons by lithium metal produces lithium ions (Li^+), which dissolve into an electrolyte medium contacting the anode. Meanwhile, electrons are absorbed by sulfur, producing sulfide (S^{2-}) which attracts nearby Li^+ from the electrolyte to form lithium sulfide (Li_2S). Charge neutrality is preserved overall by a net flux of Li^+ through the electrolyte, often traversing a porous separator that prevents physical contact of the active materials. The battery may be recharged by applying an external bias in the opposite direction to reverse these processes, ultimately regenerating elemental sulfur and lithium. Chemically, the overall discharge process may be represented as follows:

(Anode Half-Reaction) $\mathrm{Li} \rightarrow \mathrm{Li}^+ + e^-$

(Cathode Half-Reaction) $\mathrm{S}_8 + 16\mathrm{Li}^+ + 16e^- \rightarrow 8\mathrm{Li}_2\mathrm{S}$

(Overall Reaction) $16\mathrm{Li} + \mathrm{S}_8 \rightarrow 8\mathrm{Li}_2\mathrm{S}$

The anode half-reaction may be calculated to store 3861 mAh/g_{Li}, where a mAh is equal to 3.6 coulombs, or the charge passed by a milliamp of current in one hour. Alternately, this may be expressed as 2062 mAh/cm^3. Similarly, the cathode half-reaction stores 1672 mAh/g_S or 3460 mAh/cm^3. Combining these values and assuming an average discharge voltage of 2.2V yields the theoretical specific energy and theoretical energy density for the LSB: 2567 Wh/kg and 2842 Wh/L, respectively.

Of course, a functioning battery requires more than just active materials, and weight/volume are added by each additional component. The most important of these is the electrolyte, which in LSBs typically consists of a 1M solution of lithium salt – usually lithium bis(trifluoromethanesulfonyl)imide (LiTFSI) – dissolved in an etheric solvent or mixture of solvents - often 1,3-dioxolane (DOL) and 1,2-dimethoxyethane (DME). This electrolyte must thoroughly wet the surface of both electrodes, as well as the aforementioned porous separator, often made of polypropylene and/or polyethylene. Each electrode requires an easy path for current to flow into and out of the battery, and thus metal foils are included as current collectors – copper at the anode and aluminum at the cathode. The latter requires more than just aluminum foil for efficient charge transport, however, as both S_8 and Li_2S are highly insulating materials. Therefore, the cathode is typically formulated as a composite of sulfur particles and conductive carbon additives, which allows current to reach to the electrode surface more easily. This composite also requires a polymer binder to hold individual particles together in a dimensionally stable form. Finally, some exterior packaging is required, although its contribution to the total weight and volume of the battery will vary significantly depending on end-application.

1.2.2 *Mechanism of Sulfur Conversion*

The transformation of sulfur into Li_2S, and vice versa, is referred to in battery parlance as a "conversion" reaction, since the (non-metallic) chemical bonds within each material are completely rearranged during the process. In reality, this conversion does not occur in one step as written above, but instead proceeds through a series of steps in which the S_8 ring is opened and then shortened into chain-like molecules known as lithium polysulfides (Li_2S_x), eventually reaching Li_2S. The longer such variants ($4 \leq x \leq 8$) are well-known for their solubility in polar aprotic solvents such as DOL/DME,[14] and all polysulfides tend to exchange sulfur atoms with one another continuously, a process known as disproportionation.[15] Therefore, at any intermediate state-of-charge (SOC) in an LSB, sulfur atoms may exist simultaneously as a mixture of solid or dissolved S_8, Li_2S, and Li_2S_x of various lengths. The conversion does, however, follow a few identifiable stages, summarized below. Note that the reactions written below are meant to represent general processes rather than suggest or exclude particular species or mechanisms.

(Stage 1)

$$S_8 + 2Li^+ + 2e^- \rightarrow Li_2S_8$$

$$Li_2S_8 + 2Li^+ + 2e^- \rightarrow 2Li_2S_4$$

$$Li_2S_4 + Li_2S_8 \rightarrow 2Li_2S_6$$

In the first stage, solid sulfur is converted into long-chain lithium polysulfides, primarily Li_2S_8 and Li_2S_6. Usually these species will dissolve at least partially into the electrolyte, a process that is driven by lithium exchange between polysulfide and solvent molecules.[16] Because these reactions involve a phase change from solid to liquid (dissolved), the Gibbs phase rule dictates that the equilibrium or open-circuit voltage (OCV) of this process is fixed for a given temperature and pressure. Therefore, stage one can be identified on a plot of voltage vs. capacity as a plateau at ~2.4V.

(Stage 2) $$2Li_2S_6 + 2Li^+ + 2e^- \rightarrow 3Li_2S_4$$

Once elemental sulfur has been exhausted, stage two begins and long-chain polysulfides are further reduced to intermediate lengths, collectively represented here as Li_2S_4. At this point, nearly all sulfur is present as dissolved polysulfides. Therefore, OCV decreases with average sulfur oxidation state, and stage two appears as a sloping region between ~2.1-2.4V. However, this stage is short-lived, as medium-chain polysulfides generally have much lower solubility in non-aqueous electrolytes than the longer variants.

(Stage 3) $$Li_2S_4 + 2Li^+ + 2e^- \rightarrow 2Li_2S_2$$

$$Li_2S_4 + Li_2S_2 \rightarrow 2Li_2S_3$$

$$Li_2S_3 + Li_2S_2 \rightarrow Li_2S + Li_2S_4$$

Stage three marks the end of liquid-liquid conversion as poorly-soluble short-chain polysulfides begin to precipitate out of the electrolyte. Metastable solid Li_2S_2 is the first product to appear, but significant amounts of Li_2S may also form *via* disproportionation reactions, as shown above. An overall phase change is once again occurring, and therefore stage 3 is identified by another, longer plateau at ~2.1V.

(Stage 4) $$Li_2S_2 + 2Li^+ + 2e^- \rightarrow Li_2S$$

Finally, as soluble species are no longer available for reaction, a solid-solid conversion of Li_2S_2 into Li_2S occurs. The kinetics of this reaction are much poorer, however, since neither species is very conductive, and disproportionation is much slower in the solid state. Thus, only Li_2S_2 immediately adjacent to conductive surfaces may be converted. This final stage appears as an additional sloping region below 2.1V.

The same basic processes occur in reverse during charge. However, curiously, the voltage behavior of each stage less clearly identifiable, and often only a single long plateau is observed

until near the end of charge. This is because the solid-state conversion of Li_2S into Li_2S_x is quite slow, and once higher-order species are formed, the reaction proceeds almost entirely through a liquid-solid mechanism where medium-length polysulfides are oxidized to longer chains, which then disproportionate with Li_2S to regenerate the medium chains again. This means that Li_2S is present for almost the entire charge process, and the overall conversion involves two phases, restricting the OCV to a fixed value.

LSB mechanism of operation is graphically summarized in **Figure 1.1**.

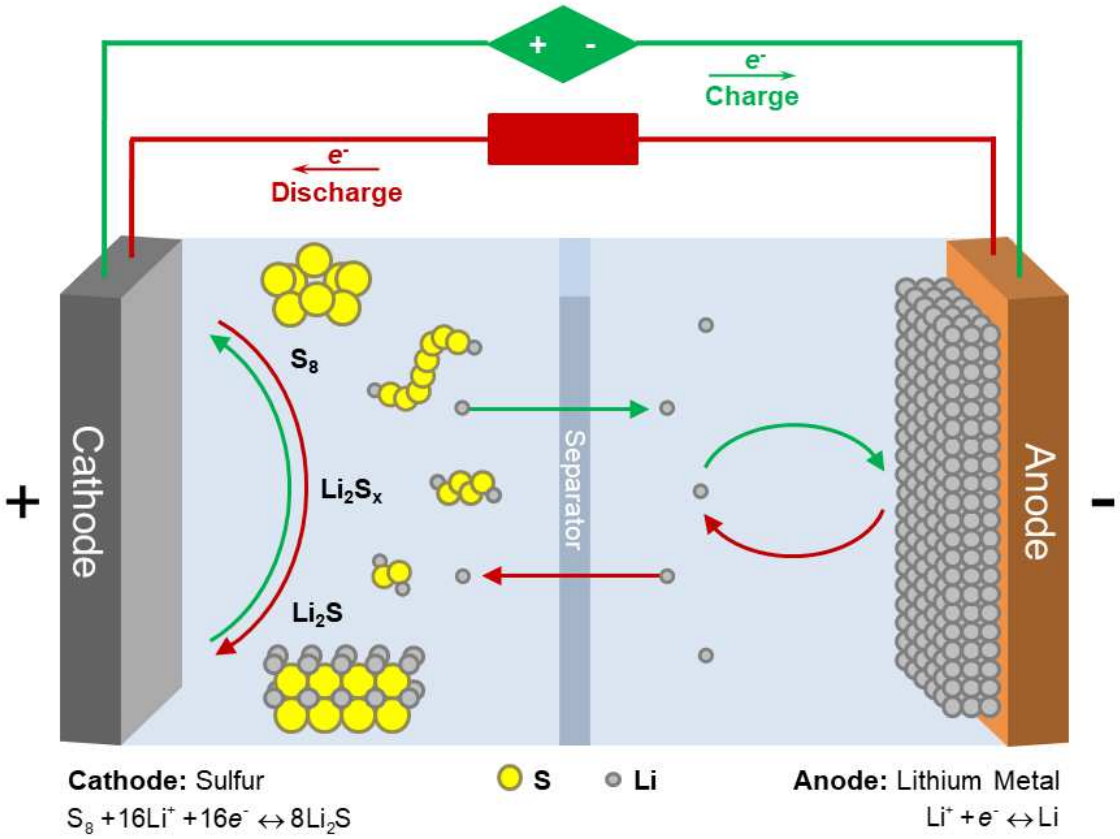

Figure 1.1. Schematic overview of the lithium-sulfur battery.

1.2.3 *Comparison to Lithium-Ion*

The basic construction and overall operation of a LIB is quite similar to a LSB, but the underlying chemistry is very different. The anode active material almost always consists of graphitic carbon, while the cathode active material may be any number of ceramic materials containing lithium. The first-described LIB used $LiCoO_2$ as the cathode, which is still commonly used in consumer electronic batteries, although many other oxides ($LiNi_xMn_yCo_{1-x-y}O_2$, $LiMn_2O_4$, $LiNi_xCo_yAl_{1-x-y}O_2$) may be employed for various applications. Additionally, $LiFePO_4$ is popular in rechargeable power tool batteries where high currents and/or extended longevity are required. All of these cathode materials share two major characteristics: they have redox potentials in the 3.5-4.5V range, along with layered or tunnel-like crystal structures which allow Li^+ to reversibly enter and leave the material in order to balance charge without affecting its structural integrity. This type of charge-storage mechanism is referred to as "intercalation." Charging a LIB forces Li^+ out of the cathode structure and into the electrolyte, where it diffuses to the anode (again through a porous separator) and re-inserts between graphitic carbon layers, now carrying excess negative charge. Graphite can only fit one lithium ion per every hexagonal carbon ring, and only a fraction of total lithium can be removed from the cathode structure without inducing a phase change that destroys the material. The overall chemical reaction[*] is represented below, with $LiCoO_2$ used as an example. Discharging the battery reverses this reaction, as Li^+ de-intercalates from graphite and re-intercalates into the cathode, releasing the stored energy of the reaction as external current.

(Anode Half-Reaction) $$6C + Li^+ + e^- \rightarrow LiC_6$$

(Cathode Half-Reaction) $$LiCoO_2 \rightarrow 0.5Li^+ + 0.5e^- + Li_{0.5}CoO_2$$

[*] As written, $LiCoO_2$ acts as the anode rather than the cathode, since (positive) current is flowing towards it, and vice-versa for graphite. However, battery materials are generally referred to as "cathode" or "anode" materials based on the direction of current flow during *discharge*.

(Overall Reaction) $6C + 2LiCoO_2 \rightarrow LiC_6 + 2Li_{0.5}CoO_2$

A little bit of calculation shows that the anode and cathode can store 372 mAh/g_C (841 mAh/cm^3) and 137 mAh/g_{LCO} (691 mAh/cm^3), respectively. Assuming a potential difference of 3.8V, this LIB has a theoretical specific energy and energy density of 380 Wh/kg and 1441 Wh/L, respectively. Of course, just like in the case of an LSB, a real battery must also include the weight and volume of current collectors, electrolyte, separator, conductive additives, binders, and casings. Nonetheless, the optimization ceiling for LIBs is considerably more limited.

However, LIBs have a major advantage in that the intercalation reactions described above occur in a single step, rather than the complicated multi-step conversion described in Section 1.2.2. Also, unlike elemental sulfur and lithium, LIB active materials are dimensionally-stable throughout battery operation, and therefore the majority of redox-active species are never directly exposed to electrolyte. However, because graphite and $LiCoO_2$ are both semiconductors and solid-state lithium-ion conductors, surface reactive sites are continually refreshed by diffusion, and thus complete utilization is possible. This fundamental difference in reaction mechanism largely explains why the "conventional wisdom" of LIB design *i.e.* fabrication techniques, additives used, interpretation of electrochemical data, *etc.* does not always apply for sulfur-based cell designs.

1.2.4 *Relevant Performance Metrics*

Optimizing battery performance requires a solid definition of what "performance" may entail, and which definition is most relevant to a given situation. For instance, a grid storage application may value longevity over specific energy, since weight is less important to a stationary system, but it must perform predictably for years of continuous use. On the other hand, an aerospace application would likely value these characteristics in the opposite order. **Table 1.1**

contains brief definitions of metrics used to describe LIBs/LSBs and their constituent materials, which will be used hereafter without further explanation.

Table 1.1. Important performance metrics for LIBs/LSBs and their materials, by category.

Active Material/Electrode		
Name	*Units*	*Definition/Explanation*
Specific capacity	mAh/g	Electric charge stored per unit mass. Measured between an upper and lower voltage. Usually shortened to "specific capacity."
Volumetric capacity	mAh/cm^3	Specific capacity multiplied by density.
Open-circuit potential	V	Determined by the electrochemical potentials of redox-involved species at the electrode/electrolyte interface. Often given vs. Li/Li^+. Usually changes with state-of-charge. Anode materials decrease in potential during charge while cathode materials increase, and vice-versa for discharge. Measured potential may differ from this value due to overpotential.
Overpotential	V	Difference between open-circuit potential and potential measured while current is flowing. May be caused by internal resistance ("ohmic"), reaction kinetics ("activation"), or diffusion ("concentration").
Mass loading	mg/cm^2	Mass of electrode material coated onto the current collector per unit area. Higher values reduce the total inactive weight/volume percentage.
Areal capacity	mAh/cm^2	Mass loading multiplied by specific capacity.
Electrical conductivity	S/cm	Inverse of electrical resistivity. Describes the ease with which electric charge passes through a medium.
Electrolyte		
Ionic conductivity	S/cm	Inverse of ionic or electrolytic resistivity. Describes the ease with which charged particles move through a medium. Related to ion diffusion coefficient.
Lithium transference number	unitless	The percentage of total current through an electrolyte that is attributable to the movement of lithium ions.
Full Cell		
Voltage	V	Difference between measured cathode and anode potentials. Current is stopped when voltage exceeds certain limits to prevent side reactions.
Specific energy	Wh/kg	Energy stored per unit weight. Obtained by integrating voltage over specific capacity.
Energy density	Wh/L	Energy stored per unit volume. Obtained by integrating voltage over volumetric capacity
Specific power	W/kg	Specific energy multiplied by C-rate.
Power density	W/L	Energy density multiplied by C-rate.
C-rate	h^{-1}	Current divided by total capacity *i.e.* fully discharging at a C/5 rate would take 5 h, whereas a 5C discharge would take

		12 min. When total capacity is unknown beforehand, C-rate is calculated based on theoretical capacity.
Cycle	unitless	One full charge, followed by one full discharge.
Coulombic efficiency	unitless (%)	Ratio of charge to discharge capacity for a particular cycle.
Capacity retention	unitless (%)	Ratio of discharge capacity for a particular cycle to that of an earlier cycle, usually the first.
Cycle life	unitless (cycles)	The number of cycles completed before capacity retention drops below a target value, often 80%.

1.3 Major Challenges in Lithium-Sulfur Cell Operation

Despite their theoretical promise, commercial development of LSBs has been hampered by the high percentage of inactive materials required for most designs, as well as their notoriously poor cycle life compared to LIBs. These problems can be traced primarily to the complexity of the cathode processes detailed in Section 1.2.2, which introduce design constraints and interdependencies that are not present in LIBs. Lithium metal anodes also present their own set of challenges, both separately and in combination with sulfur cathodes. A successful Li-S cell design must consider all of these challenges and, sooner or later, address them.

1.3.1 *Poor Cathode Conductivity*

As previously mentioned, sulfur and lithium sulfide are electrically insulating and therefore require direct contact with a conductive surface for redox to occur, as opposed to intercalation cathodes which can transport charge through their interiors. This conductive surface must also remain in electrical contact with the current collector *i.e.* an electrical percolation network must be present throughout the cathode. This means that, in practice, sulfur particles must be blended with a large amount of conductive carbon additive, often >50% by weight, for the cathode to function efficiently. High-surface-area carbons such as Ketjen Black are usually preferred. Many designs include carbon nanotubes (CNTs), which help to maintain percolation due to their high

aspect ratio but are quite costly. In contrast, LIB cathodes usually contain <10wt% total additives, including polymer binder.

Even with a large amount of conductive carbon, full electrochemical conversion of S_8 or Li_2S would nearly impossible at room temperature if not for the fact that the lithium polysulfides initially formed are highly soluble (up to 8M atomic sulfur) in typical electrolytes. Once dissolved, they are free to diffuse to the nearest conductive surface for further reaction. They also disproportionate with solid species to bring additional sulfur into solution, thus activating otherwise inactive surfaces. In this way, polysulfides act as a sort of "redox mediator" for S_8, Li_2S, and themselves, transporting electrical charge directly through solution rather than solely through the carbon network (see Section 2.1.2). Of course, having a large concentration of electroactive species in the electrolyte causes major problems of its own, as detailed in Section 1.3.4 below.

1.3.2 *Polysulfide Reactivity*

Thiolate functional groups ($R\text{-}S^-$) are well-known in organic chemistry for being excellent nucleophiles,[17] and polysulfides [$^-S\text{-}(S)_x\text{-}S^-$] share this reactivity. Thus, organic solvents containing electrophilic sites, such as the carbonates widely used in LIBs, are degraded during sulfur cathode operation.[18] Even species that are normally considered "stable," such as fluorinated anions PF_6^- and BF_4^-, may be decomposed in a similar fashion,[19] possibly due to the favorable formation of LiF. The covalent bonds in polysulfides are also relatively weak and dissociate easily,[20] leading to the formation of radical anions such as $LiS_3^{\bullet-}$ during sulfur cathode operation,[21] which may also participate in side reactions. This multifaceted reactivity of Li_2S_x severely limits the choice of electrolyte solvents, salts, and additives appropriate for LSBs.

1.3.3 *Active Material Loss*

Polysulfide dissolution into the electrolyte, although helpful in some respects, also plays a major role in capacity fading for this system. Electrolyte is present not only in the cathode, but throughout the cell, and some Li_2S_x will naturally diffuse away from conductive surfaces where it can no longer contribute to charge storage. This results in a net loss of capacity from the cathode each cycle until an quasi-equilibrium is established, which may not occur until the electrolyte is nearly saturated with polysulfide. Even worse, disproportionation will naturally produce small amounts of insoluble Li_2S and Li_2S_2, which may deposit within the pores of the separator or other non-conductive surfaces, where it is unlikely to be recovered.

1.3.4 *Redox Shuttling of Polysulfides*

Perhaps the best-known performance issue in LSBs occurs when dissolved long-chain polysulfides such as Li_2S_8 diffuse all the way across the cell to the anode surface. There they may react directly with lithium to form insoluble sulfides along with shorter, still-soluble chains, which diffuse back to the cathode and disproportionate to reform the original species. This process, known as a redox shuttle, results in a net transfer of electrons across the cell *i.e.* an internal short-circuit. This "polysulfide shuttle effect" famously results in lower-than-expected coulombic efficiency in LSBs, as some of the current required to recharge the cell instead flows through the short circuit and is lost as heat. Additionally, deposition of sulfides on the anode surface results in permanent lost capacity. If left unchecked, polysulfide shuttling may even become the path of least resistance, and attempting to recharge the cell at this point will result in current being applied indefinitely without any significant change to voltage – the battery is nonfunctional.

1.3.5 *Cathode Passivation by Li_2S*

The Li_2S formed at the end of discharge has quite low solubility in common LSB electrolyte solvents, and therefore precipitates out of solution very quickly. The rate at which this occurs and the morphology of deposits are highly sensitive to current density, electrolyte properties, and many other factors.[22] Since the majority of Li_2S is formed in the vicinity of conductive surfaces, this results in the gradual "covering up" of conductive surface area as discharge progresses. In fact, the transition from Stage 3 to Stage 4 of discharge is often triggered by passivation of the conductive network, rather than the total exhaustion of soluble polysulfides,[23] leaving a significant amount of capacity practically inaccessible. In extreme cases, Li_2S may build up to the point that the pores of the cathode are blocked and Li^+ diffusion becomes physically hindered. This has been implicated as a major source of capacity fading in Li-S pouch cells.[24]

1.3.6 *Volume Change During Conversion*

Volume change of conversion is commonly overlooked in LSB designs. Transforming a given amount of S_8 to Li_2S at room temperature produces a theoretical volume increase of 79%, due to decreased molar density of the sulfide. If adequate pore space is not available for this process, the expansion will force conductive particles apart and weaken the electron percolation network. At best, this will produce increased internal resistance, which may not recover upon recharging if plastic deformation has occurred. At worst, this leads to cracking of the electrode composite and leaves portions of sulfur "stranded" without electrical contact, the associated capacity permanently lost.

Notably, although the cathode active material expands upon discharge, the overall cell volume is actually predicted to decrease, due to the volume of lithium consumed. Cyclical volume changes like this must be considered when packaging a commercial cell.

1.3.7 *Lithium Surface Passivation*

Using lithium metal as an anode material presents its own set of challenges independent from cathode operation. Being the most electropositive element on the periodic table, lithium reacts to some degree with nearly every conceivable electrolyte, resulting in a buildup of decomposition products known as a solid-electrolyte interphase (SEI). This decomposition is self-limiting in suitable electrolytes, as the growing SEI passivates the lithium surface and prevents further reaction. An ideal SEI would be a thin, conformally-coated single-ion conductor and electrical insulator, allowing easy diffusion of Li^+ and nothing else. In practice, however, the SEI is often a porous, uneven layer with inhomogenous composition that does not fully passivate the surface. Furthermore, the ionic nature of the SEI makes it quite brittle in most cases, leading to cracking as lithium metal is stripped or deposited unevenly. The freshly-exposed surface generates additional SEI and, over time, this layer may become quite thick and contribute significantly to internal resistance.

Effective surface passivation becomes especially critical when lithium is paired with a sulfur cathode. A porous/uneven SEI layer enables direct electron transfer to dissolved Li_2S_x, leading to redox shuttling as discussed in Section 1.3.4 above. Insoluble sulfides deposited from this process are also poor ion conductors and contribute to ohmic resistance at the anode.

1.3.8 *Lithium Dendrite Growth*

Dendrite growth is the biggest problem associated with secondary lithium metal batteries and the major reason why alternative anodes like graphite are required for LIBs. The term "dendrite" comes from the Greek word for "tree," referring to the branching, tree-like morphology formed by electroplated lithium during battery charge. Many different metals have been observed to form dendrites under the right conditions, and the mechanism of this process was elucidated in 1990 by J.-N. Chazalviel.[25] In essence, electrodeposition of metal cations removes positive charge from the vicinity of the metal surface faster than anions can migrate away from it. This leads to the development of a local space charge, which favors deposition at highly-curved surfaces where the local electric field is distorted. Unlike most metals, however, lithium surfaces are covered by SEI as detailed above, which may be thinner and/or less resistive in certain spots compared to others. This further concentrates the electric field and promotes dendrite growth.

Dendritic or "mossy" lithium is the source of many different problems in LSBs. For one, growing dendrites may physically puncture the cell separator, creating a sudden short-circuit. This instantly renders the battery useless and may even cause fire or explosion due to localized heating.[26] The inherent safety risk posed by lithium dendrite growth is perhaps the biggest reason why secondary lithium metal batteries have never become popular, despite commercialization as early as the 1980s.[27]

The high surface area of lithium dendrites also promotes additional breakdown of electrolyte and subsequent capacity loss as SEI covers the growing surface. While lithium plating is most favored at dendrite tips, lithium stripping has no such preference and is governed primarily by the resistance of the SEI. This results in "branches" of the tree-like deposit being chopped off at their thinnest points and the formation of so-called dead lithium, which is electrically insulated

on all sides by SEI and excluded from any further reaction.[28] This vicious cycle of dendrite growth and SEI formation contributes to the poor coulombic efficiency and capacity loss than lithium metal anodes are known for – yet another obstacle that impedes the performance of LSBs.

Chapter 2. PROGRESS IN LITHIUM-SULFUR BATTERY RESEARCH

The basic concept of the LSB predates the LIB by almost two decades,[29,30] although the field did not receive sustained interest until the electrochemistry of non-aqueous polysulfide solutions was clarified beginning in the late 1970s.[14,31] By the late 1980s, the modern "standard" Li-S design had taken shape,[32] but its myriad operating challenges allowed it to be overshadowed by still-fledging Li-ion technology. Thus, LSBs were largely relegated to a research curiosity for many years as the vast, untapped potential of LIBs dominated the attention of scientists and engineers. However, due to the advancement of research techniques during the interim, LSBs began to enjoy a revival beginning in the mid-2000s,[33,34] which produced a variety of new, exciting results. This trickle of interest gradually gathered momentum until the field exploded into a major area of research in the 2010s, with hundreds of new papers now published yearly.[35] This chapter briefly reviews the major advancements of the past decade, including those which most-directly inspired the original work presented in this dissertation.

2.1 Improving Sulfur Cathode Performance

2.1.1 *Lithium Polysulfide Trapping/Containment*

Most of the obvious performance issues in LSBs originate from the dissolution of lithium polysulfides into the electrolyte, as detailed in Chapter 1. Therefore, controlling their spatial distribution in the cell, or "polysulfide trapping," has been one of the most active areas of research. Broadly speaking, strategies for polysulfide trapping fall into one of two categories: physical trapping which aims to physically block or hinder the diffusion of polysulfides outside of the cathode, and chemical trapping which uses reversible chemical interactions to accomplish the

same. Both strategies were demonstrated quite effectively by Ji, Li, and Nazar in 2009, who reversibly attained >75% of the theoretical capacity of sulfur (1320 mAh/g) by melting S_8 into the pores of a mesoporous carbon host matrix at 150°C, followed by coating this composite in a thin layer of poly(ethylene glycol) (PEG).[36] Such host matrices not only function as a high-surface-area conductive additive, but also as a sulfur containment mechanism, since Li_2S_x is formed exclusively within the 3-4nm pore spaces of the carbon. Any Li_2S_x which manages to escape this miniature labyrinth encounters polar PEG functionality, which interacts strongly with the charged polysulfides and slows their diffusion.

This early demonstration of polysulfide trapping spawned a huge body of work that has led to many important advancements. Carbon in its various forms remains popular as a physical host matrix for sulfur,[37–41] although many other encapsulation materials such as metal oxides,[42] metal sulfides,[43] rigid polymers,[44] semiconducting polymers,[45,46] and metal-organic frameworks[47] have given positive results. Alternately, single-ion-conducting membranes such as lithiated Nafion have been employed as separators to physically block polysulfides, although this adds significant ohmic resistance to the cell and selectivity is not perfect.[48] However, physical trapping by itself cannot prevent the escape of polysulfides from the cathode during prolonged cycling without total encapsulation, which also blocks access of sulfur to the electrolyte. For this reason, chemical trapping has ultimately proven to be more effective tool for improving the cycle life and capacity of LSBs. PEG continues to enjoy popularity as a binder or additive due to its aforementioned ion-dipole interactions with Li_2S_x, which not only hinders diffusion but may also modify the conversion pathway.[49] Other strongly-polar organic and inorganic functionalities can achieve similar effects by their inclusion in the cathode composite,[50–54] and there have been systematic

studies of the adsorption of polysulfides onto various types of host materials.[55,56] Trapping agents may also be coated onto the separator, creating a sort of "net" to prevent cross-cell diffusion.[57]

Instead of relying on dipole-type interactions, several pioneering strategies have taken advantage of the chemical reactivity of lithium polysulfides to contain them within the cathode structure. For instance, organic functional groups containing thiol, disulfide, or thiosulfate functionality may participate in disproportionation reactions with dissolved Li_2S_x, producing covalently-tethered sulfur chains and/or insoluble Li_2S/Li_2S_2. Such groups may be incorporated *via* binders,[58] separators,[59] or direct functionalization onto a solid host matrix in order to immobilize sulfur upon reaction.[60] Interestingly, the *in-situ* formation of thiosulfate by chemical oxidation of Li_2S_x at an MnO_2 surface has also been reported.[61]

Perhaps the simplest solution to polysulfide dissolution is to simply eliminate liquid electrolyte. All-solid-state LSBs have been constructed using Li^+-conducting ceramics,[62] solid polymer electrolytes,[63] or pure lithium salts,[64] and comprehensive reviews of this field may be found elsewhere.[65] However, these types of designs have three major drawbacks which have kept them from serious commercial consideration. First, solid electrolytes in general tend to have much lower ionic conductivity than liquids at a given temperature, which limits the current density that can be supported by the cell.[66] Second, all-solid cells struggle with high interfacial resistance between particles,[67] which further limits rate and active material utilization. Third, and most critically, the chemical conversion of S_8 into Li_2S proceeds through an entirely different, single-step mechanism in the solid state.[68,69] While this no doubt improves the coulombic efficiency of the process, the kinetics of this reaction are much poorer than polysulfide-mediated conversion in the liquid state due to poor electronic and ionic conductivity for both species. In practice, these drawbacks limit all-solid-state LSBs to either elevated temperature or very slow C-rate operation.

2.1.2 *Conversion Reaction Catalysts / Redox Mediators*

Sulfur utilization is heavily dependent on the ability of dissolved polysulfides to encounter and react at conductive surfaces before diffusion carries them away from these surfaces (*vide supra*). Polysulfide trapping strategies work to increase the timescale of the latter process, but reducing the timescale of the former *i.e.* catalyzing the reaction can be just as effective at improving total capacity, in addition to lowering total cell impedance. Many researchers have therefore developed methods to speed up the rate of conversion at one or more stages.

Electrolyte composition has a large and well-studied effect on both reaction rate and mechanism. For instance, the exchange current density of Li_2S_6 redox is highest in diglyme (diethylene glycol dimethyl ether) out of all common etheric solvents,[70] although this advantage is partially negated by its lower ionic conductivity compared to DOL:DME. Conversion pathway may also be changed entirely by high-donor-number solvents such as dimethyl sulfoxide (DMSO) or dimethyl formamide (DMF) that preferentially stabilize the radical anion $LiS_3^{\bullet-}$,[71,72] from which the conversion to-and-from Li_2S is faster. Unfortunately, these solvents tend to be unstable to lithium metal, which complicates their use in LSBs.

True chemical catalysis – that is, lowering of the activation energy of reaction – is quite difficult to achieve for Li_2S_x redox because substances that bind polysulfides strongly enough to weaken S-S bonds tend to degrade by doing so,[54,56] although recently-reported MgB_2 may prove to be an exception.[73] However, the observed rate of reaction can still be altered by so-called redox mediators. These materials are not true catalysts, as they reversibly oxidize/reduce along with polysulfides during charge/discharge. Instead, they carry charge between conductive surfaces and dissolved sulfur species, effectively turning a heterogeneous reaction into a homogeneous one. Only a catalytic amount of redox mediator is usually required to observe massive improvements

in reaction rate. Substances reported to exhibit this effect include conjugated organic molecules,[74,75] inorganic solids,[61] and soluble lithium salts.[76] Conjugated polymer binders/additives[45,77,78] could be viewed as an extension of this strategy due to the additional sites for charge transfer that they provide.

It is worth noting that polysulfides act as their own redox mediators *via* disproportionation, one of the key mechanisms that allows sulfur conversion to occur on a reasonable timescale. Therefore, direct addition of Li_2S_x to the electrolyte – prior to cell assembly – can be an effective way to prevent capacity fading in LSBs. Not only does this contribute to the total capacity of the cell and reduces round-trip loss of sulfur due to the principle of mass action,[79] but it also improves the overall reaction kinetics, especially when the volume of electrolyte is limited.[41] However, this strategy may only be employed if the lithium anode is sufficiently passivated to prevent redox shuttling (see Section 2.2.2).

2.1.3 *Controlling Insoluble Sulfide Deposition*

As sulfur containment strategies have improved, the issue of cathode passivation by Li_2S has received considerably more attention as a major remaining challenge to LSB commercialization. Many researchers have noted that the Li_2S, an ionic substance, deposits preferentially on polar surfaces as opposed to non-polar carbon. Targeted addition of such surfaces to the cathode can therefore be used to spatially direct Li_2S and delay passivation. Semiconducting oxides have used for this purpose,[23] along with amino-functionalized carbon.[80] The rates of nucleation and growth on carbon may also be manipulated by adjusting the electrolyte polarity and Li^+ diffusion coefficient. Using these principles to deposit an ideal Li_2S architecture, Pan and coworkers recently demonstrated an LSB with exceptional sulfur utilization (>1500 mAh/g_S at C/5

rate), capacity retention (>95% after 100 cycles), coloumbic efficiency (98.6% after 100 cycles), and rate performance (>1300 mAh/g_S at 1C).[22]

Alternately, uncontrolled Li_2S deposition may be avoided by either 1. increasing the solubility of Li_2S in the electrolyte, or 2. providing a redox-mediator with appropriate energy levels. Insoluble sulfides can be stabilized in solution by larger alkali metal cations such as K^+ or Rb^+ (at the cost of long-chain polysulfide solubility)[81] or by ammonium additives that stabilize Li_2S through hydrogen bonding,[82] although the latter is notably unstable to lithium metal. Increased solubility allows Li_2S formed at the carbon surface to diffuse to the nearest existing sulfide deposit before precipitating, which encourages three-dimensional growth rather than two-dimensional surface coverage. Gerber and coworkers recently demonstrated an electrolyte additive based on benzo[ghi]peryleneimide that achieves a similar effect *via* redox mediation.[75] With a potential in the range 1.9-2V vs. Li/Li^+, the additive promotes Li_2S formation in the bulk of the electrolyte, where the sulfide is more likely to encounter an existing deposit and precipitate there instead of on the remaining conductive surface.

2.1.4 *Cathode Architecture and Electrolyte Wetting*

Maintaining a robust and electrolyte-accessible percolation network is imperative to maximize the capacity and cycle life of secondary batteries, especially when faced with a mechanically dynamic redox system like in LSBs. Many researchers have therefore focused on designing cathode architectures specifically well-suited to sulfur, as opposed to merely adapting materials and fabrication techniques from commercial LIB cathodes. These design strategies include layered cathodes[40] and hierarchical nanostructures,[37] as well as composites where sulfur is formed *in-situ* from precursors.[83] An elegant example of this comes from Li and coworkers, who synthesized a carbon-sulfur composite with 90wt% nanoparticulate sulfur using a bottom-up

approach. Freeze-drying an aqueous solution of Na_2S, NaCl, and glucose, followed by carbonization under argon at 750°C yielded a mesoporous graphitic network uniformly doped with sulfide. Subsequent treatment with a $Fe(NO_3)_3$ solution oxidized this sulfide into well-contained nanoparticles of sulfur while simultaneously dissolving the NaCl to form macroporous channels for electrolyte. This ideal architecture allowed the composite to produce 1115 mAh/g_S at an incredible 2C discharge rate, with a capacity decay rate of only 0.039% per cycle over 1000 cycles.[84] Alternately, instead of designing new carbon structures, cathode integrity may be improved by advanced binders. Replacement of the standard poly(vinylene difluoride) (PVDF) with branched and/or highly-polar structures[34,52,85,86] can help to reinforce the cathode structure and resist plastic deformation, as well as distribute electrolyte more evenly to all surfaces. A notable recent example was published by Chen and coworkers, who used high-molecular-weight poly(ethylene oxide) (PEO) doped with a large concentration of LiTFSI as an ionically-crosslinked, swellable binder.[24] This minimized the volume of electrolyte required for homogeneous wetting of active material – a critical aspect of LSB design that was mostly overlooked until recently.

2.1.5 *Sulfur Loading and E/S Ratio*

As LSB performance has continued to improve over the past decade, the general focus of research has gradually shifted from conceptual demonstrations to commercially-relevant cell design. Most early reports focused solely on the chemical underpinnings of sulfur cathode performance, disregarding total mass loading and the weight/volume of excess electrolyte and lithium metal. The implicit assumption seemed to be that these quantities could be trivially optimized in the future, once sulfur conversion was fully mastered. By the mid-2010s, however, it was increasingly clear that this was not the case.[87,88] The weight and volume of electrolyte in

LSBs tends to outweigh active material by several times, due to sulfur's low density and the high porosity required to accommodate conversion. This can negate the energy density and specific energy advantages of Li-S chemistry unless managed properly. A similar mass balance must be considered with the other inactive components of a real cell (current collectors, separator, and casing), which are minimized at higher mass loadings of sulfur. The stark reality of this situation went unnoticed until recently, since LIBs suffer much less seriously from this problem, given the larger weight and density of their active materials.

A whole-cell mass balance suggests that LSB designs must reach an electrolyte/sulfur (E/S) ratio of <3μL/mg in order to compete commercially with LIBs.[41] Yet translating the results obtained in low loading, high E/S designs has proven more difficult than previously assumed. As many recent studies have pointed out, LSB operating mechanisms change significantly under high-loading, lean-electrolyte conditions due to the higher concentrations of Li_2S_x evolved, often reaching saturation. Under these conditions, polysulfide containment takes a backseat to mass transport limitations and electrode surface passivation as the most pressing research issues.[89,90] Any serious contender for a "practical" LSB design must therefore take these issues into account.

2.1.6 *Alternative Cathodes*

Faced with the challenges of LSB design, some researchers have chosen to "think outside the box" by chemically modifying elemental sulfur into related compounds with similar reactivity. Usually, sulfur is reacted at high temperature with an organic monomer or pre-polymer to form a crosslinked network consisting primarily of S-S bonds. For instance, Chung and coworkers reported the radical co-polymerization of molten sulfur with 10-50wt% 1,3-diisopropenylbenzene to form products similar to polymeric sulfur, which were stable indefinitely under ambient conditions.[91] The 10% composite delivered 1100 mAh/g_S at a theoretical C/10 rate with very

stable cycling behavior. Other researchers have reported similar composites of sulfur with trithiocyanuric acid,[92] polyacrylonitrile,[93] and many, many others.[94] In a conceptually-related strategy, several authors have reported that nanoconfined sulfur in microporous (<1 nm) carbon displays substantially different redox behavior, indicative of a solid-state conversion mechanism. This is due to the formation of a metastable S_{2-4} allotrope, which exists as isolated chains that convert directly to and from Li_2S.[95,96] This mechanism completely bypasses lithium polysulfides and their associated design limitations, with solid-state Li^+ diffusion becoming the more pertinent design challenge.

Other researchers, inspired by the high solubility of lithium polysulfides in many solvents, have designed cells around a Li_2S_x catholyte rather than solid sulfur. By limiting the voltage window such that Li_2S_4 is the final discharge product, the conductivity and kinetic issues associated with solid Li_2S can be avoided at the cost of reduced theoretical capacity.[74,97,98] Several reports have also proposed this reaction as part of a flow battery system.[99]

Sulfur is not the only chalcogen which undergoes electrochemical conversion to its lithium salt. Selenium has been investigated as a cathode material due to its theoretical specific capacity of 679 mAh/g, which is still much higher than LIB intercalation cathodes. It also has several major advantages: unlike sulfur, selenium is a metalloid and conducts electrons readily in its pure state. It is also less reactive in its reduced forms, allowing a wider range of electrolytes to be utilized such as the carbonates developed for LIBs. Finally, selenium tends to form chain-like structures upon electrochemical cycling rather than the discrete S_8 rings common to sulfur, which promotes lithiation in a single-step mechanism that avoids polyselenide formation.[100] Although lithium-selenium batteries fall outside the scope of this dissertation, there have been reports of sulfur-selenium solid solutions being applied successfully as cathode active materials in LSBs.[101,102]

These compounds can maintain much of the theoretical capacity of sulfur but with some of the added advantages of selenium, due to its chemical influence on solid structure and the overall redox process.

2.2 Improving Lithium Metal Anode Performance

Lithium metal batteries are one of the most active research fields in energy storage right now due to serious commercial interest from LIB manufacturers. A comprehensive look at lithium anodes could fill an entire book,[27] and reviews on their various aspects abound.[26,103,104] Instead, this chapter will focus primarily on the aspects of lithium metal anode performance that are most relevant to LSBs.

2.2.1 *Controlling Dendrite Growth*

Any secondary lithium battery design must contend with dendrite growth, and LSBs are no exception. As discussed in Section 1.3.8, lithium dendrites form due to a combination of cation depletion and uneven SEI coverage. Dendritic growth leads to capacity fading, poor coulombic efficiency, increased internal resistance, and even safety hazards. This process can be mitigated by 1. physically blocking lithium dendrite growth, 2. decreasing the local current density, 3. buffering space-charge formation, and 4. improving SEI homogeneity. The most successful strategies often include two or more of these elements.

In 2005, Monroe and Newman computationally demonstrated that lithium dendrite growth is physically suppressed by a cell separator or solid electrolyte with shear modulus twice that of metallic lithium (3.4 GPa).[105] This is much larger than most polymers, but well within the range of ion-conducting ceramics – one of the primary motivating factors for research in this field. However, all-solid-state LSBs are largely impractical for the reasons discussed in Section 2.1.1,

making the brute-force strategy less appealing. Of course, a hybrid-electrolyte cell design remains tenable, in which the anode surface is covered by solid electrolyte that gradually gives way to liquid electrolyte in the cathode.[106–108] The success of these designs depends on facile Li^+ transfer between the two electrolyte phases,[109] and the absence of interfacial defects where lithium can penetrate,[110] along with the ever-present issues surrounding Li_2S passivation and kinetics. More recently, Barai and coworkers have recently demonstrated that the shear modulus requirement is not absolute; dendrite growth can be still prevented if the current density at the lithium surface is sufficiently lower than the limiting current density of the electrolyte.[111] The definition of "sufficiently" depends in a complex way on the electrolyte's shear modulus and yield strength of the electrolyte. This reignites hope for solid polymer and polymer gel electrolytes, consisting of lithium salt (usually LiTFSI) dissolved into a polar, coordinating polymer such as PEO, with or without added solvents to facilitate ion transport.[112–116] These types of freestanding electrolytes have major processing advantages over ceramics and can conform to solid surfaces, reducing interfacial resistance and adding toughness.

These results hint at another method of preventing dendrite growth: decreasing the current density at the anode. While lowering the C-rate of the battery obviously accomplishes this, an alternate approach is to increase the active surface area of the anode. Several researchers have achieved this by depositing lithium onto porous conductive templates[117,118] or embedding lithium into ion-conducting matrices.[119,120] This also buffers the cyclic volume change associated with stripping/plating, which is advantageous for long-term cycling stability. However, this strategy must be applied cautiously to LSBs, since increased surface area also means increased opportunity for dissolved Li_2S_x to react at the anode.

One of the most intriguing strategies to combat lithium dendrites is disincentivize space charge formation. Dendrites grow when ionic concentration becomes depleted at the metal surface, which causes large electric fields to develop. Spectator ions, if present, will naturally migrate to areas of localized charge imbalance and build up, thereby neutralizing the space charge and removing the driving force for dendrite growth. This was famously demonstrated by Ding and coworkers using a $CsPF_6$ additive;[121] lithium halide additives (especially LiF) have also been reported.[122] Similarly, immobilizing some fraction of ions at the lithium surface, using either surface-modified nanoparticles[123–125] or polyelectrolytes,[126,127] has proven very effective at disincentivizing dendrite growth. Another successful approach has been to "superconcentrate" the electrolyte solution so that Li^+ is perpentually in excess at the metal surface.[128] On the other hand, a single-ion-conducting electrolyte with a lithium transference number of unity can never form dendrites at all, since anionic species will be physically incapable of migrating away from the metal surface.[129]

A logical outgrowth of this concentrated electrolyte strategy takes the form of room-temperature ionic liquid (RTIL) electrolytes, which may also be referred to simply as "ionic liquids" for clarity. These unique solvents are non-volatile *i.e.* non-flammable, highly conductive ($>10^{-3}$ S/cm at 30°C), electrochemically stable and, importantly, contain high ionic concentrations.[130] Because of this, RTIL solutions of lithium salts have received intense research attention as lithium metal battery electrolytes, both alone[131–136] and in combination with organic solvents,[137,138] as well as catenated to form polymeric ionic liquids (PILs)[139–141] or immobilized as ionogels.[142–144] One of the major drawbacks of RTIL-based electrolytes is that their lithium transference numbers tend to be much lower than traditional organic formulations,[133,145,146] which limits the current density that they can support.[147] True "lithium ionic liquids," which are molten

at room temperature and contains only Li^+ cations, has been reported, but their high viscosity and resultant poor conductivity preclude use in practical cells.[148] The Watanabe group at Yokohama National University in Japan has extensively characterized a series of "solvate ionic liquids" which may address these issues; further discussion may be found in Section 2.3.2.

The above strategies may physically block dendrites or disincentivize their growth, but in order to prevent their formation entirely, one must turn to their source: the lithium-electrolyte interface. Dendrite growth depends on the preexistence of tip-like lithium deposits and other electric-field-concentrating inhomogeneities. If the anode surface is covered with a smooth, dense, high-conductivity SEI, then dendrite growth cannot be initiated. Because the SEI is typically produced *in-situ* from electrolyte breakdown, its composition and morphology can be altered through use of specific additives or lithium salts.[149–153] In particular, additives which form LiF upon breakdown have been demonstrated as particularly beneficial, although the reasons for this are not entirely clear.[154,155] Not all such additives are safe for LSBs, since dissolved polysulfides react irreversibly with many of them, including the popular bis(fluorosulfonyl)imide (FSI^-).[156] Some reports suggest, however, that there are ways to get around this limitation.[157,158] P_2S_5 was first reported as an additive by Lin and coworkers in 2012,[159] but it did not receive much attention until a recent report by Pang and coworkers showing that, in combination with Li_2S_6, it can react with lithium metal to deposit a conformal coating of Li_3PS_4, a well-known superionic conductor.[160] Whether this coating can remain stable in the continual presence of excess Li_2S_x requires further investigation. Many others have chosen to deposit artificial SEIs onto lithium metal prior to cell fabrication, which can act to prevent dendrite growth as well as passivate the surface to reaction with polysulfides (see below).

2.2.2 *Surface Passivation*

Even ignoring the implications for dendrite growth, lithium surface passivation is absolutely critical for secondary LSBs to function (see Sections 1.3.4 and 1.3.7). In fact, a lack of viable passivation strategies may have played a major role in the decline of LSB research during the 1990s and early 2000s.[32] A major breakthrough occurred in 2004 when $LiNO_3$ was first described as an electrolyte additive for LSBs.[161] This simple salt was already known as an additive in LIBs, but proved exceptionally effective at preventing overcharge due to polysulfide redox shuttle. Long-term cycling was now achievable, and $LiNO_3$ quickly became a standard component of LSB electrolytes, which it remains to this day.[162] It's mechanism of action was initially unclear, although Zhang reported in 2012 that it was continuously and irreversibly reduced at the anode surface.[163] This reduction could also occur in the cathode – to the detriment of cell performance – at potentials below 1.6V vs. Li/Li^+, which sets a practical limit on the operating window of LSBs containing this additive. Subsequent work by Xiong and coworkers[164,165] demonstrated that $LiNO_3$ and Li_2S_x work synergistically, co-depositing a smooth, dense layer of mixed oxynitrides and oxysulfides which passivates the surface to further reaction. The nitrate anion may also play a redox-mediator-like role in the cathode,[76] although this is unconfirmed.

Unfortunately, $LiNO_3$ is not a panacea for anode problems, as the produced layer is quite brittle and prone to cracking as the lithium surface shifts underneath, exposing fresh surface for redox shuttling and additional resistive buildup. Moreover, its continuous decomposition generates volatile gasses during cycling, which is a non-starter for vacuum-sealed commercial cells.[166] Therefore, finding a way to remove or replace it is of paramount importance to the future of the field. P_2S_5 was originally reported as an electrolyte additive specifically for LSBs, and initial results were promising, if somewhat superficial.[159] A unique hydrofluoroether (1,1,2,2-

tetrafluoroethyl-2,2,3,3-tetrafluoropropyl ether, or TTFE) has been successfully applied as a cosolvent in LSB electrolytes, and found to exert a beneficial effect on anode passivation.[167,168] This is a rare example of a LiF-forming additive that is unreactive with Li_2S_x in solution.

Some researchers have turned to the "artificial SEI" strategy, quite popular in lithium anode research,[103] to design passivating layers specifically tailored for use in LSBs. For instance, benzo-15-crown-5 has been reported as both an additive and pre-treatment with DOL to form a passivating film with high Li^+ conductivity. Paired with a sulfur cathode, these pre-treated anodes were demonstrated to improve both capacity and coulombic efficiency in the cell.[169] An exciting recent report came from Li and coworkers,[170] who prepared branched sulfur-containing polymers through direct reaction of sulfur with triallylamine, then applied them to the lithium metal surface. The resulting organic/inorganic SEI was smooth and homogeneous, as well as significantly tougher than the salt-like layers formed by Li_2S_x alone. The effect on lithium stripping/plating efficiency was dramatic, with the modified anodes able to cycle indefinitely at 2 mA/cm^2 (with 1-3 mAh/cm^2 total capacity passed per cycle) and an average coloumbic efficiency of 98.6% over 200 cycles. LSBs containing the pre-treated anodes displayed significantly-improved capacity retention from the 10th to 1000th cycles (1143 mAh/g_S to 735 mAh/g_s, or 64%) at 1C.

2.2.3 *Alternative Anodes*

Although lithium metal is foundational to the concept of LSBs, the possibility of alternate anode materials remains a common line of inquiry. Eliminating lithium metal would obviously quell the headache of dendrites and simplify the maintenance of a passivation layer. The major question of such designs is then "Where will the lithium come from?" Unlike LIB cathodes, sulfur does not bring along its own lithium during cell fabrication, and therefore must either be paired with a prelithiated anode, or itself be prelithiated in the form of Li_2S. Indeed, both approaches are

viable, with silicon often being the anode of choice in these systems,[171–174] but as always, there is a loss of energy density with the added weight of the anode material. These strategies mostly fall outside the scope of this dissertation.

2.3 Electrolyte Considerations

As previously covered throughout the above sections, electrolyte composition (lithium salt, additives, solvents and/or cosolvents, liquid or solid, *etc.*) can have a profound effect on nearly every aspect of performance in LSBs. Additionally, the properties and desired distribution of the electrolyte must be considered during fabrication of individual cell components. This section briefly introduces several aspects of electrolyte design that play a major role in the motivation for, and interpretation of, the original research presented in Chapters 3-7 of this dissertation.

2.3.1 *"Sparingly-Solvating" Electrolytes*

Throughout Chapters 1 and 2 so far, it has been assumed that lithium polysulfides must form during charge/discharge and dissolve into the electrolyte, except where this is physically prevented. Since the process is driven by solvation of Li^+ ions,[16] which is necessary *ipso facto* for Li^+ transport through an electrolyte, it was naturally assumed that Li_2S_x dissolution was inevitable from a chemical point of view. However, Park and coworkers demonstrated in 2013 that certain hydrophobic RTIL electrolytes are an exception to this rule, able to support stable cycling of an LSB with 1000x lower solubility for Li_2S_8 than glymes.[156,175] Understanding this phenomenon first requires some background on electrolytes in general.

Thermodynamically, dissolution of a salt requires the total energy of its solvated ions, plus their coordination shells, being lower than the total energy of unbound solvent, plus the salt's lattice energy.[176] Lithium salts often have poor solubility because lithium's small size (0.068nm)

allows it to exert strong electrostatic forces (according to Coulomb's Law), helping it to form tightly-bound lattices. Lithium is also one of the most Lewis-acidic cations for this reason, as it strongly perturbs nearby dipoles and polarizable bonds upon approach. Unlike aqueous solutions, lithium electrolytes cannot depend on water's large dielectric constant to promote charge separation; therefore, in order to dissolve, the requisite lithium salts must contain large, "non-coordinating" anions like hexafluorophosphate (PF_6^-), trifluoromethanesulfonate (OTf^-), or bis(trifluoromethanesulfonyl)imide ($TFSI^-$), which are poor electron donors due to their extensive charge delocalization, and exert only weak electrostatic forces due to their size. $TFSI^-$ has the additional advantage of being awkwardly-shaped, reducing the packing density of its salts, and having a low barrier to rotation around its S-N bonds,[177] providing additional entropic disincentive for crystallization. The resulting lattice structure is quite weak and may be separated by a species more willing to coordinate the metal ion. Thus, lithium electrolyte solvents generally possess high Lewis basicity *i.e.* electron-donating ability in order to stabilize solvated Li^+ through ion-dipole interactions. This is what makes lithium battery chemistry possible, and also explains why lithium polysulfides of the series $Li_2S_{4\text{-}6}$ dissolve so readily in electrolytes: long-chain polysulfide dianions are charge-delocalized[178] and flexible, but also quite polarizable and unhindered from close approach with Li^+, leading them to form mixed-solvation contact ion pairs such as $[(solvent)_xLi]^+[(solvent)_{x\text{-}2}Li(S_x)]^-$ with large enthalpic driving force.[179] Note that both lithium ions must be well-stabilized by solvent coordination for this process to be favorable.

Room-temperature ionic liquids are salts with such low lattice energy that thermal motion at room temperature is enough to destabilize their solid forms, causing them to melt. While thousands of unique cation-anion combinations have been reported to display this behavior, the variants that are relevant to lithium batteries tend to comprise a bulky quaternary ammonium cation

paired with a delocalized anion such as $TFSI^-$. The solvent nature of these liquids is quite unusual, as they lack the strong dipoles common to solvents like DME or DMSO. Instead, they are held together almost entirely by weak coulombic forces and dispersion interactions, the balance of which determines their physical properties.[180] Because RTILs are themselves low-lattice-energy salts, they can dissolve other low-lattice-energy salts like LiTFSI with mild exothermicity,[181] producing electrolytes with ionic conductivity 10^{-4}–10^{-3} S/cm at 30°C – sufficient for most applications. However, $TFSI^-$ is too bulky and weakly-donating[182] to efficiently drive the dissolution of Li_2S_x, creating the unusual situation of a lithium electrolyte with poor polysulfide solubility *i.e.* a "sparingly-solvating" electrolyte for LSBs.

In their initial report, Park *et al.* used an RTIL named N,N-diethyl-N-methyl-N-(2-methoxyethyl)-ammonium bis(trifluoromethanesulfonyl)imide ([DEME][TFSI]) containing 0.64M LiTFSI as a non-solvating LSB electrolyte, achieving capacity retention of ~75% over 100 cycles at C/10 with >97% coulombic efficiency. This is remarkable, considering that no $LiNO_3$ or other anode-passivating additive was required to prevent redox shuttling. Several of the same authors published another report soon afterward, comparing and contrasting battery performance with electrolytes based on several other types of RTILs.[156] They found that the choice of anion played the largest role in battery performance, with FSI^- and BF_4^- ionic liquids causing rapid failure due to side reactions, while $TFSI^-$ ionic liquids cycled stably. RTILs based on the related bis(pentafluoroethylsulfonyl)imide ($BETI^-$) anion showed better coulombic efficiency but worse capacity and retention, which the authors attributed to poor Li^+ transport caused by higher viscosity. Interestingly, a OTf^--based ionic liquid was found to have Li_2S_x solubility roughly 1000x higher than the other RTILs tested – similar to organic electrolytes. In fact, solubility correlated strongly with Gutmann donor number (DN), a quantitative measure of Lewis basicity,[183] which

is controlled primarily by anion structure in RTILs and is larger for those based on OTf^-.[184] This provides additional strong evidence that Li^+ solvation is the driving force for polysulfide dissolution, and that it may be suppressed by electrolytes of low DN. However, it should be noted that Park and coworkers also observed poor rate performance in LSBs based on RTIL electrolytes, even at low mass loadings of sulfur. The reasons are twofold: 1. the high viscosity and low lithium transference number of these electrolytes produces large overpotentials, and 2. non-solvation of Li_2S_x forces conversion to occur primarily in the solid state, which has much poorer kinetics as previously discussed. Additionally, RTILs are significantly more expensive than common organic solvents, making cost a significant drawback to this strategy.

In the same year, another significant report was published on so-called "solvent-in-salt" electrolytes, which contained up to 7 mol LiTFSI per liter solvent (DOL:DME).[185] The concentration of Li^+ in these blends is so high that virtually all of electron-donating oxygen atoms are coordinated to lithium at any given moment. This gives rise to a number of favorable properties including suppressed crystallization and high lithium transference number, in addition to poor solubility for lithium polysulfides, similar to RTILs. Because the basic sites of the solvent are completely "occupied" by existing Li^+, the overall basicity is correspondingly lowered and the electrolyte becomes sparingly-solvating. The authors also noted improved lithium stripping/plating performance, as expected for superconcentrated systems (see Section 2.2.1). Naturally, LSBs with this electrolyte showed enhanced capacity retention and coulombic efficiency, similar to RTIL-based systems. While rate performance was still limited, this report suggested a generalized strategy to produce sparingly-solvating electrolytes without the high cost of RTILs.

Many other research groups took note of these results and developed their own high-concentration electrolytes (HCEs) with other aprotic liquids, particularly observing an improved electrochemical window that allowed otherwise-unsuitable solvents to form stable SEIs on lithium metal.[186,187] Additionally, it was found that HCEs could be diluted with non-basic solvents such as hydrofluoroether TTFE to form "localized high-concentration electrolytes" (LHCEs) with lowered viscosity. Since TTFE does not interact strongly with Li^+, the ion coordination environment of the parent material (and its associated benefits) are mostly retained, meaning that sparingly-solvating electrolytes for LSBs could be realized without the correspondingly-poor ion transport.[188] As an example, the 2:1 molar ratio blend of MeCN:LiTFSI with TTFE diluent has been demonstrated as a high-conductivity, low-Li_2S_x-solubility electrolyte by the Nazar and Balasubramanian groups.[189,190] However, the best-studied (L)HCEs belong to a class of materials known as "solvate ionic liquids," which have developed into an independent field of their own right (see below).

2.3.2 *Solvate Ionic Liquids*

The concept of a solvate ionic liquid (SIL) can be traced to a 2004 report by Pappenfus and coworkers, who noted that 1:1 molar combinations of LiTFSI or LiBETI with tetraglyme (G4) yielded liquids with extraordinary thermal stability, indicating strongly-bound Li^+-solvent complexes.[140] Previous studies on tri- and tetraglyme for LIB applications had indicated formation of solid, crystalline solvates with other non-coordinating lithium salts, where Li^+ is chelated by the glymes similarly to crown ethers.[191–193] However, Li(G4)TFSI and Li(G4)BETI were liquids at or near room temperature, with Li(G4)TFSI remaining liquid down to its glass transition at -61°C. Furthermore, the ionic conductivity of this mix was measured to be $>10^{-3}$ S/cm at 30°C, surprisingly large for such a concentrated solution. These properties, unusual for organic

electrolytes but typical for RTILs, led the authors to deem Li(G4)TFSI an ionic liquid for all intents and purposes.

Tamura *et al.* from the Watanabe group at Yokohama National University confirmed that this ionic-liquid-like behavior was also generalizable to 1:1 molar combinations of LiTFSI with triglyme (G3) and a number of alkylated G3/G4 derivatives, all of which were liquids at 25°C.[194] Thermal gravimetric analysis (TGA) experiments revealed negligible glyme evaporation up to 200°C, while differential scanning calorimetry (DSC) showed no discernable features at the melting points of the pure solvents, suggesting that no "free" glyme was present in the mixtures. Furthermore, measurement of self-diffusion coefficients revealed nearly identical values for both Li^+ and solvent, suggesting that they exist entirely as a bound complex *i.e.* $[Li(glyme)]^+$ (**Figure 2.1**). Finally, the authors observed enhanced anodic stability of Li(G3/G4)TFSI (4.7V vs. Li/Li^+) relative to $Li(G3/G4)_{20}TFSI$ (4V vs. Li/Li^+), again suggesting that the oxygen atoms of the solvent are completely occupied by coordination to Li^+ in the equimolar complex and therefore comparatively electron-deficient. Inspired by a contemporary review of molten salt electrolytes,[195] researchers from this group popularized the term "solvate ionic liquid" to describe such mixtures.[196] Further experimental[196–200] and computational[200–202] work has confirmed that Li^+ forms long-lived (~10^{-4} s) 1:1 complexes with G3 or G4, driven by the chelate effect, which are the preferred form of both species.

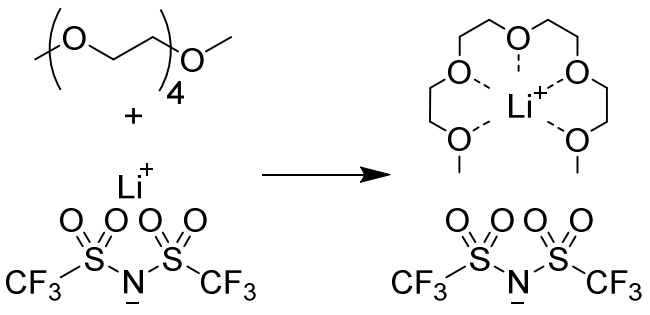

Figure 2.1. Formation of solvate ionic liquid Li(G4)TFSI from equimolar G4 and LiTFSI.

What makes SILs distinct from the broader class of HCEs? Fundamentally, in order to be considered an SIL, the cation-solvent complex of an HCE must have well-defined stoichiometry and be stable with respect to ligand exchange – simply put, the lifetime of individual solvates must be longer than the timescale of their diffusion.[197] If this condition is met, ion transport is best described by the co-diffusion of solvates and counterions, rather than the diffusion of individual ions through a neutral solvent medium. In this framework, the combination of LiTFSI with Lewis base G4 to yield Li(G4)TFSI is analogous to the combination of 1-butyl-3-methylimidazolium (BMIM) fluoride with Lewis acid phosphourous pentafluoride to yield $BMIMPF_6$, both liquids at room temperature that contain negligible uncharged species. SILs therefore display another characteristic behavior of RTILs, which is high ionicity *i.e.* a large proportion of total ions contribute to charge transport as opposed to being "locked away" as neutral ion pairs.[203] When RTILs are diluted with solvents, their ionicities tend to decrease rather than increase as expected by concentrated solution theory.[204] SILs display the same trend with concentration: the ionicity of LiTFSI-G4 blends reaches a maximum at 2.75M, corresponding to 1:1 salt:solvent stoichiometry.[198] Notably, not all lithium salts that are soluble in G3/G4 up to a 1:1 molar ratio produce SILs, even when above their melting temperatures; ionic-liquid-like properties only emerge with counterions that are sufficiently non-coordinating.[196,205] SILs are not limited to lithium salts, as Na^+- and K^+-based,[206] or even Al^{3+}-based systems have been reported which fit the above criteria.[207,208]

Lithium SILs, which can provide the benefits of RTILs without their high cost, have been investigated for a wide range of different battery roles, including but not limited to stand-alone electrolytes in LIBs,[147,209–212] non-volatile solid electrolyte fillers,[213] and of course, LSBs. Dokko and coworkers found that, analogous to other RTILs based on $TFSI^-$, Li(G4)TFSI and Li(G3)TFSI

possessed Li_2S_8 solubilities <100mM$_S$ (atomic sulfur concentration) at 30°C, and could support stable cycling of LSBs with >97% coulombic efficiency.[214] In contrast, electrolytes containing a 4:1 molar ratio of glyme:Li^+ exhibited rapid capacity fading and severe overcharge behavior after only 30 cycles. Importantly, these authors noted that addition of 4 molar equivalents TTFE diluent to Li(G4)TFSI increased the ionic conductivity nearly four times to 5.2×10^{-3} S/cm while decreasing Li_2S_8 solubility roughly six times. The ratio of Li^+ to G4 diffusion coefficients remained unity, suggesting that the $[Li(G4)]^+$ solvate structure was unaffected by TTFE. Using this diluted solvate ionic liquid (DSIL) in LSBs improved the specific capacity of LSBs by ~100mAh/g$_S$ and their coulombic efficiency by ~0.5% relative to Li(G4)TFSI alone, as well as supporting improved rate performance due to faster ion transport. Later work by the same[209] and different[215] labs confirmed these results. Ueno and coworkers further reported that these findings could be generalized to SILs based on LiBETI, but that similar HCE mixtures based on $LiNO_3$, LiOTF, and $LiBF_4$ were unsuitable and produced rapid capacity decay in LSBs.[216] Finally, Zhang and coworkers used Li(G4)TFSI to demonstrate an important design principle for LSBs with sparingly-solvating electrolytes: conductive carbon matrices should be chosen with maximum specific pore volume, rather than maximum specific surface area.[217] Unlike with traditional ether-based systems, where dissolved polysulfides must diffuse to conductive surfaces for reaction, sparingly-solvating systems rely on solid-state, in-place conversion of sulfur deposited on carbon walls. Since the transport of Li^+ through these layers can be quite slow, minimizing their thickness *i.e.* increasing pore space allows better conversion of sulfur and thus, higher capacity. Clearly, Li(G4)TFSI has potential to enable LSBs with competitive performance; however, as all of the above results were obtained from cathodes with ≤1 mg$_S$/cm^2 loading, significant work remains to be done in optimizing cell designs based on this electrolyte.

Chapter 3. SOLVATE IONOGEL ELECTROLYTES WITH FAST ROOM-TEMPERATURE LITHIUM TRANSPORT

Sections of this chapter were adapted or reproduced from the associated publication[218] with permission from the Royal Society of Chemistry.

3.1 INTRODUCTION

3.1.1 *Motivation*

As outlined in Chapter 2, solvate ionic liquids (SILs) possess a unique combination of physical and electrochemical properties which make them imminently suited to tackle performance issues in LSBs. In particular, Li(G4)TFSI – having an ionic conductivity 1.6×10^{-3} S/cm at 30°C,[194] Li_2S_x solubility <100mM$_S$ for all polysulfide lengths,[214] thermal stability up to 200°C,[198] and liquid range down to -54°C[196] – appears especially promising for a sparingly-soluble cathode design. This electrolyte may also help to mitigate dendrite growth at the lithium metal anode, given the ability of HCEs to resist space-charge formation (see Section 2.2.1). Finally, unlike traditional RTILs, Li(G4)TFSI can be produced cheaply and easily from tetraglyme (G4) and LiTFSI, both of which are already manufactured at-scale.

However, despite a handful of reports on its use in LSBs, many questions remain to be answered before a realistic assessment of Li(G4)TFSI can be made for this system. For instance, many reports have touted a high lithium transference number (t_{Li+}) of 0.5 in Li(G4)TFSI[196] as a major advantage over traditional RTIL electrolytes. This number is produced from the self-diffusion coefficients of individual ions (Equation 3.1), as measured by pulsed gradient spin echo nuclear magnetic resonance (PGSE-NMR) experiments:

$$t_{Li^+,NMR} = \frac{D_{Li^+}}{D_{TFSI^-} + D_{Li^+}} \quad (3.1)$$

This theoretical transference number provides insight into ion transport, but does not predict real-life behavior as it assumes that every ion contributes to current flow. In reality, ion motion in RTILs is highly correlated due to formation of ion pairs and/or aggregates, and it is therefore vital to measure t_{Li+} directly, using electrochemical means. Only scant information on this topic is available for Li(G4)TFSI,[147,219] and conclusions are conflicting.

Additionally, although the reported ionic conductivity of Li(G4)TFSI meets the "acceptable" standard for LIBs (>10^{-3} S/cm), high-energy-density batteries necessitate higher currents, and it is therefore desirable to increase conductivity further. Ueno *et al.* have reported immense changes to conductivity by diluting SILs with small amounts of inert solvents, which lower viscosity but do not compete with G4 for Li^+.[220] However, only a handful of solvents were investigated, most of them incompatible with lithium metal anodes.

A major "hidden" challenge of RTIL electrolytes concerns their high viscosity and high interfacial energy with nonpolar surfaces,[221] which can lead to poor wetting of porous cathodes and separators.[222] One method to address this problem is to replace the liquid electrolyte with a free-standing ionogel, where the RTIL is immobilized in a chemically-compatible, rigid network. Gel networks provide an additional "molecular handle" with which to adjust electrolyte properties, and they can also improve anode performance by adding mechanical strength to resist dendrite growth. However, only a few ionogels based on Li(G4)TFSI – so-called solvate ionogels or SIGs – have been reported,[223–225] and their conductivities are uniformly lower than 10^{-3} S/cm. Furthermore, these reports disagree regarding the effect of gel network on Li^+ transport. Research from the Watanabe group has focused on "inert" polymers such as poly(methyl methacrylate) due to their finding that poly(ethylene glycol) (PEG) decreases t_{Li+} in the final material.[226] On the

other hand, D'Angelo and Panzer measured the exact opposite effect: SIGs based on PEG were found to have larger t_{Li+} than those based on poly(methyl methacrylate) or neat Li(G4)TFSI itself.[225] Notably, both studies compared transference numbers based solely on PGSE-NMR, and the molecular weights of PEG used in both studies were vastly different (~10kDa vs. 450Da). It would be beneficial to include PEG in an LSB electrolyte due to its effects on cathode chemistry (see Section 2.1.1), but clearly, a better understanding of lithium transport in SIGs is required before they may be successfully implemented.

3.1.2 *Rationale and Overview*

In order to better understand Li^+ transport mechanisms in SIGs and evaluate their suitability for LSBs, here I report a series of novel SIG designs, each prepared from Li(G4)TFSI immobilized in chemically-crosslinked poly(ethylene gycol) dimethacrylate (PEGDMA). In order to probe the relationship between structural motifs and cell-relevant properties, the design was iteratively altered through variation of PEG length and addition of functionalized co-monomers, as well as slight dilution with an appropriate solvent to produce a "diluted solvate ionogel" (DSIG). Not only do these alterations produce amongst the highest room-temperature conductivities and lithium transference numbers ever reported for ionogel electrolytes – in addition to excellent Li stripping/plating performance – but they also suggest a mechanistic rationale for transport behavior in PEG/Li(G4)TFSI systems which could resolve seeming contradictions in literature. Hence, this report represents a first step towards free-standing electrolytes for lithium secondary cells, including LSBs, with truly competitive performance.

3.2 EXPERIMENTAL METHODS

3.2.1 *Materials*

Poly(ethylene glycol) dimethacrylate (P_{750}, average M_n~750Da, Sigma-Aldrich), triethylene glycol monomethyl ether methacrylate (TEGMA, Sigma-Aldrich), poly(ethylene glycol) (6 mmol hydroxyl end groups, M_n ~3350, Sigma-Aldrich), benzyol peroxide (BPO, reagent grade, ≥98%, Sigma-Aldrich), azobisisobutyronitrile (AIBN, 98%, Sigma-Aldrich), acetonitrile (99.9%, extra dry, anhydrous, Fisher), methanol (HPLC, Fisher), hexanes (99%, mixture of isomers, Fisher) and dichloromethane (≥99%, Fisher) were used as-recieved. Methacryloyl chloride (97%, Sigma-Aldrich) was stored in a freezer with an airtight seal and distilled over CaH_2 under N_2 before use. Tetraethylene glycol dimethyl ether (G4, ≥99%, Aldrich) and 1,4-dioxane (≥99%, Fisher) were dried with 4Å molecular sieves and stored in an argon-atmosphere glovebox (Vacuum Technology Inc, <0.01ppm H_2O and O_2) prior to use. LiTFSI was purchased from 3M and dried at 120°C under Ar, then stored/used in an argon-atmosphere glovebox. Lithium chips (99.9%, 15.6mm diameter, 0.45mm thickness) were purchased from MTI Corp and stored/used in an argon atmosphere glove box. N-[2-(2-(2-(Methacryloyloxy)ethoxy)ethoxy)-ethyl]-N-methyl-pyrrolidium bis(trifluoromethanesulfonyl)imide (PyrTFSIMA) was synthesized according to literature on similar analogs.[143] All methacrylates and radical initiators were stored in a freezer between uses.

3.2.2 *Preparation of Li(G4)TFSI*

LiTFSI was weighed into a glass beaker inside of an argon-atmosphere glove box, then an equimolar amount of G4 was gradually added with stirring and mild heating. Complete dissolution occurred within several hours, resulting in a clear, viscous liquid, which was subsequently dried

under Ar at 120°C for 12 hours, then under vacuum for an additional 12 hours, then stored in an argon-atmosphere glovebox.

3.2.3 *Synthesis of PEGDMA 3500*[†]

To a stirred solution of poly(ethylene glycol) (10.05 g, 6 mmol hydroxyl end groups, M_n ~3350) dissolved in 40 mL anhydrous acetonitrile was dropwise added freshly distilled methacryloyl chloride (1.76 mL, 18 mmol) at 0°C under an argon atmosphere. The mixture was left stirring at 0°C for 30 min, then gently heated at 40°C for 8 hours. The excess methacryloyl chloride was quenched by addition of methanol and the volatiles were removed by rotary evaporation to give the crude product, which was then dissolved in dichloromethane and precipitated by addition of hexanes. The solid was collected by filtration and again dissolved in dichloromethane, followed by addition of activated carbon. The mixture was stirred at room temperature under nitrogen atmosphere for 2 hours. After removal of activated carbon, the solution was again precipitated by addition of hexanes, and filtered to give an off-white powder of P_{3500} (8.72 g). The product was stored in a freezer and used within 1 month of synthesis.

3.2.4 *Gel Fabrication*

BPO powder was dissolved in 1,4-dioxane in the amount of 3-5%mol relative to the methacrylate content of the desired gel formula; alternately, an identical concentration of AIBN was dissolved in dichloromethane. Polymerizable molecules, Li(G4)TFSI, and initiator solution (BPO/dioxane for SIG 1, AIBN/DCM for SIGs 2-5) were sequentially added in appropriate amounts to a glass vial followed by vigorous stirring to ensure homogeneity. The resulting solution was then vacuum dried with stirring at room temperature for 2-3 hours, in order to remove solvent.

[†] The synthesis and purification of PEGDMA 3500 was performed by Francis Lin.

For DSIG 5, an appropriate amount of 1,4-dioxane was then re-added under argon. This precursor solution was transferred to a mold consisting of soda-lime glass plates (Colorado Concept Coatings) treated with siliconizing agent (Aquaphobe CM, Gelest) and separated by two hollow rectangular Kapton films measuring 5 mils (~128μm) each. The mold was sealed shut using permanent magnets over both ends, then transferred into an oven at 80°C for 6 hours to cure the ionogel, followed by cooling overnight. For all gels except DSIG 5, the top plate of the mold was then removed, and the exposed gel was vacuum dried for a minimum of 48 hours to remove any traces of solvent remaining. Finally, circular samples of varying diameter were cut from the gel using stainless steel hollow punches and stored in clean glass petri dishes. All of the above operations were performed in an argon-atmosphere glove box. All ionogels appeared as transparent, flexible films of approximately 0.25mm thickness. Average film height for each batch of gel was measured using an optical laser microscope (Olympus OLS41).

3.2.5 *Electrochemical Property Measurements*

In order to measure ionic conductivity, 7mm diameter gel samples were sandwiched between 15.5mm diameter stainless steel discs and connected to a Gamry 5000E Interface potentiostat/galvanostat *via* flat clip. Galvanostatic electrochemical impedance spectroscopy was performed (RMS 10μA) at frequencies ranging from 100kHz to 100Hz, with output voltage measured by the instrument. Resulting data (**Figure 3.1**) were fitted to an appropriate equivalent circuit (**Figure 3.2**) using Gamry EChem Analyst software, and the limiting resistance at high frequency (R_{bulk}) converted to bulk ionic conductivity using the thickness (l) and cross-sectional area (A) of the sample (**Equation 3.2**).

$$\kappa = \frac{l}{R_{bulk} A} \tag{3.2}$$

Several independent measurements were averaged to produce the reported values (**Table 3.1**). Small air bubbles, trapped between the samples and electrodes, were a frequent source of error despite efforts to eliminate them. Other sources of error may include: slight deviations from average height for individual samples, slight contractions in height due to the pressure necessary for electrical contact, slight temperature variation between measurements, and (for DSIG 5) variations in dioxane content between samples.

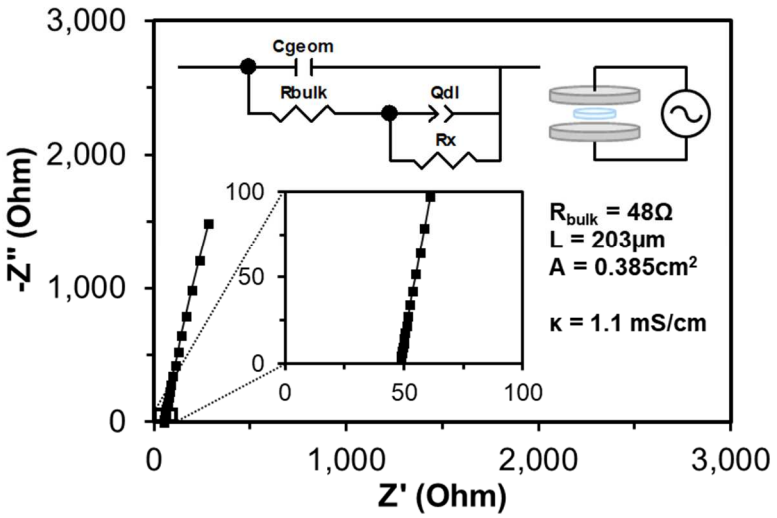

Figure 3.1. Nyquist plot of impedance data (10kHz-100Hz) for a SIG 2 sample.

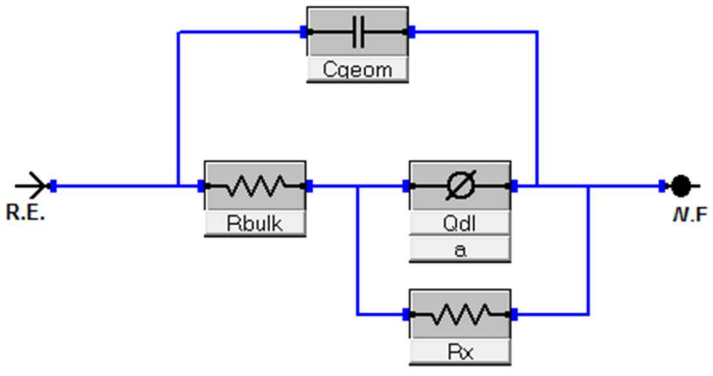

Figure 3.2. Equivalent circuit used to fit impedance data for conductivity measurements.

In order to measure lithium transference number (t_{Li+}), lithium symmetric cells were assembled. Lithium chips were gently polished inside of an argon-atmosphere glovebox using 320 grit followed by 600 grit sandpaper (Norton T414 Blue-Bak) to remove excessive surface oxidation and ensure consistency between samples. The lithium chips were then pressed onto stainless steel discs. A 19mm diameter gel separator (or Whatman GF/C separator with 80µL liquid electrolyte) was inserted between the chips, and the whole assembly placed into CR2032 coin cells (Pred Materials) which were sealed using an electric crimping machine (MTI Corp). In order to measure t_{Li+} of gels, the Evans-Vincent-Bruce method was followed,[227] with galvanostatic impedance spectra (100kHz-0.1Hz, RMS 10µA) collected before and after a potentiostatic polarization of 5mV for 6 hours performed on a Gamry 5000E Interface potentiostat/galvanostat. Polarization and impedance spectroscopy was performed again following this to ensure reproduceability, and this second set of data was used for calculations. Impedance spectra were fitted to a two-semicircle Randles model (with constant phase elements modeling non-ideal capacitive processes) in series with a constant phase element to model the low-frequency diffusive region (**Figure 3.3**).

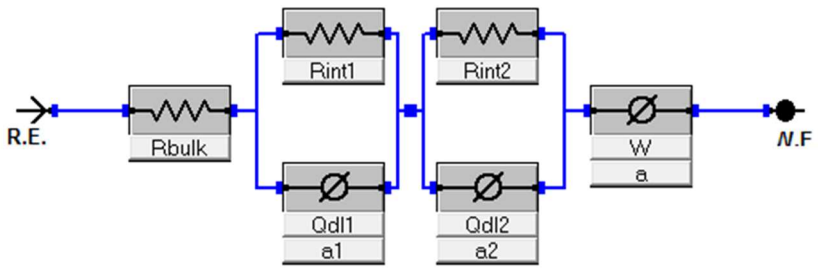

Figure 3.3. Equivalent circuit used to fit symmetric cell impedance data.

For each spectrum, high-frequency real intercept was subtracted from low-frequency real intercept to obtain total interfacial resistance (R_i). The polarization voltage (ΔV), initial

interfacial resistance ($R_{i,o}$), interfacial resistance after steady-state current was attained ($R_{i,ss}$), initial current (i_o), and steady-state current (i_{ss}) were plugged into **Equation 3.3** to determine t_{Li+}.

$$t_{Li^+} = \frac{i_{ss}(\Delta V - R_{i,o} i_o)}{i_o(\Delta V - R_{i,ss} i_{ss})} \tag{3.3}$$

3.2.6 *Lithium Stripping/Plating Experiments*

Lithium symmetric cells were prepared as above, then either galvanostatically polarized at 0.1 mA/cm^2 (time-to-short-circuit) or cycled between ±0.1 mA/cm^2 at 3-hour intervals (stripping/plating) using an Arbin LBT ±5V-200mA battery testing system, and data collected using the included MITS Pro software. A short circuit was considered to have formed when an abrupt, sustained (>5hrs) drop in voltage was observed.

3.2.7 *Physical Property Measurements*

TGA experiments were performed under flowing N_2 gas (50mL/min) using a Shimadzu TGA-50 Thermogravimetric Analyzer. Samples (8-10mg) were transferred into pre-weighed aluminum pans in an argon-atmosphere glove box, then weighed on a microbalance and loaded into the instrument within ~1 minute. Samples were then heated at 10°C/min to 80°C, held for 15 minutes to drive off any superficial moisture absorbed during transfer, then heated at 10°C/min to 120°C and held for two hours while weight loss was recorded. DSC thermograms were recorded under flowing N_2 gas (50mL/min) using a liquid-nitrogen-cooled Shimadzu DSC-60 Plus Differential Scanning Calorimeter. Samples (3-5mg) were transferred into aluminum pans and covered, then cooled to below -110°C at -10°C/min. Samples were held at this temperature for 10 minutes, then warmed to 100°C at 10°C/min, resulting in the reported curves.

Uniaxial compression testing was performed using an Instron 5585H test frame equipped with a 50N load cell. 14mm diameter gel samples (thickness determined by a micrometer) were

placed between PTFE platens and compressed to 1N applied force at a strain rate of 5μm/min. Response was linear (elastic) for all samples and compression was repeated until slopes converged, the final measurement being reported as elastic modulus. Then, samples were compressed to 50N at 25μm/min and the resulting stress-strain curves plotted.

3.2.8 *Raman Spectroscopy*

Raman spectra were collected at ~23°C between 500-1600cm^{-1} on a Renishaw InVia Raman Microscope (785nm laser, 0.5cm^{-1} resolution), and data analysis was performed with Renishaw WiRE 3.4 software. Samples of Li(G4)TFSI ("SIL"), dioxane, and 5:1 + 1:1 volumetric combinations of the two, respectively, were analyzed on a cleaned silicon substrate. In order to normalize signals to Li(G4)TFSI concentration, the 1125-1150cm^{-1} region was fit with two curves (~1139cm^{-1} and ~1128cm^{-1}) to represent signals from G4 and dioxane, respectively, neither of which show much dependence on Li^+ coordination state.[228,229] The intensity of the peak at 1139cm^{-1} was then normalized between all samples, and the resulting data plotted.

3.3 RESULTS AND DISCUSSION

3.3.1 *Comparison Between Formulas*

Five unique compositions of ionogel were fabricated (SIGs 1-5), each containing 80 vol% of liquid electrolyte with 20 vol% polymerizable components (~17 wt% polymer). This ratio was chosen to be well above the minimum gelation point[225] and provides a good balance of mechanical integrity with ionic concentration. The formula-specific constituents (**Figure 3.4**) were stirred together with a small amount of radical initiator to form transparent, homogeneous solutions, which were then cured at 80°C for 6h in a glass mold, causing methacrylate groups to polymerize and form a crosslinked network (**Figure 3.5**). This process produced thin, freestanding gel films which could be handled and die-cut into circular samples of any desired diameter (**Figure 3.6**), which were used to test ionic conductivity κ, potentiostatic-polarization-based t_{Li+}, and compressive elastic modulus E of SIGs 1-5 in a climate controlled (23±1°C) laboratory room. Results are summarized in **Table 3.1**.

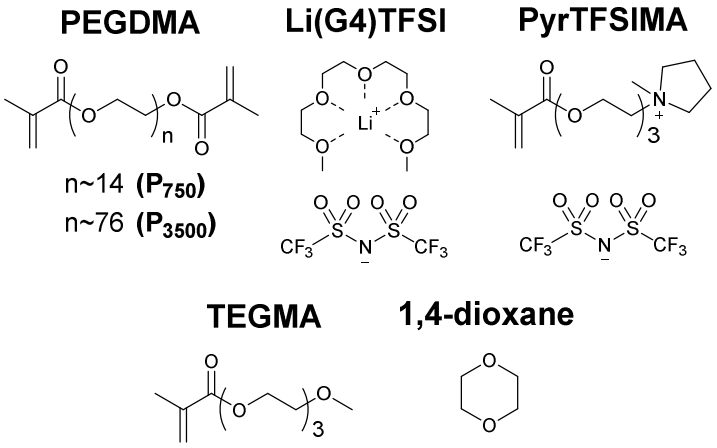

Figure 3.4. Structures/abbreviations of molecules used to form SIGs.

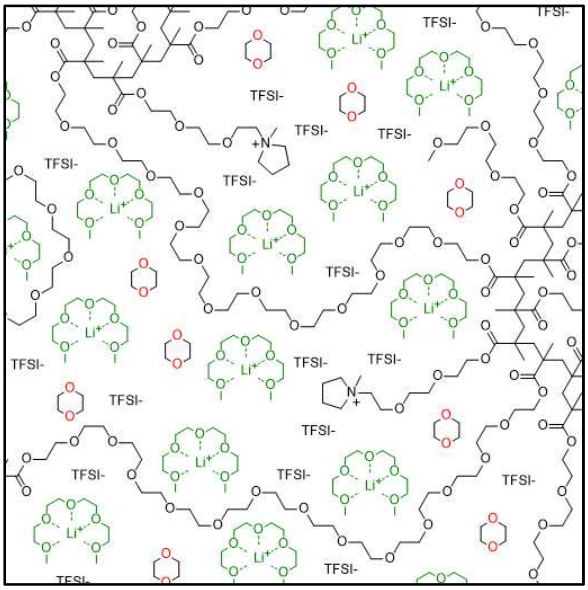

Figure 3.5. Schematic snapshot of SIG molecular structure, showcasing the interplay between solid and liquid components.

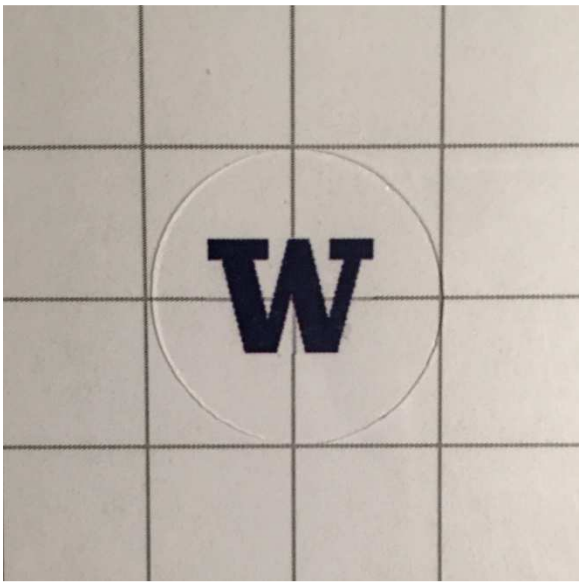

Figure 3.6. Photograph of a typical 19mm diameter x 0.25mm thick SIG sample.

Table 3.1. Composition of five novel SIGs and their measured properties at room temperature (23°C), along with neat SIL for comparison.

Formula	Composition [vol % added]						Properties		
	P_{750}	P_{3500}	TEGMA	PyrTFSIMA	Li(G4)TFSI	Dioxane	E [kPa]	t_{Li+}	κ [mS/cm]
SIL	0%	0%	0%	0%	100%	0%	**n/a**	**0.13**	**1.08**
SIG 1	20%	0%	0%	0%	80%	0%	**369**	**0.21**	**0.73**
SIG 2	0%	20%	0%	0%	80%	0%	**254**	**0.28**	**1.05**
SIG 3	0%	10%	10%	0%	80%	0%	**249**	**0.24**	**0.92**
SIG 4	0%	10%	0%	10%	80%	0%	**401**	**0.16**	**1.07**
(D)SIG 5	0%	20%	0%	0%	66.6%	13.3%	**228**	**0.57**	**2.15**

Elastic modulus, important for cell integrity and also linked directly to lithium deposition morphology,[230] ranged 228-401 kPa for our materials, similar to other PEG-based gel electrolytes. While variation between formulas is relatively minor, the differences are simple to correlate with composition. Elongation of polymer chain length from PEGDMA M_n~750 (P_{750}) to PEGDMA M_n~3500 (P_{3500}) produces a decrease in stiffness between SIGs 1 and 2, consistent with larger molecular weight between crosslinks.[231] Replacing half of this P_{3500} with chemically-similar tri(ethylene glycol) methyl ether methacrylate (TEGMA) in SIG 3 does not appear to significantly alter the modulus, while incorporating a small amount of cyclic ether 1,4-dioxane (DSIG 5) produces only a minor decrease. This can be explained by a slight reduction in overall solvent quality for PEG[232,233] for which dioxane is a theta solvent[234] while Li(G4)TFSI is a theta-good solvent.[235] The introduction of ionic-liquid-like pendant group PyrTFSIMA (N-[2-(2-(2-(methacryloyloxy)ethoxy)ethoxy)-ethyl]-N-methyl-pyrrolidium bis(trifluoromethanesulfonyl)imide), as in SIG 4, confers a noticeable increase in modulus, consistent with electrostatic interactions between RTIL and polymer network that resist deformation.[236,237]

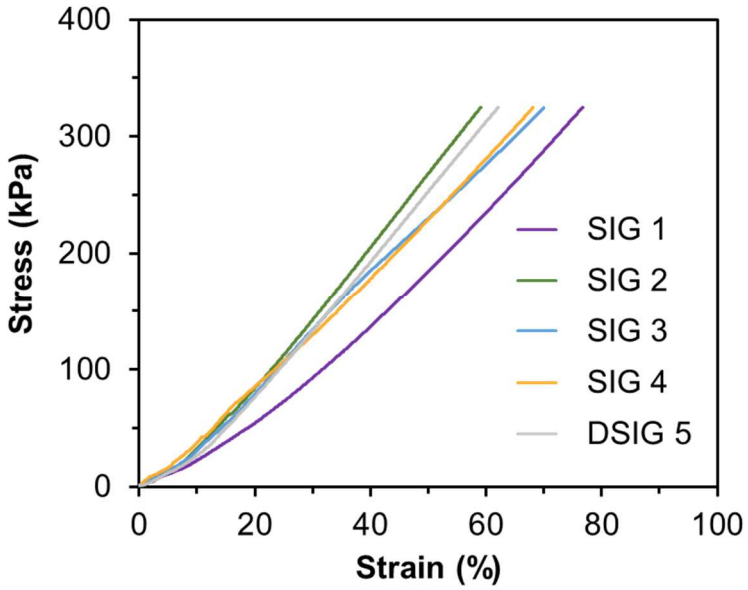

Figure 3.7. Stress-strain curves for SIGs under uniaxial compression. Curve end points correspond to the pressure limit of the experiment (325kPa), not sample failure.

Interestingly, the trend in resistance to deformation at high stress (SIG 1 < SIG 3 ~ SIG 4 < DSIG 5 ~ SIG 2) – inferred by the strain evolved at maximum pressure – is very different than the trend in resistance to deformation at low stress *i.e.* elastic modulus (DSIG 5 ~ SIG 2 ~ SIG 3 < SIG 1 < SIG 4) (**Figure 3.7**). This is likely a product of increased chain entanglement for gels based on P_{3500} as opposed to P_{750}, the latter being below PEG's entanglement molecular weight of ~2kDa,[238] as well as decreased entanglement in samples with a lower overall number of crosslinking chains (SIGs 3 and 4).[239] In a simplified way, entanglement may be thought of as restricted chain motion caused by adjacent chains crossing one another,[240] which only occurs in sufficiently-concentrated polymer solutions above a structure-dependent molecular weight (the entanglement molecular weight M_e). I was unable to quantitatively measure toughness in these samples, as none of them failed catastrophically up to the maximum pressure achievable in the load cell (325 kPa), but the ability of SIGs to withstand this compressive stress bodes well for their applicability to pouch cells and other non-rigid battery designs.

The lithium transport properties of these SIGs exhibit more significant variation; data used to determine t_{Li+} are plotted in **Figure 3.8**. While "baseline" SIG 1 displayed a room-temperature ionic conductivity of 0.79 mS/cm – slightly higher than, but similar to, SIGs with related designs[225] – increasing PEG molecular weight from P_{750} to P_{3500} produced a nearly 50% increase in conductivity, elevating SIG 2 to near Li(G4)TFSI itself at >1 mS/cm. Critically, this occurs without any change to overall polymer volume fraction. Lithium transference number also increased between samples by 33%, from 0.21 to 0.28. Note that while these t_{Li+} values are higher than most RTIL-based materials, including Li(G4)TFSI itself (measured here as 0.13), all three electrochemically-derived values fall significantly below previous reports of t_{Li+}>0.5 for Li(G4)TFSI, a product of differing measurement technique. This highlights the importance of obtaining t_{Li+} electrochemically for SIL-based materials, as PGSE-NMR-derived self-diffusion coefficients do not reflect transport under applied electric fields for non-ideal electrolytes.[129,203,219,241] Regardless, the properties of SIG 2 are exciting but anomalous, defying the conventional wisdom that gelation of an electrolyte solution reduces its conductivity.

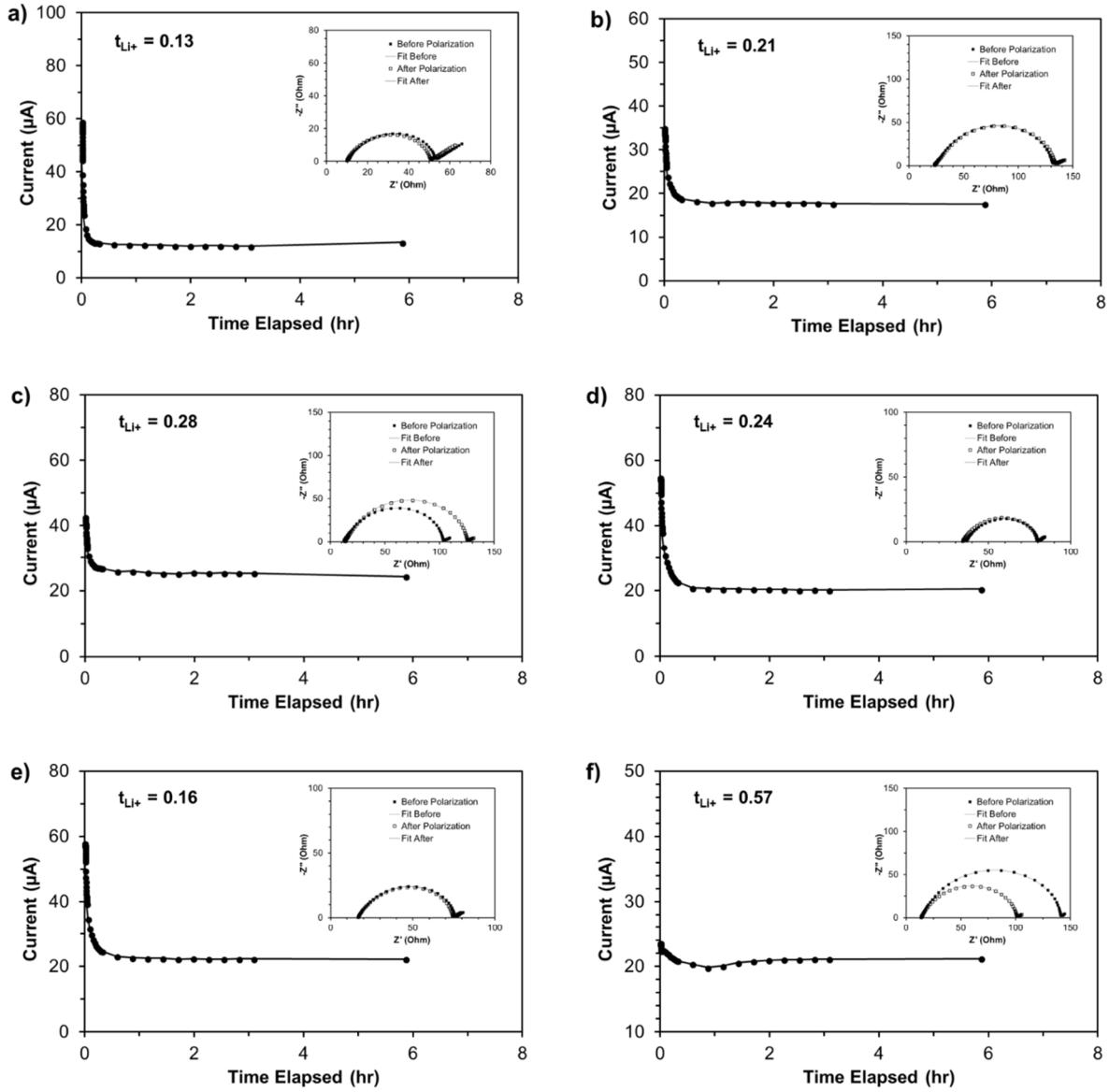

Figure 3.8. Chronoamperometry data (inset: Nyquist plots of impedance data) used to determine t_{Li+} for **a)** Li(G4)TFSI, **b)** SIG 1, **c)** SIG 2, **d)** SIG 3, **e)** SIG 4, **f)** DSIG 5.

Further variation of the SIG formula provides clues to the transport mechanism. Co-polymerization of monofunctional groups with crosslinkers has previously proven effective at manipulating gel properties,[143,237,242] and this was done here using either neutral (TEGMA) or ionic (PyrTFSIMA) groups of similar structure, while maintaining a constant total volume of polymer. In the neutral case (SIG 3), both κ (0.92 mS/cm) and t_{Li+} (0.24) were slightly worsened.

The astute reader will note that the molar volume ratio of PEG functionality to methacrylate functionality is greatly decreased in TEGMA (3 repeat units per methacrylate) as opposed to P_{3500} (~38 repeat units per methacrylate). Methacrylate functionality has been previously indicated as electrochemically inactive towards Li(G4)TFSI.[224–226] The fact that κ and t_{Li+} decrease concurrently with total volume of PEG suggests a volume-dependent effect of the polymer on ion mobility, although this effect cannot be fully decoupled from associated minor changes to the network structure. SIG 4, in contrast to its neutral counterpart, displays nearly identical conductivity to SIG 2, but significantly worsened t_{Li+}. This may be attributed to the additional, mobile anions contributed by ionic-liquid-like PyrTFSIMA, which increases the number of charge carriers but imbalances the ratio away from $[Li(G4)]^+$. This effect can be helpful for dendrite prevention,[123–125] but must be weighed against the subsequent decrease in t_{Li+} which limits current density in practical cells.

In contrast to SIGs 3 and 4, where polymer structure is altered, replacing a small volume of the liquid SIL with solvent diluent as in DSIG 5 more than doubled both conductivity (2.15 mS/cm) and t_{Li+} (0.57) compared to SIG 2. To my knowledge, this is the first demonstration of an electrochemically-measured $t_{Li+}>0.5$ in a SIG-based material, as well the first demonstration of solvent dilution applied to an immobilized SIL and of 1,4-dioxane as a diluent for Li(G4)TFSI in general. The beneficial effect of diluents on SIL properties are well-documented,[198,214,220] and dioxane is an ideal choice for this system: it is a low-molecular-weight solvent that is miscible with all other components, unreactive towards methacrylate radicals, and boils well above the curing temperature of the gel (101°C vs. 80°C); however, its dielectric constant and Gutmann DN are too low to interfere with $[Li(G4)]^+$ structure.[220] The "innocence" of dioxane in this system is further supported by Raman spectroscopy (**Figure 3.9**). The breathing mode peak at 869cm^{-1},

corresponding to Li^+-G4 interaction, appears to intensify upon initial dilution with dioxane. This peak intensity decreases with additional dioxane content but remains above that of the neat SIL. Such behavior contrasts with "non-innocent" diluents like water, in which a monotonic decrease of the breathing mode peak is observed with increasing dilution due to competition with G4 for coordination of Li^+.[220]

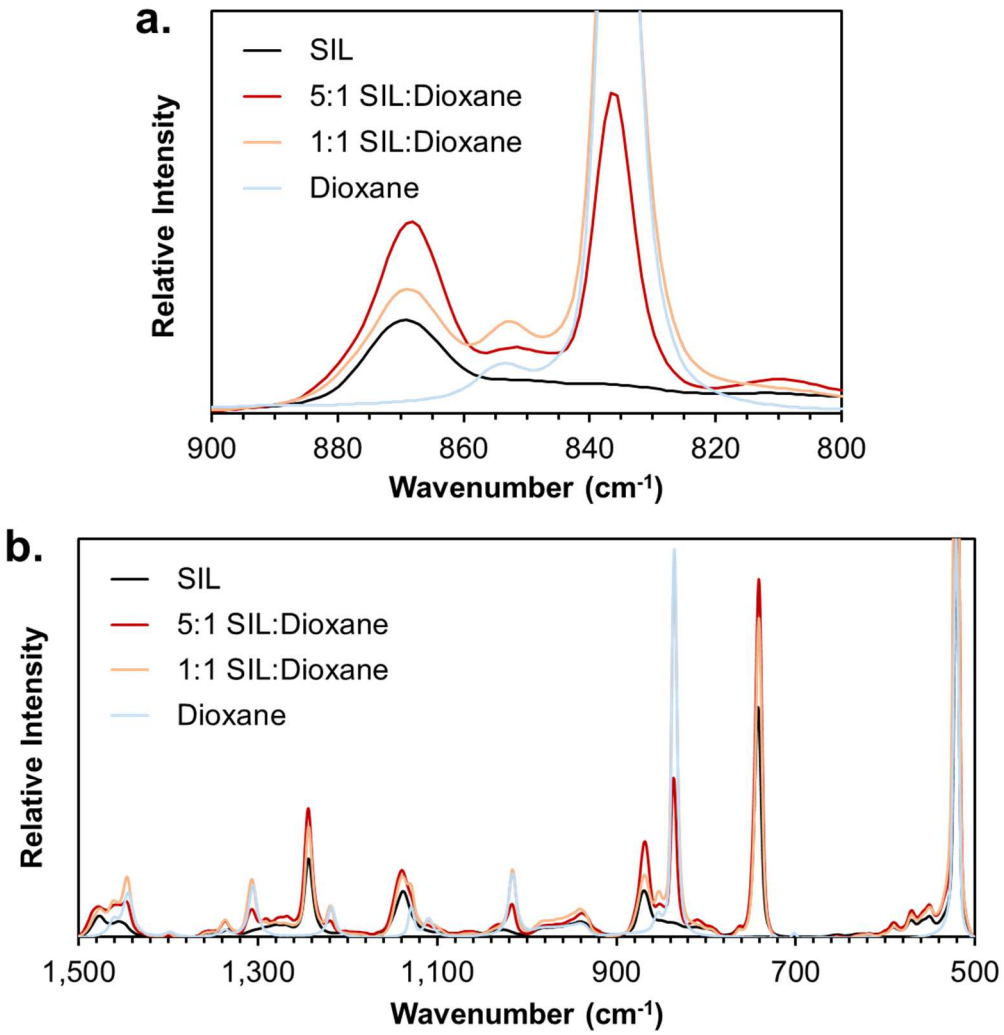

Figure 3.9. a) Raman spectra of Li(G4)TFSI ("SIL"), 1,4-dioxane, and their 5:1 + 1:1 volumetric combinations between 800-900cm^{-1}. **b)** Raman spectra for the above samples between 500-1500cm^{-1}. The intensity of the peaks at 1139cm^{-1} (deconvoluted from the nearby 1128cm^{-1} peaks) were used to normalize the data.

The exact mechanism by which solvent dilution affects electrochemical, rather than diffusion-based, t_{Li+} in SILs has yet to be clarified. This effect seems highly volume-dependent: at least one prior study has indicated a large t_{Li+} increase for a diluted SIL when solvent volume fraction becomes ~23-33% of the total,[212] similar to the combined volume of P_{3500}/dioxane in DSIG 5. Altogether, this hints at a "diluent-like" effect of PEG.

3.3.2 *PEG "Diluent-Like" Effect*

To further explore the idea of PEG-as-diluent, I prepared non-crosslinked versions of SIGs 1 and 2, referred to as LIQ 1 and LIQ 2, which differed only in absence of a crosslinking initiator. However, counterintuitively, I found that room-temperature conductivity *decreased* in the liquid state, and that the trend with molecular weight is reversed (LIQ 1: 0.72 mS/cm, LIQ 2: 0.57 mS/cm), indicating that transport in PEG/Li(G4)TFSI mixtures depends significantly on whether the polymer is crosslinked or not. Notably, PEO/LiTFSI solid electrolytes show the same trend in conductivity vs. molecular weight when M_w<4kDa *i.e.* from below to just above M_e. This has been ascribed to vanishing mobility of polymer/Li^+ complexes (as opposed to interchain Li^+ transport *via* segmental motion) above the entanglement limit.[243] In point of fact, it has been previously shown that PEG can compete with G4 for Li^+ binding in Li(G4)TFSI *i.e.* it is a "non-innocent" diluent,[224,226] which induces formation of polymer/Li^+ complexes.

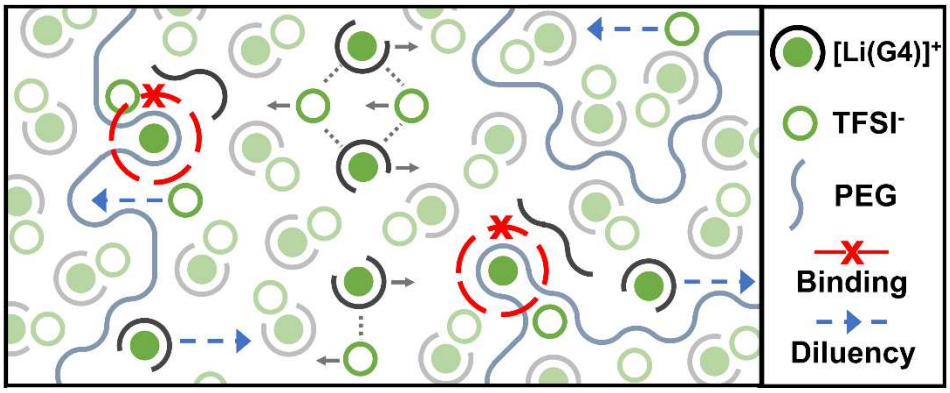

Figure 3.10. Schematic diagram of PEG/Li(G4)TFSI interactions under an applied field, conceptually depicting competitive binding of Li^+ and diluent-like mobility enhancement.

With all of the above information it is possible to rationalize the transport behavior of PEG/Li(G4)TFSI mixtures, including SIGs. I posit that competitive binding of Li^+ and "diluent-like" mobility enhancement are simultaneous-but-competing effects which depress or enhance Li^+ transport, respectively (**Figure 3.10**). Because the stability of $[Li(polyether)]^+$ complexes depends strongly on change in entropy upon binding *i.e.* the chelate effect,[199,244] the ability of PEG to effectively compete with G4 for Li^+ must be dependent on polymer conformational freedom. Chemical crosslinking results in a significant loss of freedom, especially for chain segments near the crosslinking sites,[233,245] which should therefore shift the competitive equilibrium more strongly towards G4. Competitive Li^+ binding by PEG in SILs is indirectly detectable through thermogravimetry,[224] as the liberated G4 molecules are slightly volatile at 120°C. Indeed, greater weight loss is observed at 120°C for the liquid vs. crosslinked samples (**Figure 3.11**), suggesting that the stability of the $[Li(G4)]^+$ complex is affected by PEG crosslinking status. One might expect the shorter, un-entangled P_{750} to displace G4 more readily than P_{3500} in the solution state; however, the difference in weight loss with crosslinking is actually smaller for the smaller chain, which may point towards some fundamental difference in PEG/Li(G4)TFSI interaction below the M_e. Alternately, it is possible that chain-end effects play a role.

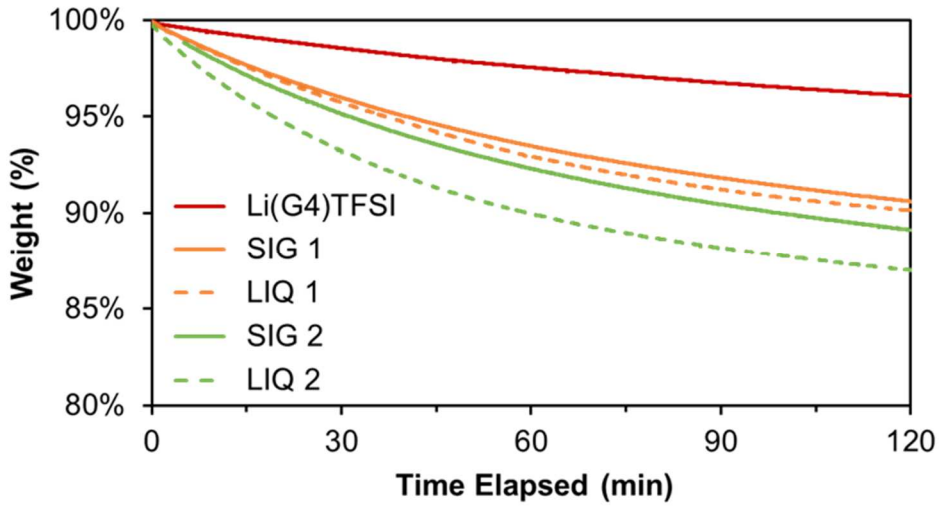

Figure 3.11. Weight loss of SIGs/LIQs 1 and 2, compared to Li(G4)TFSI, over 2 hours at 120°C.

PEG chain segments that do not compete for Li^+ may instead exert a diluent-like effect. Solvent dilution of RTILs tends to greatly reduce their viscosity and thus improve ion mobility, albeit with a concurrent, dielectric-dependent reduction of ionicity as well.[204,246,247] In lithium SILs, where cation molecular structure may also fluctuate,[201] diluents can additionally affect the structure and balance of Li^+-G4 complexes.[220] Regardless, PEG fits the criteria for an effective SIL diluent, possessing a moderate dielectric constant of ~4 and a donor number similar to glymes. In fact, studies which report lowered D_{Li+} in PEG/Li(G4)TFSI systems also report improved bulk conductivity relative to other polymer choices.[224,226] These effects could only occur simultaneously if the depressed mobility of bound Li^+ is outweighed, on average, by enhanced mobility for the remaining ions *i.e.* a diluent-like effect. Furthermore, our own results lead us to postulate that this enhancement is influenced by 1) the volume fraction of PEG relative to total SIL-swelled polymer, and, for crosslinked systems, 2) whether the molecular weight between crosslinks is above or below PEG's M_e (~2kDa).

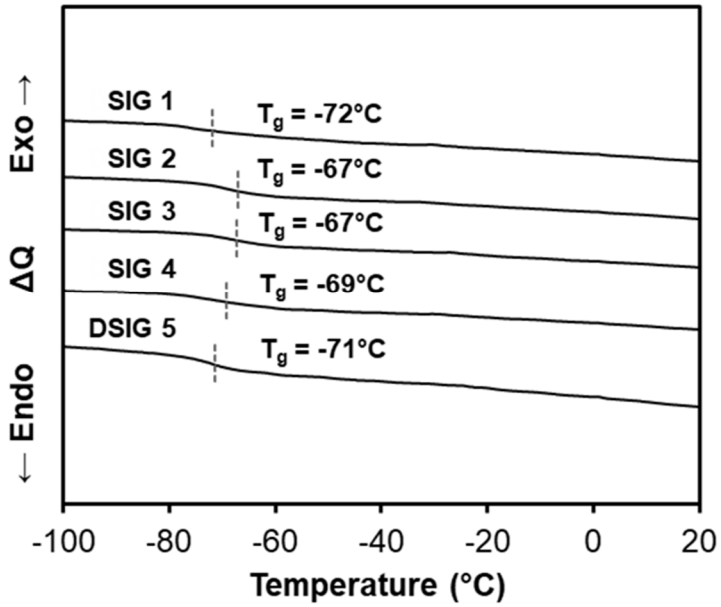

Figure 3.12. DSC thermograms and glass transition temperature (T_g) values for (D)SIGs 1-5. The dashed vertical lines are a visual aid to mark T_g.

Plasticization of the polymer network, often invoked to explain transport in solid polymer electrolytes,[248] does not seem to be a major factor, as differential scanning calorimetry data indicates a slight increase, rather than decrease, of T_g for samples with P_{3500} (**Figure 3.12**), perhaps a result of more $[Li(polyether)]^+$ complex formation. Instead, the observed dependence on polymer molecular weight is likely caused by specific chemical interactions. It is possible that, rather than being directly related to entanglement itself, enhanced mobility at higher M_w is related to the radius of gyration of the polymer in comparison to the bulky sizes of $[Li(G4)]^+$, $TFSI^-$, and their aggregates. Further study is needed to clarify the origin of this effect. Notably, no melting peak for 1,4-dioxane (lit. 11.8°C) was observed in DSIG 5, indicating strong interactions between the solvent and SIL/polymer that prevent crystallization.

The dual action of PEG (binding vs. diluency) on Li(G4)TFSI also accounts for behavior in previously-reported SIG materials. In SIG 1, as well the ionogels reported by D'Angelo *et al.*, competitive Li^+ binding by PEG is rendered unfavorable due to low molecular weight and/or

chemical crosslinking; hence, the volume-dependent diluent-like effect dominates, and both κ and t_{Li+} are observed to increase compared to similar materials lacking PEG. However, the improvement is minor, again due to low molecular weight between crosslinks. On the other hand, the PEG chain in the block copolymer reported by Kitazawa *et al.* is much longer (M_w>10kDa) and also processed at higher temperature, creating opportunities for coiled PEG segments to bind Li^+ and liberate G4. The resulting SIG displays reduced t_{Li+} compared to a methacrylate analog, although κ is still observed to increase overall due to the diluent-like effect.

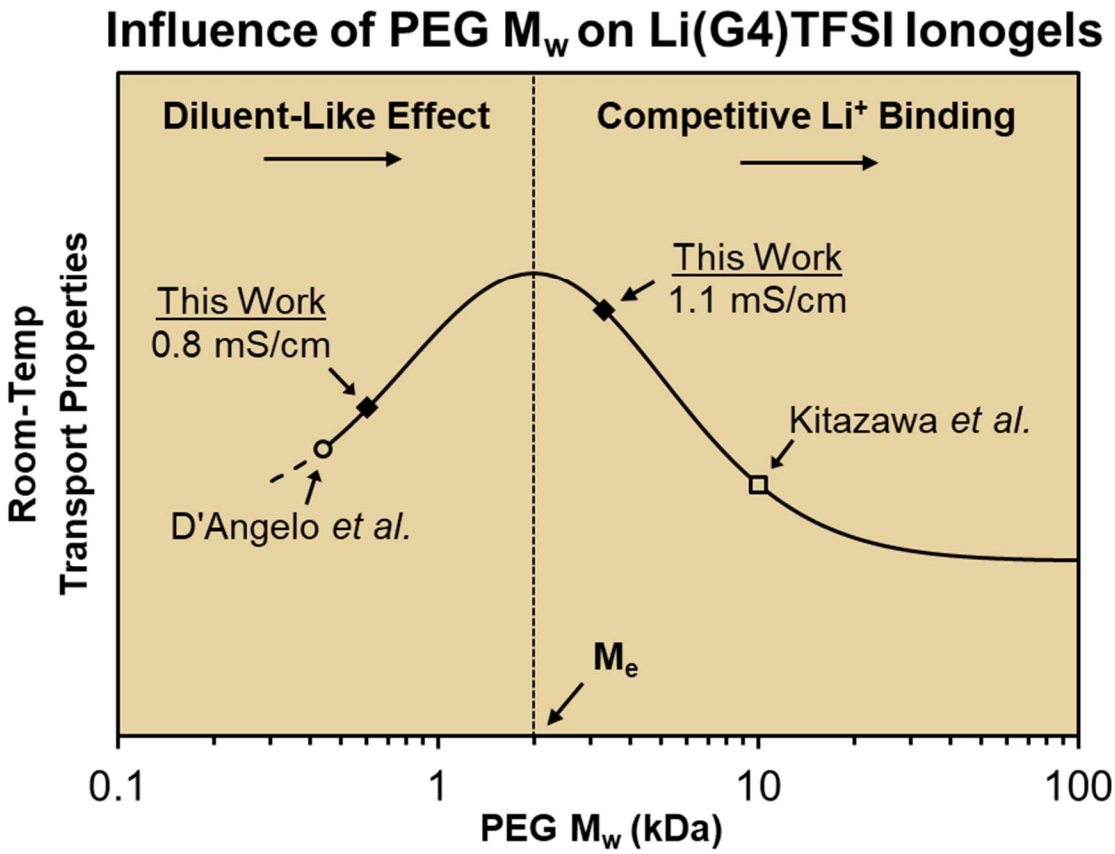

Figure 3.13. Expected dependence of Li^+ transport on PEG M_w in SIGs. The curve is a guide for the eye, demonstrating the interplay between mechanistic effects above and below M_e.

This study's P_{3500}-based SIGs apparently occupy a "sweet spot" between these cases, where molecular weight between crosslinks is large enough to maximize the diluent effect, but not so large that competitive binding of Li^+ overshadows it. This mechanistic view also suggests that

further improvement might be achieved through rational design of the polymer matrix and/or liquid composition to minimize/eliminate competitive binding while maximizing diluent-like properties. This concept will be explored further in Chapter 4.

3.3.3 *Lithium Stripping/Plating Performance*

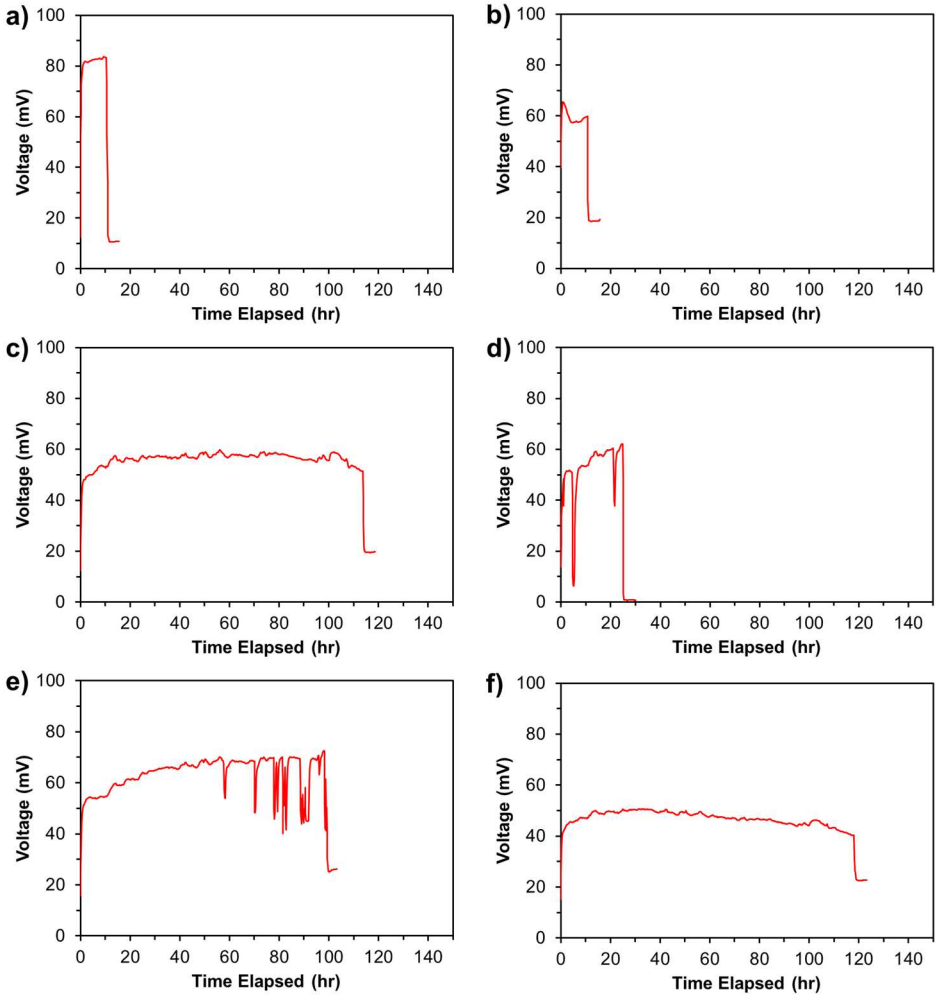

Figure 3.14. Symmetric cell voltage vs. time elapsed in time-to-short-circuit experiments at 0.1 mA/cm^2 for **a)** Li(G4)TFSI, **b)** SIG 1, **c)** SIG 2, **d)** SIG 3, **e)** SIG 4, **f)** DSIG 5.

In order to confirm that favorable SIG properties translate into good performance with lithium metal, I constructed Li|Li symmetric cells containing SIG separators and performed galvanostatic (0.1 mA/cm^2) polarization experiments at room temperature until lasting short

circuits were observed (**Figure 3.14**). Time-to-short-circuit (T_{sc}) values are summarized in comparison to neat Li(G4)TFSI contained in a large-pore glass fiber separator (**Figure 3.15**). While no major advantage over the SIL is observed for SIG 1, SIGs 2-5 show excellent dendrite resistance. Best-performers SIG 2 and DSIG 5, which have the highest concentration of P_{3500}, resisted short-circuit for longer than 100h of continuous current application – competitive with other high-performing gel electrolytes.[26] Using my newfound structural insight to analyze these results, it is clear that T_{sc} is related to chain entanglement, which should act to dissipate the force of a protruding dendrite more evenly throughout the network. Elastic modulus does not directly reflect this structural detail. High-stress behavior, however, seems to correlate better (*vide supra*), and we suggest that more future efforts be dedicated to studying and correlating non-elastic mechanical properties with dendrite resistance. We also note that SIG 4 performs much better than SIG 3 despite similar network structures, confirming that anion concentration and other chemical details also play a role.

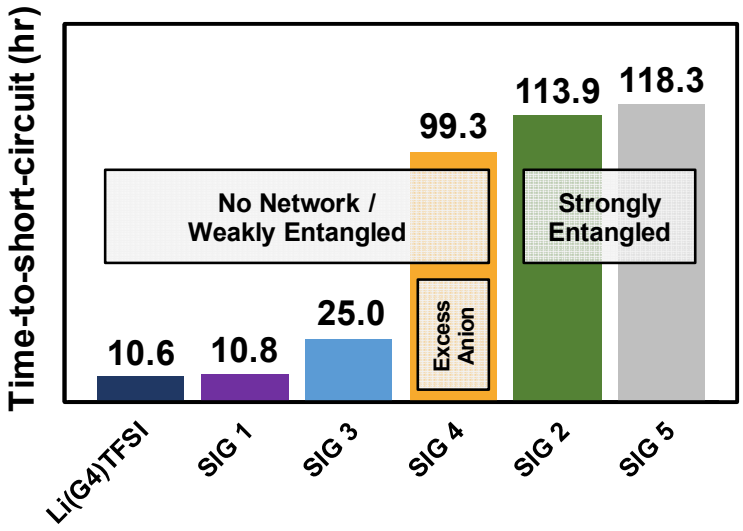

Figure 3.15. Time-to-short-circuit (0.1 mA/cm^2) for Li|Li symmetric cells with SIG separators vs. Li(G4)TFSI in glass fiber.

Cyclic stripping/plating in symmetric cells, as opposed to static polarization, more accurately mimics real device conditions. Hence the best-performing SIG 2 and DSIG 5 were compared to Li(G4)TFSI/glass fiber over 100 6h cycles at 0.1 mA/cm^2 (**Figure 3.16**). All cells exhibited an initial SEI formation period with slightly higher overpotential and irregular voltage profile shape, followed by minimum overpotential around the 50 cycle (30h) mark. Continued cycling out to 600 hours results in a very slight increase for all cells, most likely due to gradual SEI buildup, however, no signs of short-circuit were observed, and the shapes of the stabilized profiles was smooth and monotonically increasing, suggesting non-dendritic morphology.[249] Furthermore, both SIGs required significantly less overpotential for stripping/plating than neat Li(G4)TFSI, possibly due to porosity/tortuosity effects in the glass fiber separator.[250] However, comparing SIG 2 with DSIG 5, it is clear that overpotential does not correlate linearly with transport properties. Interfacial resistance likely plays a limiting role in this system, which might be selectively improved through compositional engineering.

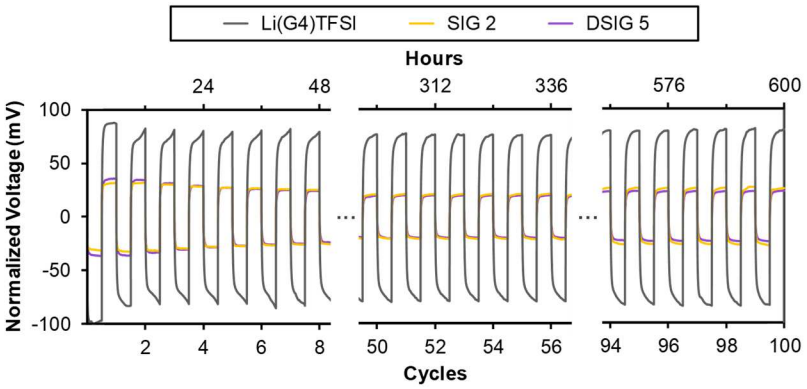

Figure 3.16. Symmetric cell cycling data for best-performing SIGs, which demonstrate consistent and lower overpotential vs. Li(G4)TFSI/glass fiber. Voltage data is normalized to Li(G4)TFSI based on sample/separator thickness to account for batch-to-batch variation and allow a head-to-head comparison.

3.4 CONCLUSION

In summary, I fabricated a series of free-standing solvate ionogel (SIGs) electrolytes based on low-cost Li(G4)TFSI immobilized in a chemically-crosslinked poly(ethylene glycol) dimethacrylate (PEGDMA) network. Through careful design of both polymer structure and liquid composition, I have demonstrated the potential to control properties such as conductivity (κ) and lithium transference number (t_{Li+}) to exceed 2×10^{-3} S/cm and 0.5, respectively. Additionally, I uncovered a significant dependence of lithium transport on PEG chain length and crosslinking status in SIGs, which may be due to an interplay between competitive Li^+ binding and "diluent-like" mobility enhancement that changes for PEG above the entanglement limit (~2kDa). These novel SIGs may be used in lithium metal batteries, with best-performing formulas able to strip/plate lithium for >600h (100 cycles) at 0.1 mA/cm^2 without short-circuiting. My results also suggest future areas for SIG optimization, such as reduction of competitive Li^+ binding, reduction of lithium interfacial resistance, and improved toughness. The combination of simple fabrication, excellent Li^+ transport, and metallic lithium compatibility makes SIGs attractive for "beyond Li-ion" battery designs, including LSBs.

Chapter 4. PROBING THE EFFECT OF POLYMER STRUCTURE AND LIQUID COMPOSITION ON SOLVATE IONOGEL ELECTROLYTES

4.1 INTRODUCTION

4.1.1 *Motivation*

During the course of my prior work on Li(G4)TFSI-based solvate ionogels (SIGs), as detailed in Chapter 3, I found an unexpected dependence of transport properties on the molecular weight M_w of poly(ethylene glycol) (PEG) between crosslinks. This led me to propose a dual effect of PEG on Li^+ transport in SIGs: competitive binding of lithium and a diluent-like enhancement of ion mobility. The former mechanism acts to reduce ionic conductivity κ and lithium transference number t_{Li+} but does not become significant until above the entanglement molecular weight M_e, which is ~2kDa in PEG.[238] The latter mechanism has the opposite effect but seems to level off above M_e. Additionally, I demonstrated the first-ever diluted solvate ionogel (DSIG) using 1,4-dioxane as a solvent diluent in a 1:5 volume ratio [dioxane:Li(G4)TFSI], and measured a quadrupling of total Li^+ conductivity in the resulting SIG as compared to an identical formula lacking dioxane.

These results caused me to wonder whether performance could be additionally improved without significantly altering the design or fabrication process. Two molecular "handles" have emerged with which to tweak SIG properties: solid polymer structure and liquid diluent composition. The polymer structure may be altered by 1. adjusting network properties such as M_w between crosslinks and density of crosslinks, 2. adding/removing molecular functionality, or 3. changing the polymer backbone structure. Since my previous work focused primarily on the first

two strategies, it seemed prudent to investigate the third, especially in regards to the question "Can competitive Li^+ binding be minimized without sacrificing the beneficial diluent effect?" Additionally, while 1,4-dioxane was selected for my initial study based on a limited survey of common solvents, it is by no means the best possible choice for DSIGs. Dioxane's low dielectric permittivity of 2.3 does not encourage efficient charge separation, and permittivity has been linked to conductivity in diluted RTILs, including Li(G4)TFSI. Dioxane also has a low-medium boiling point of 101°C, which is not ideal given that curing step of SIG fabrication involves a temperature hold at 80°C. Increasing both of these parameters should lead to a DSIG with better properties.

4.1.2 *Rationale and Overview*

In order to further explore and optimize the design of (D)SIGs, here I report the fabrication and properties of a free-standing gel electrolyte based on Li(G4)TFSI and poly(propylene glycol) dimethacrylate (PPGDMA). This polymer crosslinker shares many characteristics with PEGDMA but contains an additional methyl group in its repeat unit, which makes it considerably more hydrophobic and totally suppresses crystallization.[251] Importantly, this methyl group also introduces tacticity and raises the barrier to bond rotation,[252,253] which has significant implications for polymer interactions with $[Li(G4)]^+$. Additionally, I report a heretofore-unexplored solvent diluent for Li(G4)TFSI: methoxybenzene, or anisole. This solvent has an excellent combination of properties for use in DSIGs and is demonstrated to increase the conductivity of Li(G4)TFSI by up to seven times.

4.2 EXPERIMENTAL METHODS

4.2.1 *Materials*

Poly(ethylene glycol) dimethacrylate (P_{750}, M_n~750Da, Sigma-Aldrich), poly(ethylene glycol) (6 mmol hydroxyl end groups, M_n ~3350, Sigma-Aldrich), poly(propylene glycol) (M_n ~1000, Sigma-Aldrich), benzyol peroxide (BPO, reagent grade, ≥98%, Sigma-Aldrich), ethyl acetate (HPLC, Fisher) and dichloromethane (≥99%, Fisher) were used as-recieved. Methacryloyl chloride (97%, Sigma-Aldrich) was stored in a freezer with an airtight seal and distilled over CaH_2 under N_2 before use. Tetraethylene glycol dimethyl ether (G4, ≥99%, Aldrich), 1,4-dioxane (≥99%, Fisher), 1,1,2,2-tetrafluoroethyl-2,2,3,3-tetrafluoropropyl ether (TTFE, 98+%, Oakwood) and methoxybenzene (anhydrous, 99.7%, Sigma-Aldrich) were dried over 4Å molecular sieves and stored in an argon-atmosphere glovebox (Vacuum Technology Inc, <0.01ppm H_2O and O_2) prior to use. LiTFSI was purchased from 3M and dried at 120°C under Ar, then stored/used in an argon-atmosphere glovebox. Li(G4)TFSI and P_{3500} were prepared as detailed in Section 3.2. Diluted solvate ionic liquids (DSILs) were prepared by mixing appropriate volumes of Li(G4)TFSI and solvent in a 4mL glass vial. Lithium chips (99.9%, 15.6mm diameter, 0.45mm thickness) were purchased from MTI Corp and stored/used in an argon atmosphere glove box. CR2032 coin cell kits were purchased from Pred Materials International. PTFE unthreaded spacers (3/4“ OD, 1/4“ long) were purchased from McMaster-Carr and cleaned thoroughly prior to each use.

4.2.2 *Synthesis of PPGDMA 1150*[‡]

Poly(propylene glycol) dimethacrylate (P_{P1150}, M_n~1kDa) was synthesized by adding 2.4 ml of freshly distilled methacryloyl chloride (25 mmol) dropwise to a mixture of 10g poly

[‡] The synthesis and purification of PPGDMA 1000 was performed by Jiaxu Qin and Sei-Hum Jang.

(propylene glycol) (M_n ~1,000, 10 mmol) and 4 ml of triethylamine (30 mmol) dissolved in 120 ml of dichloromethane. The reaction mixture was stirred for 12 hours at room temperature under argon. Then, the reaction mixture was filtered to remove triethylamine hydrochloride and solvent evaporated. The crude polymer was purified by column chromatography using 50% ethyl acetate in dichloromethane as an eluent to give 4 g of product (33% yield).

4.2.3 *Gel Fabrication*

An amount of BPO powder corresponding to 2wt% of polymer was added to a glass vial and dissolved in either ~50x its weight of dichloromethane (for SIG 1, 2, and 1P) or the appropriate volume of anisole (for DSIG-C). Then the appropriate amounts of polymer (P_{P1150} for SIG 1P, P_{750} for SIG 1, 2, and DSIG-C) and Li(G4)TFSI were added and vigorously stirred; in the case of SIG 1, 2, and 1P, the resulting clear solution was then vacuum dried with stirring at room temperature for 2-3 hours, in order to fully remove dichloromethane. This precursor solution was transferred to a mold consisting of soda-lime glass plates (Colorado Concept Coatings) treated with siliconizing agent (Aquaphobe CM, Gelest) and separated by two hollow rectangular Kapton films measuring 5 mils (~128μm) each, and the mold was sealed shut using permanent magnets over both ends. Alternately, homemade conductivity cells (see below) were filled with 480μL each of solution and capped. Filled gel templates were transferred to a pre-heated glovebox antechamber 80°C for 6 hours to cure the ionogel, followed by cooling overnight. The top plates of the glass molds were then removed, and circular samples of varying diameter were cut from the gel using stainless steel hollow punches and stored in clean glass petri dishes. Gel-filled conductivity cells were stored as-is until measurement. All of the above operations were performed in an argon-atmosphere glove box. All cured SIGs were optically transparent and flexible.

4.2.4 *Conductivity Measurements*

Temperature-dependent SIG ionic conductivity was measured using homemade primary conductivity cells consisting of PTFE unthreaded spacers (3/4“ OD, 1/4“ long) with stainless steel discs as blocking electrodes. Each cell was assembled by 1. placing a large CR2032 coin cell cap flat-side-down onto a stable, level surface, 2. centering a clean stainless steel (SUS316L) spacer disc in the cap, followed by a PTFE spacer, 3. dispensing 480µL of SIG precursor resin into the PTFE spacer with a micropipette, and 4. gently placing another SUS316L spacer, centered, on top of the PTFE, followed by a flat-side-up large coin cell cap. The filled conductivity cells were then cured and stored as above. For measurement, each cell was placed in a re-sealable plastic bag with electrical leads connected *via* insulated kelvin clip (Cal Test Electronics), then removed from the glove box and placed into a convection oven (Thermo Scientific Heratherm OMH100) where it was connected *via* four-probe lead to a potentiostat (Gamry 5000E Interface). Potentiostatic electrochemical impedance spectroscopy (100mV) was performed from 100kHz-100Hz at 30-80°C. Resulting data were fitted to an appropriate equivalent circuit (**Figure 3.2**) using Gamry EChem Analyst software, and the limiting resistance at high frequency (R_{bulk}) converted to bulk ionic conductivity using the thickness (l=6.35mm) and cross-sectional area (A=9.65) of the sample (**Equation 3.2**). Two or three samples were measured simultaneously for each SIG formula, and their conductivities at each temperature averaged to obtain the reported values. Opening the cells after measurement revealed the presence of small air bubbles trapped in the gels, which were impossible to completely eliminate, despite my best efforts. This likely caused measured conductivities to systematically err towards lower conductivity than actual.

(D)SIL conductivities were measured using a low-volume liquid conductivity cell (HTCC, Bio-Logic) with non-platinized Pt electrodes, filled with 750µL of liquid electrolyte in an argon-

atmosphere glovebox. The cell was sealed, taken out, and potentiostatic electrochemical impedance spectroscopy (100mV) was performed from 100kHz-100Hz. Resulting data were fitted to an appropriate equivalent circuit (**Figure 4.1**) using Gamry EChem Analyst software, and the limiting resistance at high frequency (R_{bulk}) converted to bulk ionic conductivity using **Equation 4.4**, where K_{cell} was determined by calibrating with 0.01m KCl solution beforehand.[254] The Warburg element in the equivalent circuit accounts for surface roughness effects.[255]

$$\kappa = \frac{K_{cell}}{R_{bulk}} \tag{4.4}$$

Figure 4.1. Equivalent circuit used to fit impedance data for liquid conductivity measurements.

All temperature-dependent conductivities were fitted to a Vogel-Tammann-Fulcher (VTF) model for ionic conductivity κ (**Equation 4.5**) using Microsoft Excel's Solver tool, where R is the gas constant (8.3145 J•mol^{-1}•K^{-1}), T is temperature (K), and κ_0, $E_{a,ion}$, and T_0 are material-dependent constants.

$$\kappa = \kappa_0 \exp\left[-\frac{E_{A,ion}}{R(T - T_0)}\right] \tag{4.5}$$

4.2.5 *Lithium Symmetric Cell Measurements*

For symmetric cell fabrication, lithium chips were gently polished inside of an argon-atmosphere glovebox using 320 grit followed by 600 grit sandpaper (Norton T414 Blue-Bak) to remove excessive surface oxidation and ensure consistency between samples. The lithium chips

were then pressed onto roughened SUS316L discs. A 19mm diameter SIG separator was inserted between the chips, and the whole assembly placed into CR2032 coin cells which were sealed using an electric crimping machine (MTI Corp). Alternately, the separator consisted of a 19mm diameter Whatman GF/C separator sandwiched between two sheets of porous polypropylene (Celgard 2500), all thoroughly saturated with Li(G4)TFSI. The Celgard was used to preclude any effect of the glass fiber on lithium interfacial processes.

The lithium transference number (t_{Li+}) of SIG 1P was measured according to the procedure described in Section 3.2.5. In order to measure temperature-dependent interfacial resistance (R_{int}), symmetric cells were first pre-conditioned at 30 °C by applying 0.05 mA/cm^2 for 10h, followed by -0.05 mA/cm^2 for 10h. Cells were then placed in a convection oven and connected to a potentiostat (*vide supra*), and potentiostatic electrochemical impedance spectroscopy (10mV) was performed from 100kHz-1Hz at 30-80°C. Resulting data were fitted to an appropriate equivalent circuit (**Figure 4.2**) using Gamry EChem Analyst software. R_{SEI} and R_{ct} were summed to obtain R_{int}.

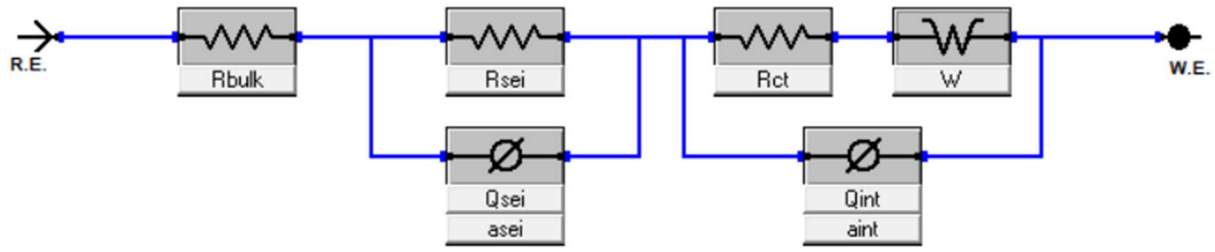

Figure 4.2. Equivalent circuit used to fit impedance data for R_{int} measurements.

4.2.6 *Thermal Measurements*

TGA was performed under flowing N_2 gas (50mL/min) using a Shimadzu TGA-50 Thermogravimetric Analyzer. A SIG 1P sample (9.02mg) was transferred into pre-weighed aluminum pans in an argon-atmosphere glove box, then weighed on a microbalance and loaded

into the instrument within ~1 minute. The sample was then heated at 10°C/min to 80°C, held for 15 minutes to drive off any superficial moisture absorbed during transfer, then heated at 10°C/min to 120°C and held for 2h while weight loss was recorded. The DSC thermogram was recorded under flowing N_2 gas (50mL/min) using a liquid-nitrogen-cooled Shimadzu DSC-60 Plus Differential Scanning Calorimeter. A SIG 1P sample (9.15mg) was transferred into an aluminum pan and covered, then cooled to below -110°C at -10°C/min. The sample was held at this temperature for 10 minutes, then warmed to 100°C at 10°C/min, resulting in the reported curve.

4.3 Results and Discussion

4.3.1 *Discussion of PPG-SIL Interaction*

While poly(ethylene oxide) *a.k.a.* poly(ethylene glycol) has been studied extensively for its ability to form solid polymer electrolytes by dissolution of alkali metal salts, poly(propylene oxide) *a.k.a.* poly(propylene glycol) (PPG) has received much less attention for this purpose. A 1999 report by Doeff and coworkers found that the ionic conductivity was lower for PPG:LiOTf solid electrolytes compared to PEG:LiOTf; additionally, microphase separation was observed, indicating comparatively poor solvation of Li^+ by PPG.[256] This characteristic, while undesirable for solid electrolytes, may actually be quite useful in SIGs, since PPG should be unable to compete effectively with G4 for solvation of Li^+.

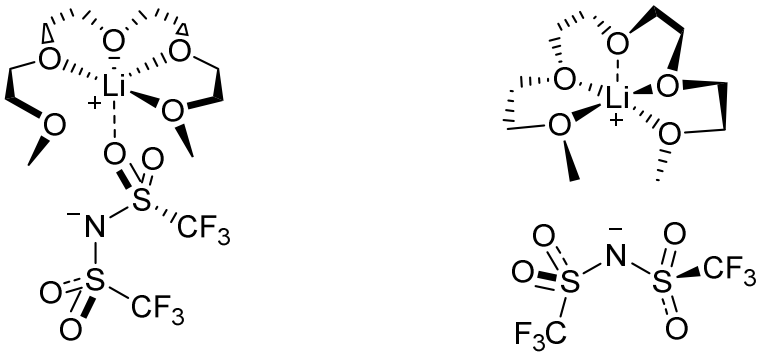

Figure 4.3. Depiction of the two predominant conformations of $[Li(G4)]^+$ in Li(G4)TFSI.

To understand why this would be the case, consider lithium solvation structure in this system (**Figure 4.3**). The predominant conformation of G4 in Li(G4)TFSI is crown-ether-like, with tetraglyme wrapping three-dimensionally around Li^+ to form an ellipsoidal-shaped $[Li(G4)]^+$ complex. On average, each cation is coordinated by 4.5 oxygen atoms from the glyme and 0.5 oxygen atoms from $TFSI^-$, as there exists both contact ion pair (CIP) and solvent-separated ion pair (SSIP) geometries with similar energy.[257] In order to fully displace a tetraglyme molecule

from the complex, a polyether would need to provide a similar number of coordination bonds (**Figure 4.4**). A single PEG chain can potentially do this, or multiple chains may participate. Regardless, since PEG and G4 share the same repeat unit, the energetics of coordination are similar. On the other hand, PPG coordination of Li^+ is more awkward: atacticity of the chain can result in unfavorable *gauche* interactions, and coordination by multiple polymer chains leads to steric crowding. Additionally, the higher rotational barrier in PPG means that a larger activation energy is required to maneuver chains into the required position.

Although the competitive binding effect is suppressed in PPG compared to PEG, the diluent-like effect should still be present. Reflecting their similar structure, both polymers have similar dielectric permittivity,[258,259] indicating that they should promote charge separation in SILs to a nearly equal degree. Additionally, while the origin of diluent-like t_{Li+} enhancement in PEG-based SIGs is still unknown, Chen *et al.* have proposed that PEG may interact with Li(G4)TFSI by replacing $TFSI^-$ in the solvate's CIP form,[235] which would naturally lead to better ion separation and enhanced t_{Li+}. Since this type of interaction only involves a single polymer repeat unit, PPG should be capable of it, although steric hindrance may still cause problems (**Figure 4.5**). Hence, replacing PEGDMA with PPGDMA in SIGs may reduce the undesirable competitive binding effect while retaining the desirable diluent-like effect.

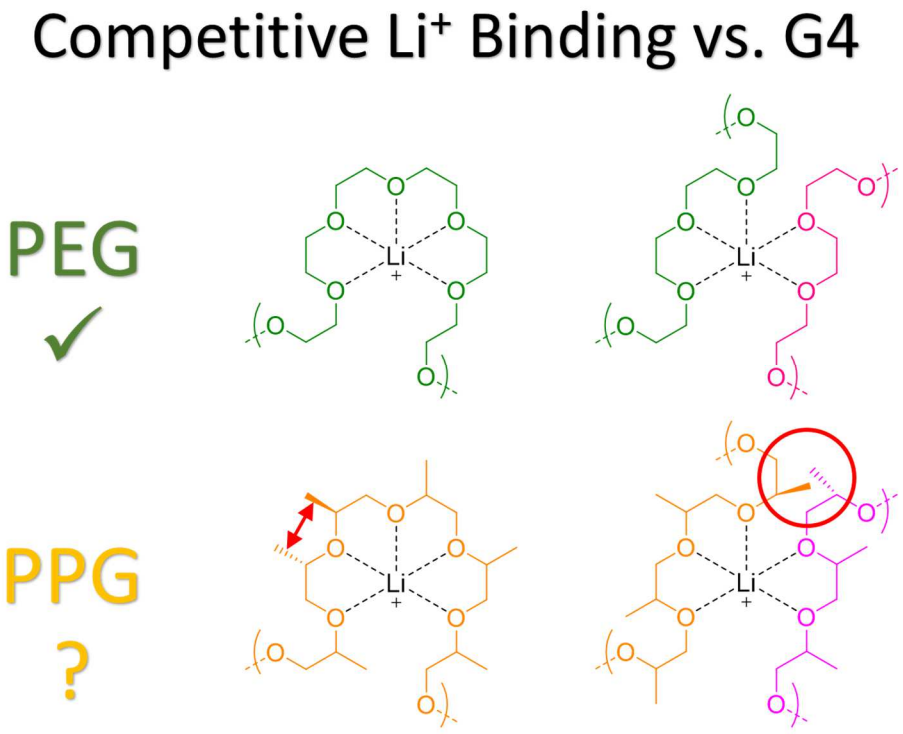

Figure 4.4. Example conformations of PEG/PPG after successfully unbinding the $[Li(G4)]^+$ complex. Atacticity and steric hindrance makes this process less favorable in PPG.

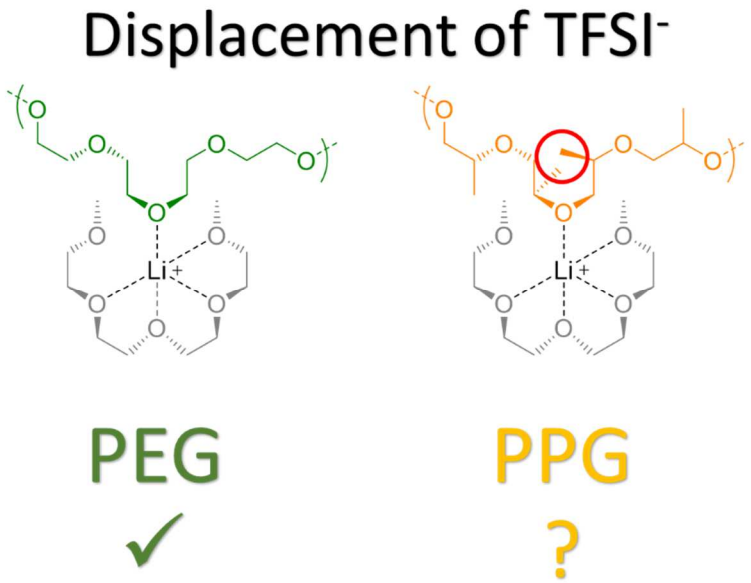

Figure 4.5. Example conformations of PEG/PPG after successfully displacing $TFSI^-$ from the $[Li(G4)]^+[TFSI]^-$ ion pair. Steric hindrance makes this process less favorable in PPG.

I tested this hypothesis by fabricating a modified version of SIG 1 from my previous study (see Chapter 3). "SIG 1P" contained 20vol% P_{P1150}, which has nearly the same degree of polymerization as P_{750}, and 80vol% Li(G4)TFSI. The only substantial difference between SIGs 1 and 1P is that the latter contains methyl groups on the polymer backbone. Competitive binding of Li^+ was probed by TGA (see Section 3.3.2) with a 2h temperature hold at 120°C, as well as by DSC. As can be seen in **Figure 4.6**, SIG 1P loses substantially less G4 to evaporation than SIG 1, and only slightly more than neat Li(G4)TFSI itself (6.8wt% vs. 3.9wt%). This is strong evidence that PPG cannot compete effectively for Li^+ solvation, leaving more $[Li(G4)]^+$ complexes intact. The T_g of SIG 1P was found to be -59°C (**Figure 4.7**), much lower than SIGs 1 or 2 and slightly higher than the literature value for Li(G4)TFSI (-54°C).[194] This is yet more evidence that PPG interacts with Li(G4)TFSI only weakly.

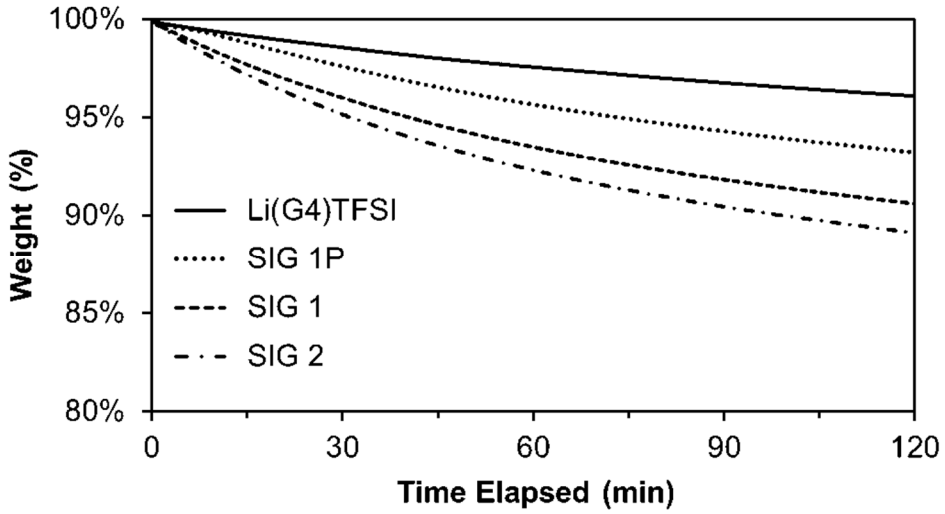

Figure 4.6. Weight loss of SIGs 1, 1P, and 2 compared to Li(G4)TFSI, over 2 hours at 120°C. Data for Li(G4)TFSI and SIGs 1 and 2 reproduced from Chapter 3 for ease of comparison to SIG 1P.

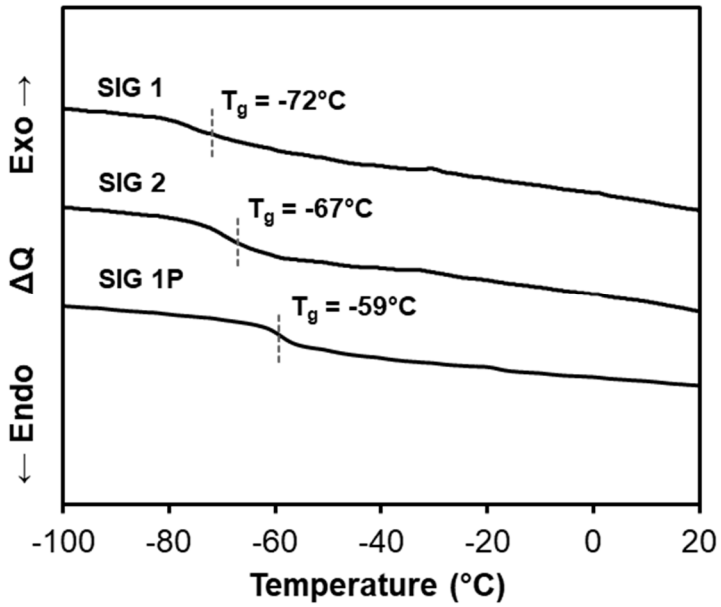

Figure 4.7. DSC thermograms and glass transition temperature (T_g) values for SIGs 1, 1P, and 2. The dashed vertical lines are a visual aid to mark T_g. Data for SIGs 1 and 2 reproduced from Chapter 3 for ease of comparison to SIG 1P.

SIG 1P's t_{Li+} was also determined using the potentiostatic polarization method; a value of 0.17 was obtained, lower than SIG 1 (t_{Li+}=0.21) and only slightly higher than Li(G4)TFSI (t_{Li+}=0.16). While disappointing from a practical point of view, this does support the conclusion that PPG interacts less-strongly with SILs than PEG does. It also lends credence to the idea that enhanced t_{Li+} in PEG/SIL electrolytes originates from non-destructive coordination of $[Li(G4)]^+$ by polymer chains, leading to separation of ion pairs. The more-sterically-hindered oxygen atoms of PPG may be unable to approach Li^+ closely enough for this process to occur efficiently.

4.3.2 *Temperature-Dependent Conductivity of SIGs*

In order to further probe the transport behavior of PEG/PPG-based SIGs, I measured temperature-dependent ionic conductivity for SIGs 1, 1P, and 2, as well as neat Li(G4)TFSI

between 30-80°C. The resulting data and VTF curve fits are plotted in **Figure 4.8**. The obtained VTF parameters, along with conductivities at 30°C, are reported in **Table 4.1**.

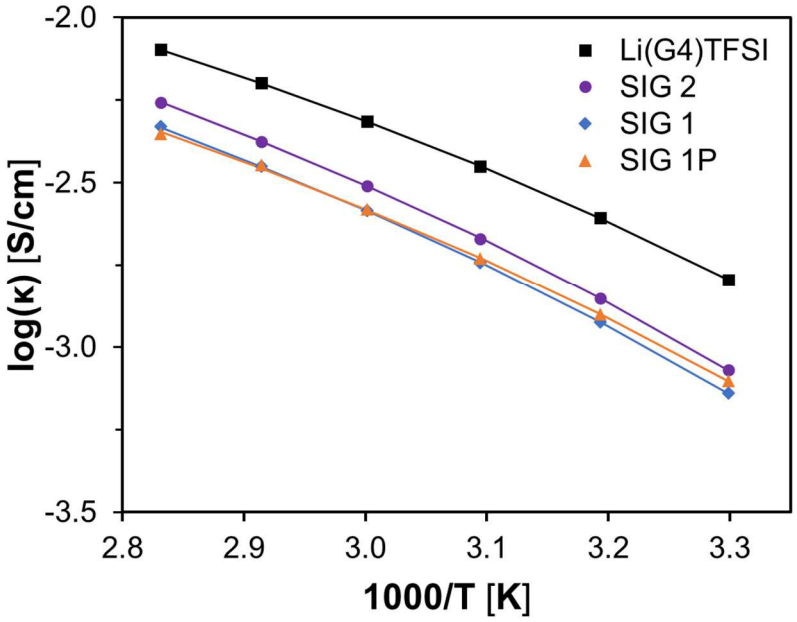

Figure 4.8. Temperature-dependent ionic conductivity (points) and VTF curve fits (lines) for Li(G4)TFSI and SIGs 1, 1P, and 2 between 30-80°C.

The VTF equation (**Equation 4.5**) is a phenomenological modification of the Arrhenius equation, modeling properties related to dielectric relaxation in glass-forming materials near their T_g. This equation has been found to accurately describe ionic conductivity in a wide range of polymer[260] and RTIL[261] electrolytes, including ionogels.[262] There are three material-dependent parameters in this equation: 1. the limiting conductivity κ_0, which is related to charge carrier concentration, 2. the activation energy of ion transport $E_{a,ion}$, and 3. the Vogel temperature T_0 at which configurational entropy disappears, which is related to T_g although the exact relationship is not perfectly clear.[263] Based on **Figure 4.8**, this model appears to fit SIG conductivity very well.

Table 4.1. Conductivity at 30°C and VTF parameters obtained for Li(G4)TFSI, SIG 1, SIG 2, and SIG 1P. Data for Li(G4)TFSI agrees well with literature.[198]

	$\kappa_{30°C}$ [S/cm]	κ_0 [S/cm]	$E_{a,ion}$ [J/mol]	T_o [K]
Li(G4)TFSI	1.60×10^{-3}	2.30×10^{-1}	4.32×10^{3}	198
SIG 1	7.24×10^{-4}	2.49×10^{-1}	5.20×10^{3}	196
SIG 2	8.50×10^{-4}	2.82×10^{-1}	5.06×10^{3}	198
SIG 1P	7.90×10^{-4}	1.93×10^{-1}	4.93×10^{3}	195

Examining **Table 4.1** reveals several interesting trends. As expected, all SIGs have a larger $E_{a,ion}$ than Li(G4)TFSI itself, since polymer chains make up a significant fraction of the overall medium and must "move out of the way" for ions to pass. Surprisingly, however, PEG-based SIGs 1 and 2 have higher κ_0 than the neat ionic liquid, despite containing a lower overall salt concentration. This strongly indicates that PEG promotes separation of $[Li(G4)]^+[TFSI]^-$ ion pairs. SIG 2 possess both higher κ_0 and lower $E_{a,ion}$ than SIG 1, demonstrating that both the diluent-like effect and polymer configurational entropy increase with increasing M_w between crosslinks, as I have proposed (see Section 3.3.2).[218] The trend in overall room-temperature conductivity with M_w is similar to my previously report, although individual values are slightly lower, likely due to the differing measurement technique. No clear trend is present for T_0, although these values are uniformly lower and less-variable than the corresponding T_g values.

Notably, substituting P_{P1150} for P_{750} causes a decrease to κ_0 but an increase to $E_{a,ion}$. This correlates well with the trends observed for thermal properties and t_{Li+}: PPG does not separate ion pairs as efficiently as PEG, nor does it slow down Li^+ transport *via* competitive binding. The practical outcome is apparent in **Figure 4.8**: substituting P_{P1150} for P_{750} causes an increase to low-

temperature conductivity, which is almost 10% higher for SIG 1P than SIG 1 at 30°C. However, this advantage gradually disappears with increasing temperature until SIG 1 overtakes SIG 1P at 80°C. In other words, this is the point at which the negative relative influence of PEG on ion mobility is outweighed by its positive relative influence on charge carrier concentration.

Solid/gel polymer electrolytes often exhibit a "compensation effect," causing $E_{a,ion}$ and $\ln \kappa_0$ to be directly related. This results from coupling between ion transport and segmental motion: stronger Li^+-polymer coordination results in better charge separation, increasing κ_0, but also stiffens the chain, increasing $E_{a,ion}$.[263] In order to optimize the ionic conductivity of freestanding electrolytes, these processes must be decoupled. In contrast to the trend for polymer electrolytes correlated by Diederichsen *et al.* in the above reference, $E_{a,ion}$ and $\ln \kappa_0$ are virtually unrelated amongst the SIGs reported here (**Figure 4.9**). Additionally, the $E_{a,ion}$ range is remarkably low compared to other electrolytes of similar κ_0; in other words, transport is "liquid-like."

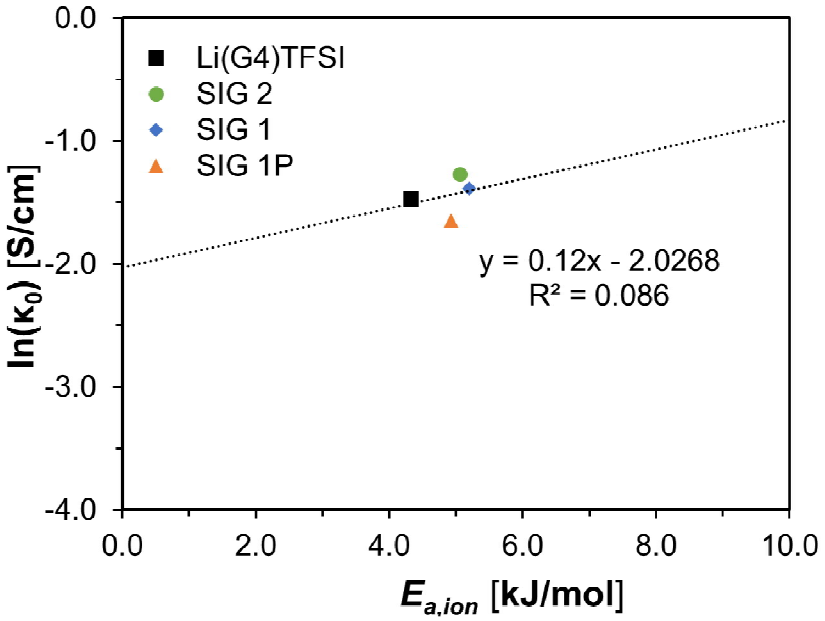

Figure 4.9. Activation energy of ion transport *vs.* limiting conductivity for Li(G4)TFSI and SIG electrolytes.

4.3.3 *Charge Transfer at the SIG-Li Interface*

While the effect of PPG/PEG on bulk ion transport in SIGs has been clarified, it is unknown how this translates to cell performance, since both transport and charge transfer kinetics may contribute to overpotential. Heterogeneous charge transfer at the lithium metal/electrolyte interface depends on many factors, including the solvation structure of Li^+ in both the electrolyte and SEI. Due to the stability of the $[Li(G4)]^+$ complex, the activation energy of charge transfer is slightly larger for SILs than many other liquid electrolytes: Yoshida and coworkers reported a value of 67 kJ/mol for Li(G4)TFSI.[198] In my previous report, I noted that lithium stripping/plating overpotential was lower in SIGs than in Li(G4)TFSI itself, and postulated that this may be due to the influence of PEG (see Section 3.3.3). In order to better clarify the effect of polyethers on processes at the Li metal interface, impedance spectroscopy was performed on Li|SIG/SIL|Li symmetric cells to measure the values of R_{int} over the temperature range 30-80°C. From this data, the activation energy of charge transfer $E_{a,ct}$ and the exchange current density i_o were extracted.

To derive the relationship between these parameters, we start with the Butler-Volmer equation and assume that 1. the symmetry factor of charge transfer is equal to 0.5, 2. all overpotential is related to charge transfer *i.e.* activation overpotential, and 3. activation overpotential is small enough to justify linearization.[264] The second assumption is justified by the fact that we will ultimately separate R_{int} from other resistances using impedance spectroscopy. This produces **Equation 4.6** below, where i is the current density (mA/cm^2), i_o is the exchange current density (mA/cm^2), n is the number of electrons transferred during reaction, F is the Faraday constant (96,485 C/mol), R is the gas constant (8.3145 $J \cdot mol^{-1} \cdot K^{-1}$), T is temperature in K, and η is the overpotential (mV).

$$i = i_o \eta \frac{\mathrm{nF}}{\mathrm{RT}} \tag{4.6}$$

The number of electrons transferred is one ($Li^+ + e^- \rightarrow Li^0$), and in a symmetric cell, the open-circuit voltage is zero; therefore, measured voltage is equal to overpotential. Rearranging and using Ohm's Law yields **Equation 4.7**, where R_{int} is the interfacial resistance (Ω) and A is electrode area.

$$\frac{1}{R_{\mathrm{int}}} = i_o \frac{\mathrm{AF}}{\mathrm{RT}} \tag{4.7}$$

Exchange current density i_o can be expressed in terms of the reaction rate constant k_o (s^{-1}), the activity coefficient of Li^+ at the interface γ_{Li^+}, the (dimensionless) concentration of Li^+ at the interface c_{Li^+}, the activity of Li^0 at the interface (equal to unity), and the Faraday constant F (**Equation 4.8**):[264]

$$i_o = \mathrm{F} k_o (\gamma_{Li^+} c_{Li^+})^{0.5} \tag{4.8}$$

If we assume that the charge-transfer reaction follows Arrhenius kinetics, then the equation above may be rewritten as **Equation 4.9**, where A_f is the frequency factor (s^{-1}) and $E_{a,ct}$ is the activation energy of charge transfer (J/mol):

$$i_o = \mathrm{F} A_f (\gamma_{Li^+} c_{Li^+})^{0.5} \exp\left[-\frac{E_{a,ct}}{\mathrm{RT}}\right] \tag{4.9}$$

Plugging this result into Equation 4.7 and taking the natural logarithm yields **Equations 4.10** and **4.11**:

$$\ln\left[\frac{1}{R_{\mathrm{int}}}\right] = \ln[\zeta] - \frac{E_{a,ct}}{\mathrm{RT}} \tag{4.10}$$

$$\zeta = \frac{\mathrm{F}^2 A_f (\gamma_{Li^+} c_{Li^+})^{0.5} \mathrm{A}}{\mathrm{RT}} \tag{4.11}$$

With the above relationship between R_{int} and $E_{a,ct}$ established, we may plot $\ln(R_{\text{int}}^{-1})$ *vs.* T^{-1} (**Figure 4.10**) and perform linear regression, extracting $E_{a,ct}$ from the slope of the line and i_o from its intercept as per **Equation 4.12** below.

$$i_o = \frac{\zeta \mathrm{RT}}{\mathrm{AF}} \exp\left[-\frac{E_{a,ct}}{\mathrm{RT}}\right] \tag{4.12}$$

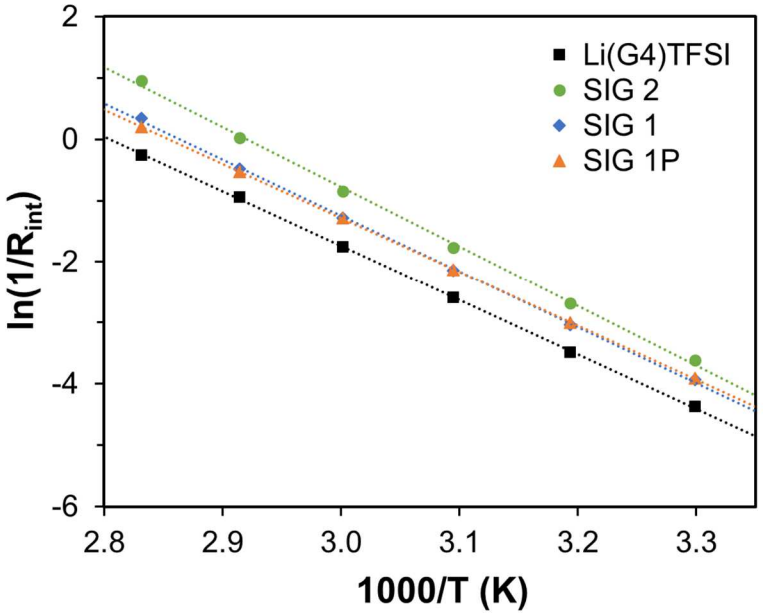

Figure 4.10. Plot of $\ln(R_{\text{int}}^{-1})$ *vs.* 1000/T for Li(G4)TFSI and SIG electrolytes.

All electrolytes showed good agreement with this model for interfacial resistance, as evidenced by the linearity of the above plot. At 30°C, SIG 2 had the lowest interfacial resistance of 37 Ω, followed by the similar values for SIG 1P (50 Ω) and SIG 1 (51 Ω). Li(G4)TFSI had the largest interfacial resistance of 79 Ω. These trends agree well with my previous report on stripping/plating overpotential (see Section 3.3.3). Calculated values for $E_{a,ct}$ and temperature-dependent i_o are plotted in **Figure 4.11**; a value of 74 kJ/mol was obtained for Li(G4)TFSI, slightly larger than the literature value.

Surprisingly, activation energy of charge transfer doesn't correlate with interfacial resistance, as SIG 2 possesses the largest $E_{a,ct}$ (81 kJ/mol), followed by SIG 1 (76 kJ/mol), Li(G4)TFSI, and SIG 1P (73 kJ/mol). In fact, it would appear that PEG increases $E_{a,ct}$, which ought to produce larger resistance. PPG has comparatively little effect on $E_{a,ct}$ however, lowering it slightly comparing to the neat SIL. On the other hand, exchange current density correlates quite well with interfacial resistance, showing the same trends with material and temperature (at 30°C, SIG 2: 0.34 mA/cm^2, SIG 1P: 0.27 mA/cm^2, SIG 1: 0.26 mA/cm^2, Li(G4)TFSI: 0.17 mA/cm^2). Apparently, the improved Li stripping/plating performance of SIGs relative to Li(G4)TFSI originates from exchange current density, rather than activation energy.

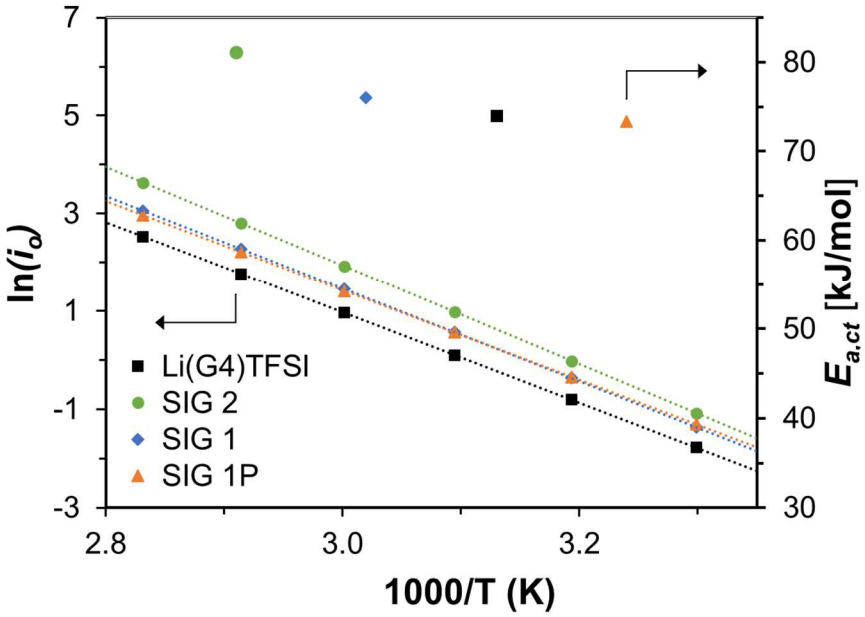

Figure 4.11. Calculated values of i_o (mA/cm^2) and $E_{a,ct}$ for all electrolytes. Exchange current density is plotted on a log scale to better demonstrate the trend among materials.

Notably, the data for SIGs 1 and 1P cross each other in Figures Figure **4.10** and Figure **4.11**, exactly the same as in Figure 4.8. This suggests that the mechanistic underpinnings for the all of these trends are similar. Examining Equation 4.9, it is clear that polymer-ion interactions

might potentially influence i_o through four variables: γ_{Li^+}, c_{Li^+}, A_f, and $E_{a,ct}$. While activation energy could possibly explain the minor differences between SIG 1 and 1P, it certainly cannot explain the performance of SIG 2. Similarly, c_{Li^+} is identical for each SIG as they all contain 80vol% Li(G4)TFSI. This leaves γ_{Li^+} and A_f as the only possible culprits. While a detailed study of either parameter falls outside the scope of this work, it should be noted that frequency factor is commonly interpreted in terms of the probability that colliding reactants (in this case, Li^+ and the charged lithium surface) occupy the correct orientation to proceed. In light of the relative abilities of PEG/PPG to participate in either competitive binding of Li^+ or diluent-like charge separation, both of which involve changes to Li^+ coordination environment, it seems likely that polyethers play a role in solvating Li^+ at the electrode surface. Further study on this topic is required.

One final note concerns the validity of the model used to derive $E_{a,ct}$ and i_o, and the discrepancy in activation energies obtained for Li(G4)TFSI. While I assume here that R_{int} can be entirely attributed to charge transfer, this may not necessarily be the case. Example Nyquist plots of SIG 1 impedance data are shown in **Figure 4.12**, along with their equivalent circuit fits. At 30°C, the data appear to consist of two overlapping semicircles: one at high frequency with a small real component, and one at lower frequency with a large real component. This necessitated a more-complex equivalent circuit to obtain an accurate value for R_{int} (Figure 4.2). One of these features may be representative of ion transport through the SEI, and it should be possible to separate charge-transfer resistance R_{ct} from SEI resistance R_{SEI}, which ought to be excluded from further calculations. However, the time constants of these processes become increasingly similar at higher temperatures and the semicircles become impossible to distinguish. Therefore, the total $R_{\text{int}} = R_{ct} + R_{SEI}$ was used instead. Since my symmetric cells were preconditioned before testing,

while Yoshida *et al.*'s were not, this may explain the slightly larger $E_{a,ct}$ value reported here for Li(G4)TFSI. However, the discrepancy (5 kJ/mol) is very small, and any error related to this effect is unlikely to have affected the overall conclusions.

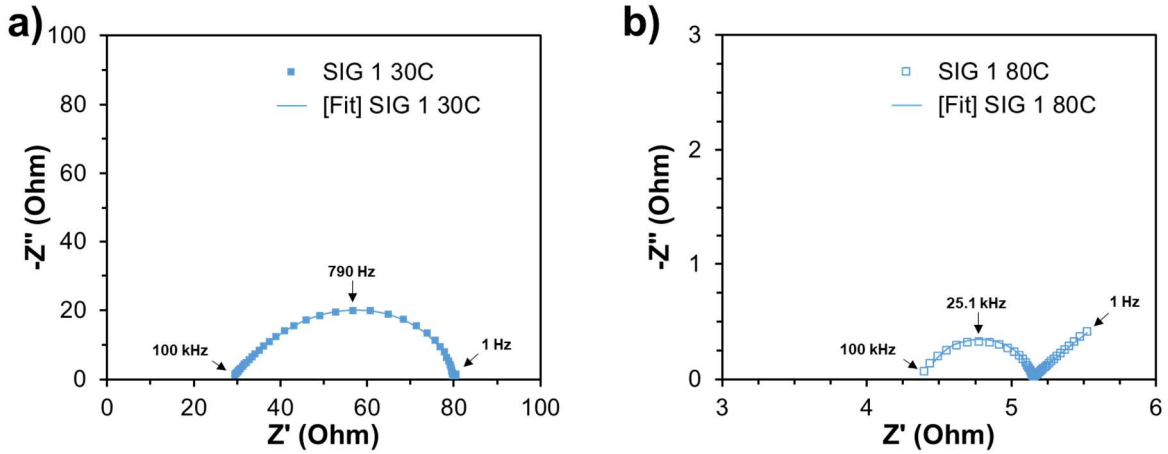

Figure 4.12. Nyquist plots of Li|SIG 1|Li impedance data and their equivalent circuit fits at **a)** 30°C and **b)** 80°C.

4.3.4 *Diluent Effects on Li(G4)TFSI and SIGs*

While polymer network structure clearly has a strong effect on transport and charge transfer in SIGs, liquid composition may also be used to tailor properties. Previously, I reported the use of 1,4-dioxane as a solvent diluent (13.3vol%), which dramatically improved κ and t_{Li+} of SIGs; however, dioxane's low boiling point (101°C) and dielectric permittivity (2.3) make it less-than-ideal. A better diluent ought to further improve SIG transport properties.

Very few solvent classes are appropriate for LSBs, considering their stability constraints (see Sections 1.3.2 and 1.3.7). Ketones, esters, sulfones, nitriles, alcohols, and halogenated solvents are ruled out due to their reactivity with lithium metal; amides, sulfones, and phosphates are questionable at best. Some aromatic solvents could be appropriate, but they usually have poor solubility for lithium salts. Carbonates are additionally ruled out due to their reactivity with Li_2S_x

species, leaving only ethers to be generally suitable. In fact, besides RTILs and a few isolated exceptions,[152,190,265,266] ethers make up the vast majority of reported solvents. While many ethers have better permittivity than dioxane (DOL: 7.1, DME: 7.2), their boiling points tend to be quite low (DOL: 76°C, DME: 85°C), which raises flammability concerns and leads to bubble formation/evaporation during SIG cure.

Li(G4)TFSI also introduces stability constraints of its own. Ueno and coworkers have found that molecular solvents with a permittivity and/or DN much larger than G4 (ε=7.7, DN=17) will unbind the $[Li(G4)]^+$ complex, which ruins its ionic-liquid-like properties.[220] These authors demonstrated a handful of solvents that can successfully increase κ while maintaining solvate integrity, but only two of them (toluene and 1,1,2,2-tetrafluoroethyl-2,2,3,3-tetrafluoropropyl ether, or TTFE) meet LSB stability criteria. Based on the above report, an ideal solvent diluent would possess the highest-possible ε≤40, the highest-possible DN≤17, and the lowest-possible viscosity.

After a thorough literature search, I have identified a new diluent candidate for Li(G4)TFSI which satisfies all constraints: anisole *a.k.a.* methoxybenzene (**Figure 4.13**). Anisole is both an ether and an aromatic solvent, possessing a higher boiling point (154°C) than most members of either class. It has been previously reported as an additive for lithium-ion batteries[267] and, due to the π-donating effect of the $-OCH_3$ substituent, it is stable to reduction by lithium metal.[268] Its permittivity (4.7)[269] and DN (9)[270] are within the acceptable range for Li(G4)TFSI, and it contains no functional groups likely to react with Li_2S_x under LSB conditions. Finally, it has extremely low viscosity (0.9cP at 30°C)[271] comparable to DOL (0.6cP at 25°C)[272] and DME (0.4cP at 20°C).[273]

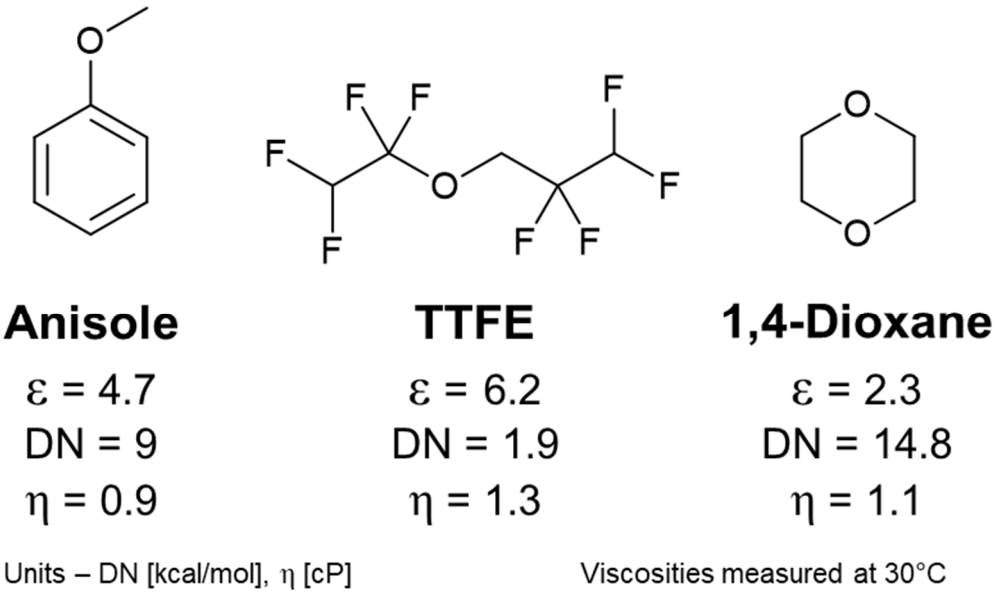

Figure 4.13. Molecular structures and relevant reported properties of three molecular solvents investigated as diluents for Li(G4)TFSI. References given in text.

To investigate the effect of anisole on Li(G4)TFSI, a series of DSILs were prepared with anisole, TTFE, and dioxane for comparison. Conductivity at lab temperature (23±1°C) was then measured for each blend as detailed in Section 4.2.4, and the results plotted in **Figure 4.14** below. The measured values of κ for Li(G4)TFSI and Li(G4)TFSI:TTFE agree with previous reports,[220] confirming the accuracy of the method. The hydrofluoroether TTFE (ε=6.2 and DN=1.9, viscosity 1.3cP at 30°C[274]) is found to moderately improve ionic conductivity, with a maximum of 5.0 mS/cm observed at 1:2 mixing ratio. At the 5:1 dilution previously used in DSIG 5, TTFE and dioxane produce identical κ values of 1.8 mS/cm; notably, this is still less than the measured conductivity of DSIG 5, suggesting an additional improvement from PEG diluent-like effect. Dioxane slightly surpasses TTFE at 1:1 mixing ratio (4.8 *vs.* 4.4 mS/cm), suggesting that its lower viscosity (1.1cP at 30°C)[275] and/or higher DN (14.8)[270] become more relevant at higher dilutions.

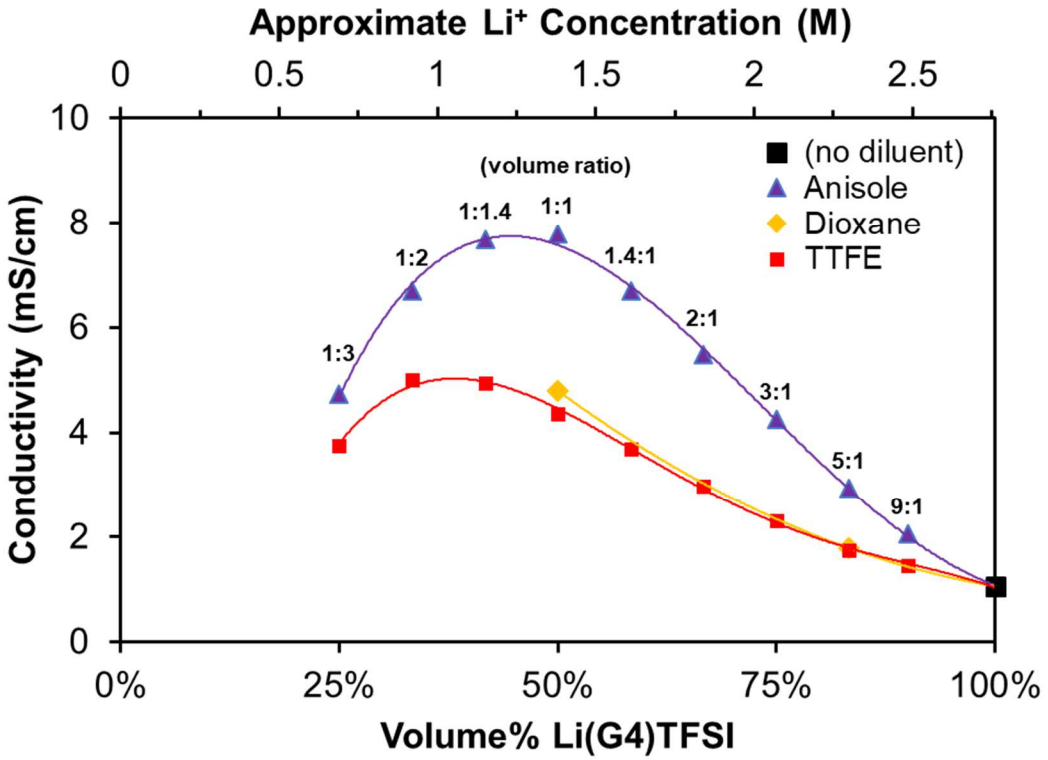

Figure 4.14. Room temperature ionic conductivity of Li(G4)TFSI diluted with anisole, 1,4-dioxane, or TTFE in varying ratios. Lines are guides for the eye. Molarity is approximate since volume change of mixing was not measured.

Anisole, on the other hand, easily surpasses both solvents, producing a conductivity of 2.9 mS/cm at 5:1 dilution and a maximum of 7.8 mS/cm at 1:1 dilution. To my knowledge, this exceeds any other reported diluent which is thermodynamically stable to the $[Li(G4)]^+$ complex and to lithium metal. The >700% conductivity boost achievable with anisole is a product of its unique combination of moderate ε and DN with low viscosity.

A new DSIG formula was developed with this diluent: 20vol% P_{750}, 66.6vol% Li(G4)TFSI, and 13.3vol% anisole. This material was termed "DSIG-C1" due to its later use in sulfur cathodes (see Chapter 5) and parent material SIG 1. Short-chain P_{750}, liquid at room temperature, was used rather than P_{3500} to simplify processing. The temperature-dependent ionic conductivity of DSIG-C was measured as described above, with resulting data plotted in **Figure 4.15**.

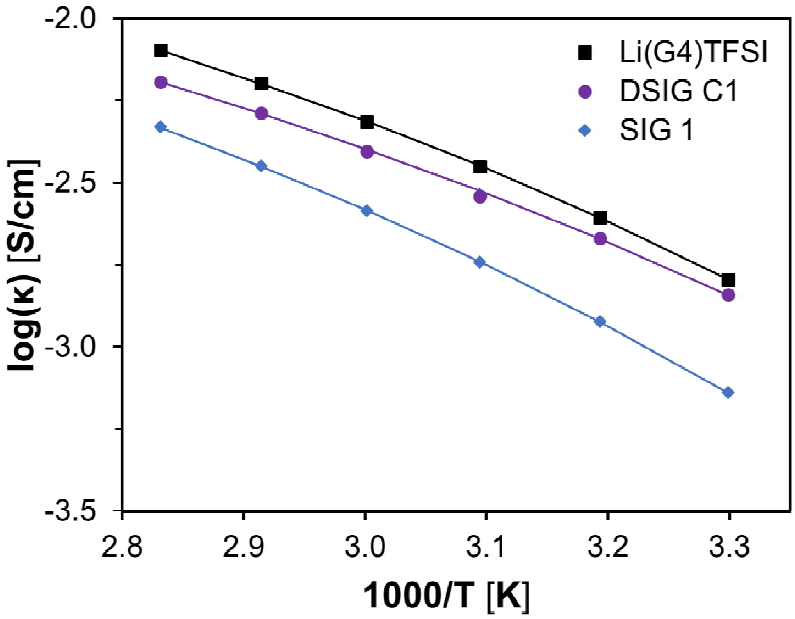

Figure 4.15. Temperature-dependent ionic conductivity (points) and VTF curve fits (lines) for DSIG C1 between 30-80°C. Data for Li(G4)TFSI and SIG 1 reproduced from Figure 4.8 for comparison.

Table 4.2. Conductivity at 30°C and VTF parameters obtained for DSIG C1. Data for Li(G4)TFSI and SIG 1 reproduced from Table 4.1 for comparison.

	$\kappa_{30°C}$ [S/cm]	κ_0 [S/cm]	$E_{a,ion}$ [J/mol]	T_0 [K]
Li(G4)TFSI	1.60×10^{-3}	2.30×10^{-1}	4.32×10^{3}	198
SIG 1	7.24×10^{-4}	2.49×10^{-1}	5.20×10^{3}	196
DSIG C1	1.44×10^{-3}	1.95×10^{-1}	4.67×10^{3}	188

As with other SIGs, DSIG C1's conductivity is modeled very well by VTF behavior; the parameters obtained from fitting are presented in **Table 4.2** above. Dilution with anisole is found to roughly double the room-temperature ionic conductivity of SIG 1, despite producing a decrease in limiting conductivity. This behavior is quite common for RTILs, as solvent dilution tends to introduce nanoinhomogeneities that reduce ionicity,[204] although PEG is an exception to this rule

for SILs. Anisole, however, does not appear to effectively displace $TFSI^-$ from the Li^+ coordination shell, likely due to its lower ε and DN compared to G4. The reduced κ_0 is more than compensated for by reduced local viscosity, measured here as reduced $E_{a,ion}$. Vogel temperature T_0 also decreases significantly, indicating an increase in conformational entropy which also improves transport.

4.4 CONCLUSION

In summary, the temperature-dependent ion transport and charge transfer properties of PEG- and PPG-based SIGs were measured in comparison to Li(G4)TFSI. Due to atacticity and/or steric hindrance, PPG was found to interact less-strongly with Li(G4)TFSI, as evidenced by lower values for κ_0, $E_{a,ion}$, and t_{Li+}, in addition to thermal measurements. Overall, slightly-improved room-temperature conductivity was observed for PPG-based SIG 1P (0.79 mS/cm) as compared to otherwise-identical, PEG-based SIG 1 (0.72 mS/cm). Additionally, measurement of temperature-dependent R_{int} in Li symmetric cells revealed that the reduced stripping/plating overpotential in SIGs compared to SILs originates from improved exchange current density i_o. However, all measured values of i_o at 30°C (0.16-0.34 mA/cm^2) were still 1-2 orders of magnitude below traditional organic electrolytes (>1 mA/cm^2).[276,277] While impedance spectroscopy has been known to underestimate i_o in some cases, the highlighting the need for additional research on the mechanism of charge transfer in SIL-based electrolytes and how the kinetics of this process may be further improved. Finally, methoxybenzene *a.k.a.* anisole was demonstrated as a superior solvent diluent for Li(G4)TFSI, enhancing room-temperature conductivity by >700% at 1:1 dilution. Anisole was incorporated into the SIG 1 formula at 13.3vol% to produce DSIG C1, and the solvent was found to significantly decrease $E_{a,ion}$ and T_0 resulting in a doubling of room-

temperature conductivity (1.44 mS/cm). DSIG C1 shows tremendous promise as an electrolyte for LSBs.

Chapter 5. QUASI-SOLID-STATE LITHIUM-SULFUR BATTERIES BASED ON SOLVATE IONOGEL ELECTROLYTES

The experiments discussed in this chapter were designed, performed, and analyzed collaboratively by myself and colleagues Yun (April) Li and Jiaxu Qin.

5.1 INTRODUCTION

5.1.1 *Motivation*

All-solid-state designs are generally desirable for lithium secondary batteries, including LSBs, since they may improve safety, simplify fabrication, and eliminate structural "dead weight."[66] Additionally, the previous chapters of this dissertation have discussed at-length the myriad specific advantages of Li(G4)TFSI-based solvate ionogels (SIGs) for LSBs, including spatial control of Li_2S_x diffusion, Li dendrite prevention, and elimination of flammable/gas-generating organic electrolytes. While SIGs have demonstrated to possess good lithium transport properties and acceptable Li stripping/plating performance, I am unaware of any existing literature on the use of SIGs in an LSB system. In fact, there have been very few reports on LSBs with ionogel electrolytes of any kind.[278,279] This may be due to the inherent challenge of cathode/separator wetting, as mentioned previously in Section 3.1.1. The difficulty of wetting nonpolar surfaces with RTILs is further compounded by the introduction of a solid matrix or its precursors, which may further inhibit electrolyte penetration into highly-porous carbon composites. Baloch and coworkers directly acknowledged this challenge in their report on gel polymer electrolytes based on polymeric ionic liquids (GPE-PIL); ultimately, they were forced to include an organic electrolyte to achieve reasonable LSB performance, with GPE-PIL relegated to

a cathode binder role. Ogawa and coworkers took a different approach, blending their RTIL/fumed silica ionogel directly with a C/S composite during cathode fabrication. This allowed their LSB to achieve >1300 mAh/g_S initial capacity without requiring organic electrolyte. However, these cells exhibited rapid capacity fading (<800 mAh/g_S after 10 cycles), even at a low rate of C/20. They attributed this to rapid passivation of cathode surfaces by Li_2S, which may be due to the near-total immobility of sulfur species in their design.

On the other hand, the SIG design strategy demonstrated in Chapters 3 and 4 may provide a route around these problems. PEGDMA-based SIGs are not fabricated as gels, but rather as crosslinkable liquid resins which gelate upon radical initiation. Furthermore, unlike the SIGs reported by D'Angelo and coworkers,[225] initiation is triggered by heat rather than UV light, which allows for opaque substrates *i.e.* carbon to be integrated into SIGs without compromising curing efficiency. An 80°C heating step is already included in most LIB/LSB electrode fabrication processes, which start from a viscous slurry of active material, additives, and binders in low-volatility solvent (NMP). This suggests that SIG precursors might be added directly to a cathode slurry, coated onto a substrate, then cured, forming an *in-situ* crosslinked composite with S/C particles evenly distributed and wetted with electrolyte. Such a process would simultaneously bypass most of practical challenges associated with ionogels in LSBs, allowing better long-term evaluation of the electrochemistry in such a device.

5.1.2 *Rationale and Overview*

Herein I report the fabrication of separator and S/C cathode composites containing solvate ionogels, both of which demonstrate excellent bulk conductivity due to intimate contact between components. These composites are combined with a Li metal anode to produce, for the first time, a quasi-solid-state (QSS) LSB based on SIG electrolyte. The electrochemical performance of this

design is explored in detail, including its galvanostatic cycling performance and the origin of various overpotentials. A QSS design is found to outperform traditionally-constructed LSBs with both organic and SIL-based electrolytes, retaining 774 mAh/g_S (66% of initial capacity) after 100 cycles at C/10 and maintaining an average coulombic efficiency of 96.5% without any passivating additives. These results demonstrate the viability of ionogel-based LSBs and suggest a path to high-performance using integrated molecular design.

5.2 EXPERIMENTAL METHODS

5.2.1 *Materials*

Poly(ethylene glycol) dimethacrylate (P_{750}, M_n~750Da, Sigma-Aldrich), poly(ethylene glycol) (6 mmol hydroxyl end groups, M_n ~3350, Sigma-Aldrich), azobisisobutyronitrile (AIBN, 98%, Sigma-Aldrich), HCl (ACS reagent, 37%, Sigma-Aldrich) ethyl acetate (HPLC, Fisher), ethanol (200 proof, Decon Labs), and dichloromethane (≥99%, Fisher) were used as-recieved. Methacryloyl chloride (97%, Sigma-Aldrich) was stored in a freezer with an airtight seal and distilled over CaH_2 under N_2 before use. Tetraethylene glycol dimethyl ether (G4, ≥99%, Aldrich), 1,4-dioxane (≥99%, Fisher), and anisole (anhydrous, 99.7%, Sigma-Aldrich) were dried over 4Å molecular sieves and stored in an argon-atmosphere glovebox (Vacuum Technology Inc, <0.01ppm H_2O and O_2) prior to use. LiTFSI was purchased from 3M and dried at 120°C under Ar, then stored/used in an argon-atmosphere glovebox. Li(G4)TFSI and P_{3500} were prepared as detailed in Section 3.2.

Sulfur (S_8, powder, 99.98% trace metals basis, Sigma-Aldrich), Li_2S (99.98% trace metals basis, Sigma-Aldrich), $LiNO_3$ (anhydrous, 99.98% metals basis, Alfa-Aesar), poly(vinylene difluoride) (PVDF, 600kDa, MTI Corp), 1-methyl-2-pyrrolidinone (NMP, 99%, Sigma-Aldrich), 1,3-dioxolane (DOL, anhydrous, contains ~75 ppm BHT as inhibitor, 99.8%, Sigma-Aldrich), and 1,2-dimethoxyethane (DME, anhydrous, 99.5%, inhibitor-free, Sigma-Aldrich) were stored/used as-received in an argon-atmosphere glovebox (Vacuum Technology Inc, <0.01ppm H_2O and O_2). Carbon black (C-NERGY™ Super C65, Imerys) and multi-wall carbon nanotubes (MWCNT, <5nm diam, SES Research) were stored in a 70°C drying oven and removed only when needed. MJ430 (Porous Carbon CNovel™, Toyo Tanso USA) was purified by acid wash with 2 M HCl in ethanol, then rinsed thoroughly with ethanol, vacuum dried, and stored in a sealed glass vial prior

to use. Lithium chips (99.9%, 15.6mm diameter, 0.45mm thickness) were purchased from MTI Corp and stored/used in an argon atmosphere glove box. CR2032 coin cell kits were purchased from Pred Materials International. Celgard 2500 (85mm x 60m roll) was purchased from AME Energy Co., Ltd and used as-received. Aluminum foil (280mm x 350m x 15 μm roll) and carbon-coated aluminum foil (260mm x 80m x 18μm roll) were purchased from MTI Corp.

5.2.2 *Synthesis of S/C Composites*[§]

Solid S_8 and purified MJ430 were added in the desired weight ratio to an agate mortar/pestle and ground together until visually homogeneous, then added to a quartz vacuum tube. The tube was evacuated and refilled with argon (UHP, 99.999%) three times, then sealed under vacuum with an oxy-acetylene torch and heated at 155°C for 24 h to produce melt-diffused S/C composites.

5.2.3 *Fabrication of SIG/Celgard Composite Separators*

Inside of an argon-atmosphere glovebox, AIBN powder corresponding to 2wt% of polymer was added to a glass vial and dissolved in ~50x its weight of dry dichloromethane. Then, appropriate amounts of P_{750} and Li(G4)TFSI were added and magnetically stirred for 10 minutes to produce a clear, transparent solvate ionogel (SIG) precursor resin. 200μL precursor was slowly micropipetted onto the center of a porous polypropylene (Celgard 2500, or simply "Celgard") sheet, which was wrapped tightly around and taped to the underside of a soda-lime glass plate (Colorado Concept Coatings) treated with siliconizing agent (Aquaphobe CM, Gelest). After allowing a few minutes for the resin to thoroughly soak the separator, another siliconized plate was gradually placed on top of the assembly to evenly distribute resin across/through the sheet.

[§] This procedure was performed by Yun Li and Jiaxu Qin.

Rare-earth magnets were then affixed to top and bottom of the plates to secure the assembly together; the Celgard functioned as its own spacer in this gel mold, limiting the height of the total composite. Finally, the mold was transferred into a preheated antechamber at 80°C for 3 h, followed by a 24 h rest to ensure full cure. After this, the SIG 1/Celgard composite film was gently removed from the mold and cut into 19mm diameter separators using a compact disc cutter (MSK-T-07, MTI Corp). The separators were stored in a glass jar inside the glovebox. Thickness was measured with a micrometer and found to be 40μm on average.

5.2.4 *Fabrication of S/C/SIG Composite Cathodes*

Exact weights of S/C composite and Super C65 carbon black (typically a 265:35 ratio) were added to an agate mortar/pestle and ground together until mixed thoroughly. The mixture of solids was then added to a clean glass vial and transferred into an argon-atmosphere glovebox. Meanwhile, in the glovebox, appropriate amounts of P_{750}, AIBN (2%wt of polymer), Li(G4)TFSI, and anisole (+10% additional anisole to account for evaporation) were added to a glass vial and magnetically stirred for 10 minutes to produce a clear, transparent solvate ionogel (SIG) precursor resin. Then, the solids mixture and resin mixture (typically 1:9 weight ratio) were sequentially added to a 12mL polypropylene ointment container (Umano UG), along with three zirconia grinding balls (2mm). The container was closed and sealed with Parafilm M™, then allowed to rest for 3 h to ensure full wetting of the resin into the solid powder. The container was then removed the glovebox and mixed three times for 5 min at 2000rpm in a Thinky SR-500 planetary centrifugal mixer to create an S/C/SIG cathode slurry. Finally, the container was transferred back into the glovebox.

Meanwhile, a conductive substrate was prepared by tightly wrapping a smooth sheet of battery-grade aluminum foil around a soda-lime glass plate (9 x 15 cm), then affixing it to the

underside with tape. This was transferred into the glovebox along with a 9 x 15 cm piece of EPDM rubber (1/16" thick, 60A, Grainger) cut into a hollow rectangular gasket with interior 7 x 13 cm, a second glass plate, and several rare-earth magnets. The S/C/SIG slurry was manually blade-coated onto the foil using a micrometer-adjustable film applicator (150 mm width, MTI Corp), then the mold was closed/sealed using the rubber gasket and second glass plate with rare earth magnets affixed to the top and bottom. The entire assembly was transferred into a preheated antechamber at 80°C for 3 h, followed by a 24 h rest to ensure full cure. The assembly was kept sealed in the glovebox until the day of cell fabrication.

5.2.5 *Fabrication of Quasi-Solid-State Li-S Batteries*

Inside of an argon-atmosphere glovebox, S/C/SIG-coated Al foil was gently removed from its mold and cut into 15mm electrodes using a compact disc cutter (MSK-T-07, MTI Corp). These were weighed and then immediately stored inside individually-labeled 20mL glass scintillation vials. Areal loadings ranged 0.9-1.3 mg_S/cm^2. Thickness was measured with a micrometer and found to be about 150μm on average. Lithium chips were gently polished using 320 grit followed by 600 grit sandpaper (Norton T414 Blue-Bak) to remove excessive surface oxidation and ensure consistency between samples, then pressed onto roughened stainless steel (SUS316L or "SS") discs. QSS LSBs were assembled into CR2032 coin cells by sequentially placing S/C/SIG cathodes, SIG 1/Celgard separators, and Li/SS anodes on top of one another. Cells were closed with an electric coin cell crimping machine (MSK-160D, MTI Corp).

5.2.6 *Fabrication of Traditionally-Constructed Li-S Batteries*

In a typical procedure, PVDF and NMP were added to a 12mL ointment jar and mixed to form a solution, followed by addition of S/C composite and Super C65 (80:10:10 [S/C:PVDF:C65]

weight ratio) and mixing for 15 min at 2000rpm in a Thinky SR-500 planetary centrifugal mixer to produce a slurry. The slurry was coated onto smooth Al foil using an automatic film coater (MSK-AFA-II-VC-H, MTI Corp) with a micrometer-adjustable film applicator (150 mm width, MTI Corp), then superficially dried using a heated cover. The cathode-coated foil was then dried under active vacuum for 12 h at 50°C. Finally, 15mm diameter cathodes were punched using a heavy-duty disc cutter (EQ-T06-Disc, MTI Corp), then individually weighed and transferred inside an argon-atmosphere glovebox for storage. Typical areal loadings were 0.8-1.1 mg_S/cm^2. Celgard 2500 separators (19mm diameter) were cut and stored similarly. CR2032 coin cells were fabricated in the glovebox by adding 30 μL of either organic electrolyte ("OE," 1M LiTFSI in DOL:DME [1:1 v/v] + 1wt% $LiNO_3$) or Li(G4)TFSI to a separator/cathode stack, followed by a Li/SS anode prepared as described above, then closing the cell with an electric coin cell crimping machine (MSK-160D, MTI Corp).

5.2.7 *Fabrication of Symmetric Cells*

For Li symmetric cell fabrication, lithium chips were polished and pressed onto roughened SS discs, as described previously. 19mm diameter separators (SIG 1/Celgard or Li(G4)TFSI prewetted into Celgard) were inserted between the chips, and the whole assembly placed into CR2032 coin cells which were sealed using an electric crimping machine. SS symmetric cells were fabricated by sandwiching either an S/C/SIG cathode or a SIG 1/Celgard separator between smooth, clean SS discs, then placing whole assembly into CR2032 coin cells which were sealed using an electric crimping machine.

5.2.8 *Electrochemical Measurements*

All C-rates were calculated based on the theoretical gravimetric specific capacity of sulfur (1C = 1.672 mA/g_S). Galvanostatic cycling tests were performed at 30°C using an Arbin BT-2043 battery tester connected to an environmental chamber; typically, cells were preconditioned at C/20 for the first discharge and second cycle, followed by sustained cycling at C/10. Voltage limits were set 1.9-2.8V for cells with organic electrolyte, and 1.5-3V for all others. The reported cell data was selected to be generally representative of behavior for many different cells of the same design. Galvanostatic intermittent titration technique (GITT) data was collected on preconditioned cells during the 3rd cycle. Charge/discharge was interrupted every 20 min with a 1 h rest, allowing the cell to relax to its open circuit voltage (OCV); this continued until voltage limits were reached. Temperature-dependent electrochemical impedance spectroscopy (EIS) of cells was performed from 7MHz-100mHz in an environmental chamber using a CH Instruments Model 660E Electrochemical Workstation. Temperature-dependent ionic conductivity of SIG 1/Celgard was measured by sandwiching a 15mm diameter sample between smooth, clean SS discs, then performing impedance spectroscopy as described in Section 4.2.4.

5.3 Results and Discussion

5.3.1 *SIG/Celgard Composite Separators*

Although the previously-demonstrated SIGs are all free-standing solids with relatively high compressive toughness, their elastic moduli are <500kPa (see section 3.3.1) and I have found them to be poorly tolerant of tensile stress. This necessitates the fabrication of thick films (~250μm) to allow a reasonable amount of handling. However, LIB/LSB battery separators are typically limited to <50μm thickness to both minimize ohmic resistance and reduce cell volume, which begs the question of how to best utilize SIG electrolyte chemistry while limiting through-cell distance.

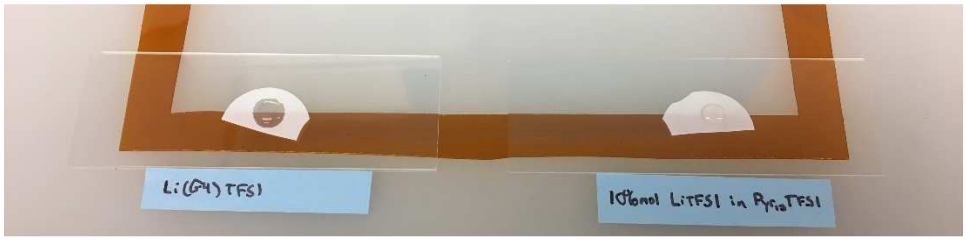

Figure 5.1. Photograph of Celgard 2500 films against a patterned background, with Li(G4)TFSI (left) or a ternary RTIL blend (right) added on top.

Commercial LIBs generally use porous polyethylene (PE) or polypropylene (PP) films as separators, which are readily wetted by organic electrolyte solvents. Celgard® 2500 (hereafter referred to as "Celgard") is a representative example, being a 25μm thick monolayer PP film with 55% porosity and 0.064μm pore size.[280] Notoriously, most RTILs appropriate for lithium battery usage cannot penetrate such separators, which has driven research into alternatives.[222] However, solvate ionic liquid Li(G4)TFSI does, in fact, wet Celgard, albeit slowly due to its high viscosity (94.6 cP at 30°C).[194] This is illustrated in **Figure 5.1** below; porous PP is largely opaque when dry due to light scattering, but becomes transparent when soaked with organic liquids. Upon adding a drop of Li(G4)TFSI to Celgard, a piece of orange polyimide underneath becomes clearly visible, indicating full penetration of the SIL through porous PP. In comparison, a drop of ternary

RTIL electrolyte (10mol% LiTFSI in 1-butyl-1-methylpyrrolidinium TFSI) fails to cause any optical change, indicating no penetration of this liquid.

In light of this information, I fabricated novel composites by thoroughly wetting SIG 1 precursor resin into a Celgard film, then heating between non-stick glass plates to cure the gel *in-situ* within the pores of the PP (**Figure 5.2**). SIG 1 was chosen due to its comparatively lower viscosity, commercially-available precursors, and ease of fabrication. Solvent diluents were avoided so as to discourage through-diffusion of Li_2S_x in LSBs. The resulting separator films possess the chemical characteristics of SIG 1 but the mechanical toughness of porous PP, allowing them to be easily handled despite only 40µm average thickness.

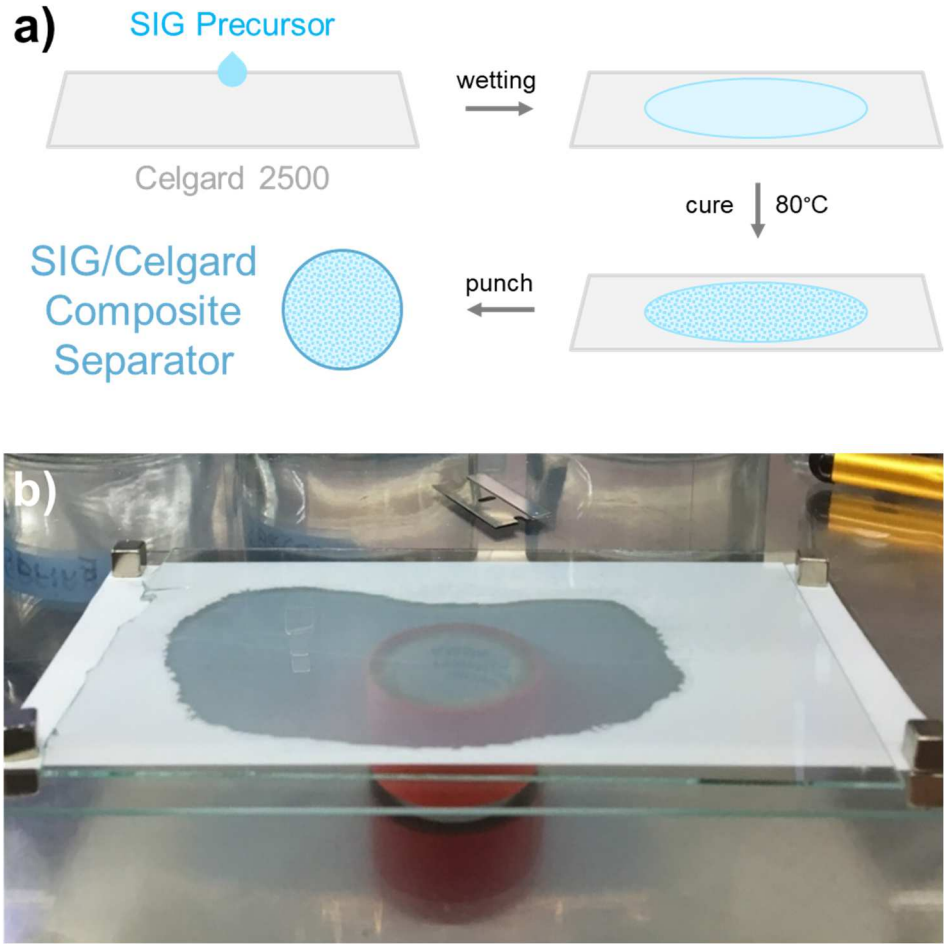

Figure 5.2. a) Schematic of the fabrication process for SIG/Celgard composite separators. **b)** Image of a cured SIG 1/Celgard composite, with red tape underneath to show its transparency.

Temperature-dependent ionic conductivity of the composite separators was measured between 30-80°C (**Figure 5.3**) and the corresponding VTF parameters presented in **Table 5.1** (see Section 4.3.2). SIG 1/Celgard has a bulk ionic conductivity of 0.38 mS/cm at 30°C, roughly half that of SIG 1 itself. This is an expected effect of the porosity/tortuosity introduced by Celgard, in agreement with previous reports,[281] and still acceptable for room-temperature battery operation.

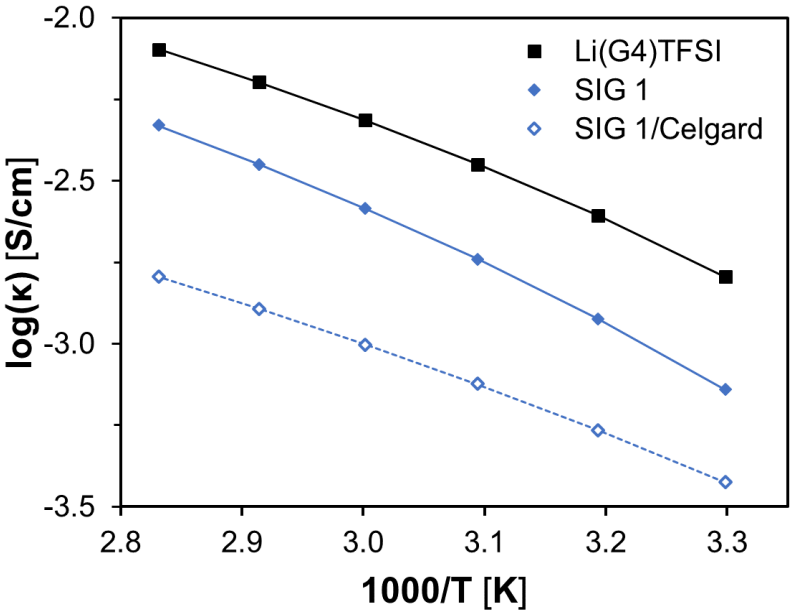

Figure 5.3. Temperature-dependent ionic conductivity (points) and VTF curve fits (dotted line) for SIG 1/Celgard between 30-80°C. Data for Li(G4)TFSI and SIG 1 reproduced from Figure 4.8 for comparison.

Table 5.1. Conductivity at 30°C and VTF parameters obtained for SIG1/Celgard. Data for Li(G4)TFSI and SIG 1 reproduced from Table 4.1 for comparison.

	$\kappa_{30°C}$ [S/cm]	κ_0 [S/cm]	$E_{a,ion}$ [J/mol]	T_0 [K]
Li(G4)TFSI	1.60×10^{-3}	2.30×10^{-1}	4.32×10^{3}	198
SIG 1	7.24×10^{-4}	2.49×10^{-1}	5.20×10^{3}	196
SIG 1/Celgard	3.76×10^{-4}	9.00×10^{-2}	6.33×10^{3}	164

In fact, a quick calculation reveals that anode interfacial resistance still outweighs bulk ohmic resistance by far. Using previously-determined parameters for Li(G4)TFSI and SIG 1, R_{int} for Li|SIG 1/Celgard is predicted to be a full order of magnitude larger than R_{bulk} at 0.1 mA/cm^2. However, R_{tot} is still reduced by 30% compared to Li(G4)TFSI/Celgard or 19% compared to freestanding SIG 1, demonstrating the utility of this composite approach. Notably, this calculation does not include polarization *a.k.a.* concentration overpotential, which is more difficult to predict from basic material properties, [264] but since this parameter is related to transference number through D_{Li+}, it is expected that SIG 1/Celgard should benefit from the improved t_{Li+} of SIGs relative to Li(G4)TFSI (see Section 3.3.1).

Table 5.2. Expected overpotential of Li anode + separator (excluding polarization) at 0.1 mA/cm^2 for three electrolyte/separator systems: Li(G4)TFSI wetted into Celgard 2500, a freestanding film of SIG 1, and SIG 1 wetted into Celgard 2500. The conductivity of Li(G4)TFSI/Celgard was estimated as 2.5x less than the SIL itself.[281]

	Li(G4)TFSI/ Celgard	**SIG 1 (freestanding)**	**SIG 1/ Celgard**
$\kappa_{30°C}$ [S/cm]	6.4×10^{-4}	7.24×10^{-4}	3.76×10^{-4}
A [cm^2]	1.911	1.911	1.911
***l* [μm]**	25	256	40
R_{bulk} [Ω]	2.04	18.5	5.57
R_{int} [Ω]	79.4	51.0	51.0
R_{tot} [Ω]	**81.4**	**69.5**	**56.6**
η_{an+sep} [mV]	**15.33**	**13.3**	**10.8**

In order to directly test the suitability of SIG 1/Celgard for real systems, Li symmetric cells were fabricated and cycled at ±0.1 mA/cm^2 (**Figure 5.4a**). After an initial induction period, the overpotential of SIG 1/Celgard stabilizes at 55mV, in comparison to 90mV for Li(G4)TFSI/Celgard. Quite a large percentage of this may be attributable to polarization effects, since the combined overpotentials predicted by **Table 5.2** are 11mV and 16mV, respectively. Clearly, SIGs with higher t_{Li+} must be developed to minimize polarization; however, the improved Li^+ transport characteristics of SIG 1 still generate a major reduction in overpotential compared to neat Li(G4)TFSI. Furthermore, the overpotential of Li(G4)TFSI/Celgard increases rapidly with continued cycling, eventually becoming erratic and then dropping rapidly, indicating a dendrite-related short-circuit. On the other hand, SIG 1/Celgard continues to cycle stably with only moderately-increased overpotential (90 mV) after 400 h, probably attributable to SEI growth.

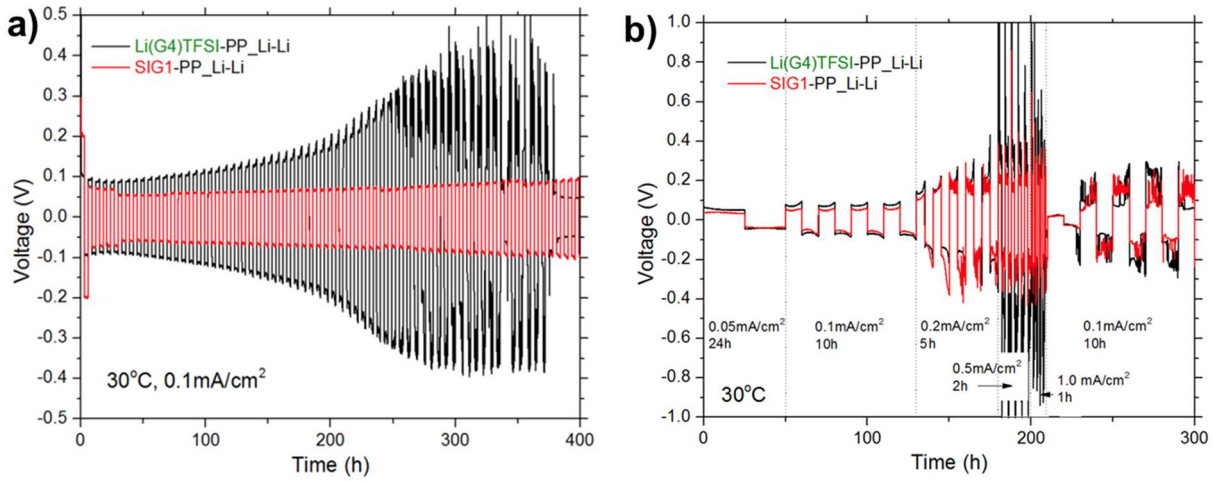

Figure 5.4. a) Cycling behavior of Li symmetric cells (30°C, ±0.1 mA/cm^2, ±0.3 mAh/cm^2) containing Celgard 2500 prewetted with Li(G4)TFSI *vs.* a SIG1/Celgard separator, and **b)** comparison of their performance from 0.05-1.0 mA/cm^2.

To compare performance at other current densities, Li symmetric cells with both types of separator underwent cycling at ±0.1-1 mA/cm^2, with ±1 mAh/cm^2 total charge passed in each case. A 24h preconditioning cycle at ±0.05 mA/cm^2 was performed for both cells in order to establish a

stable SEI layer and Li morphology. However, the overpotential becomes erratic for both materials starting at 0.2 mA/cm^2, a behavior which has been linked to rapid growth of a highly-resistive SEI,[282] although the voltage "spikes" are less severe in SIG 1/Celgard at 0.5 and 1.0 mA/cm^2. Further work is required to better understand this behavior.

5.3.2 *Rational Design of QSS LSBs with Integrated SIG Electrolyte*

Despite the improved wetting behavior of Li(G4)TFSI compared to other RTILs, its high viscosity still poses a significant challenge to cell integration. This is especially true in LSBs using mesoporous S/C composites, where electrolyte must thoroughly penetrate the highly-tortuous cathode, coat a large amount of surface area, and navigate pores as small as 2nm. Gelating agents further complicate the picture, and I have noted increased viscosity even in SIG precursor resins containing only "pre-polymer" P_{750}.

Prompted by these challenges, I have developed a novel electrode fabrication method which relies on existing, scalable manufacturing techniques but produces a fully-integrated, mechanically-stable cathode composite containing an intimate mixture of S/C composite and SIG electrolyte (**Figure 5.6**). This S/C/SIG cathode can be "dropped in" to existing cell fabrication processes, but requires no additional electrolyte to function.

Traditional cathode manufacturing processes start from a slurry of the desired materials in a carrier solvent, usually NMP. This slurry is blade-coated, slot-die-coated, *etc.* onto an aluminum foil substrate, and the solvent is gradually removed by heating to produce a porous composite. During cell fabrication, the cathode must then be re-wetted, this time with electrolyte. My process instead replaces carrier solvent with the electrolyte itself – a SIG precursor resin. This liquid becomes intimately mixed with all solid particles during the slurry mixing process, bypassing the need for re-wetting later on. Since Li(G4)TFSI and PEGDMA are non-volatile under ambient

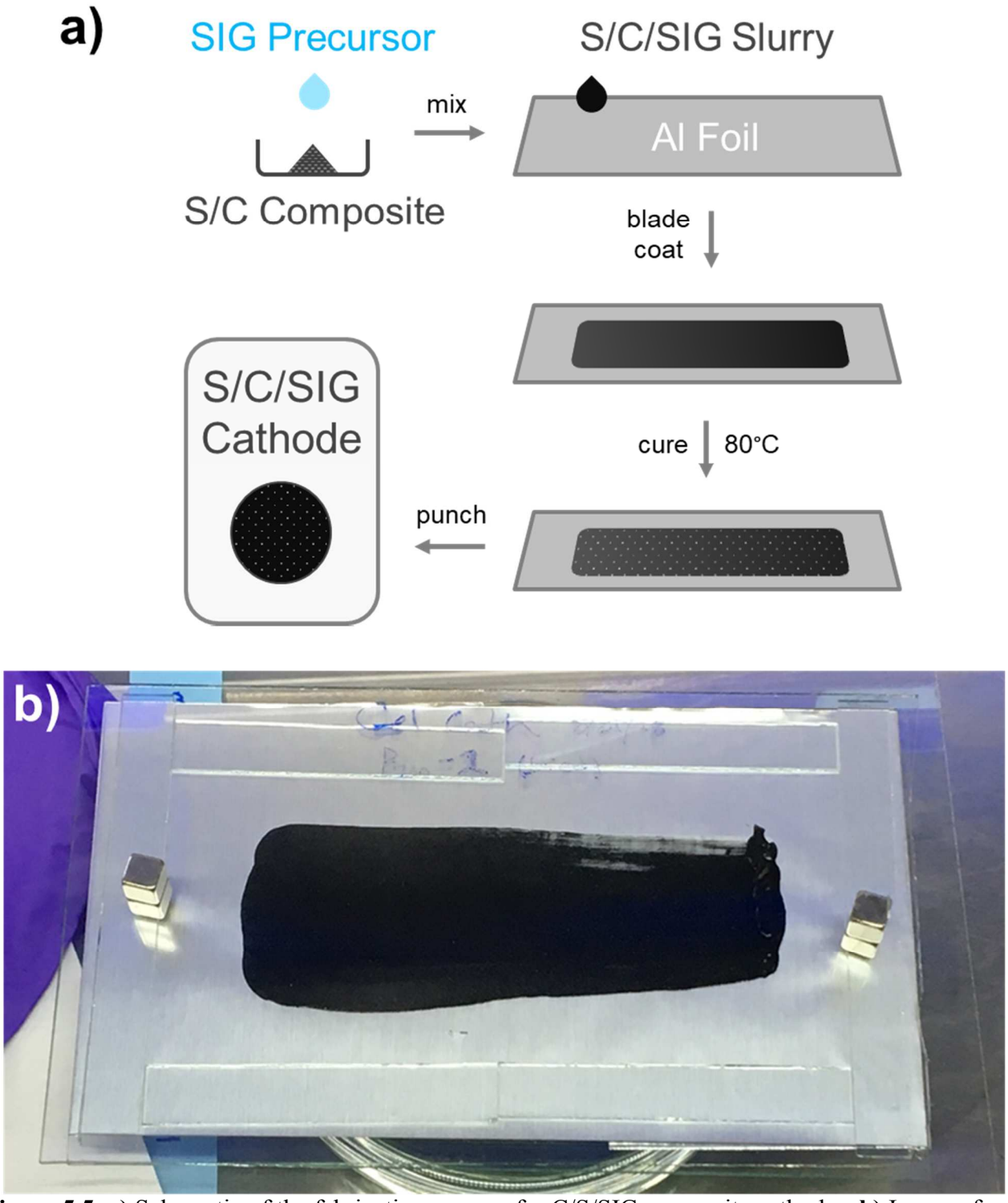

Figure 5.5. a) Schematic of the fabrication process for C/S/SIG composite cathodes. **b)** Image of a cured C/S/SIG film. This early trial used glass spacers, which were later replaced by an EPDM rubber spacer.

conditions, the resulting slurry may be processed with minimal risk of drying out. Once coated onto a foil substrate, heating the S/C/SIG slurry initiates crosslinking of PEGDMA *in-situ* around the percolation network of particles, forming a bi-continuous transport network for electrons and Li^+ ions. This cathode design is also "binderless," since the crosslinked SIG functions as both an electrolyte and a mechanical support network.

The resulting S/C/SIG cathodes may combined with SIG/Celgard composite separators (as described above) and Li metal to produce quasi-solid-state lithium-sulfur batteries (QSS LSBs, **Figure 5.6**). Since the cathode and separator both contain high concentrations of mobile Li(G4)TFSI, they laminate together readily, in comparison to many solid-state designs where interfacial contact is a major challenge.[230] No additional electrolyte is required, eliminating the electrolyte addition/wetting step of cell fabrication. This cell can only be considered "quasi-solid-state" since the majority of electrolyte volume still consists of liquid, albeit macroscopically immobilized as a gel. Nonetheless, every component is entirely free-standing with minimal volatile content, making it functionally near-identical to a true solid-state battery. To my knowledge, this represents the first-ever report of an LSB containing SIG electrolyte.

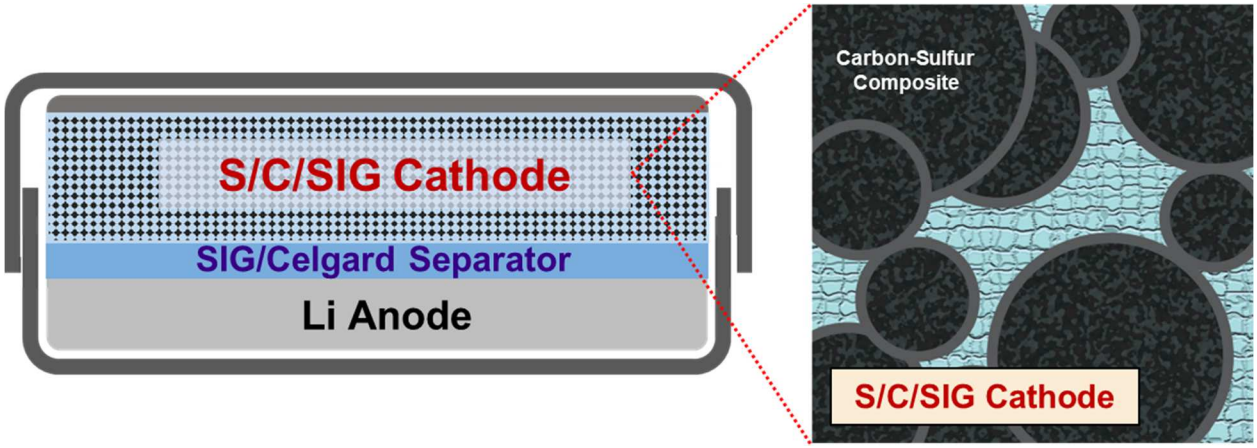

Figure 5.6. Overview of the quasi-solid-state (QSS) Li-S cell design, consisting of SIG-impregnated composites laminated together with Li metal. Close-up schematic depicts internal cathode structure with bi-continuous electron and ion transport pathways.

Practically-speaking, I found it helpful to add a small amount of organic solvent diluent to the cathode slurry. This diluent reduces resin viscosity to speed infiltration into the solid powder, promotes even dispersion of carbon particles during mixing, and (if not removed prior to cure) improves ion transport in the final SIG composite. Hypothetically, a solvent may also influence electrochemical behavior of the cell due to effects on Li_2S_x conversion (see Section 2.1.2). Initially, I investigated 1,4-dioxane for this role, and successfully produced functioning cells. However, the volatility of dioxane caused visible, time-dependent changes during both slurry processing and thermal cure, leading to poor reproducibility. This led me to investigate lower-volatility anisole as a diluent (see Section 4.3.4), culminating in the design of DSIG-C1, which was used thereafter to produce the results reported below, which were easily reproduceable between batches.

5.3.3 *Cycling Results and Comparison to Other Designs*

In order to assess the viability of my design strategy, I fabricated S/C/DSIG-C1 composite cathodes using a composite of 50wt% S_8 melt-diffused into mesoporous carbon MJ430, as previously described by myself and coworkers,[60] along with a small amount of Super C65 carbon black as a conducting additive. Excluding aluminum, the total sulfur content was ~5wt%; however, this calculation also includes the weight of electrolyte and "binder" due to the unique design and fabrication process. The sulfur content corresponds to a typical design with 50% inactive solids and an electrolyte/sulfur (E/S) ratio of 15 mL/mg. The composite cathodes were then laminated together with a SIG 1/Celgard separator and Li metal to produce QSS cells.

For comparison, I fabricated "traditional" sulfur cathodes using 50%S/MJ430, Super C65, and PVDF binder (see Section 5.2.6). To these cathodes were added either a standard organic electrolyte ("OE," 1M LiTFSI in DOL:DME [1:1 v/v] + 1wt% $LiNO_3$) or neat Li(G4)TFSI,

followed by a PP separator (Celgard) and Li metal to form a complete LSB. All cells were then cycled at 30°C, with the results plotted in **Figure 5.7** below.

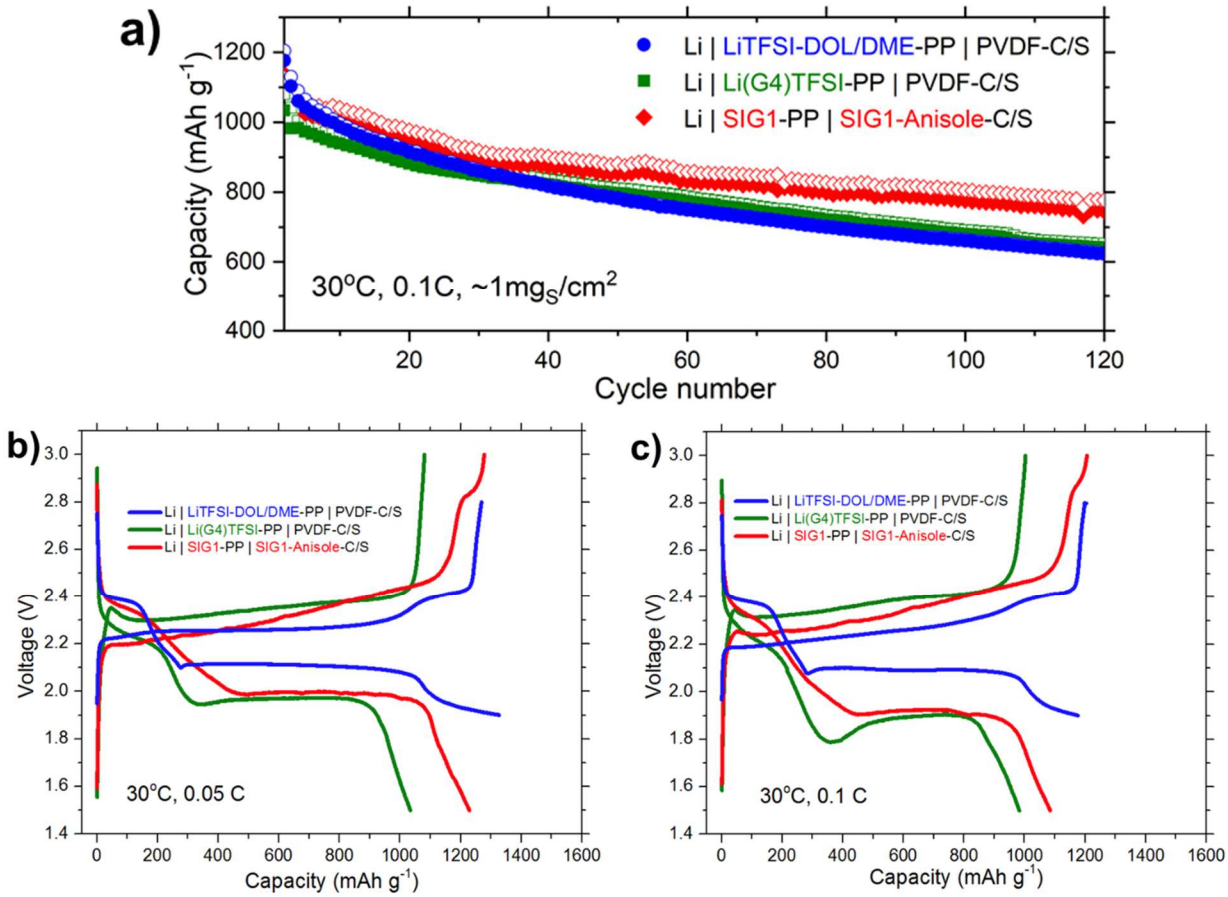

Figure 5.7. a) Cycling performance of a QSS cell at C/10, compared to cells with traditional S/C/PVdF cathodes and OE or Li(G4)TFSI liquid electrolyte. **b,c)** 2nd cycle voltage traces of all three cell designs at C/20 and C/10, respectively.

All three designs produced initial capacities >1000 mAh/g_S, decreasing in the order OE > > QSS > Li(G4)TFSI. However, the cell with organic electrolyte exhibited rapid capacity fading within the first ten cycles, as expected due to irreversible dissolution of highly-soluble Li_2S_x into the electrolyte. Capacity continued to decline at a slower rate long-term, with the cell retaining 661 mAh/g_S of its 2nd cycle capacity after 100 cycles (average 0.44% loss/cycle). The coulombic efficiency of this cell averaged 98.7% over this period – the best out of all designs. This is due to

the inclusion of $LiNO_3$ passivating additive, which mostly prevents redox shuttling in this case. It should be noted that, as seen above, coulombic efficiency often correlates poorly with capacity fade rate in LSBs. This is because a large portion of the efficiency loss comes from redox shuttling, which is a non-destructive process, and much of the remaining loss can be attributed to the anode, which is provided in large excess here. In contrast, nearly all processes that reduce coloumbic efficiency in LIBs result from irreversible capacity losses.

The cell with Li(G4)TFSI electrolyte produced the least initial capacity but also the least-rapid initial decline, a result of the reduced polysulfide solubility in this electrolyte. However, capacity fade accelerated somewhat over time, with only 680 mAh/g_S remaining after 100 cycles (0.35% average loss from cycles 2-100). Average coulombic efficiency was found to be 98.5% over this period, quite impressive for a cell lacking a specific anode-passivating element, which again is a testament to the ability of Li(G4)TFSI to prevent crossover of sulfur species. Notably, both "traditional" cells exhibited similar capacity fade rates after Cycle 60, possibly indicating that they share a long-term degradation mechanism unrelated to polysulfide crossover. Cathode passivation by Li_2S buildup may play a role in this behavior, and/or mechanical degradation of the electrical percolation network.

In contrast, the QSS cell exhibited both a large initial capacity (1173 mAh/g_S) and reduced capacity fading over 100 cycles (0.32% per cycle). Most of this loss occurs in the first 30 cycles, as the 100^{th} cycle discharge capacity (774 mAh/g_S) is noticeably higher than the other cells and declining at a visibly slower rate. The S/C/DSIG-C1 cathode to found to enable efficient sulfur conversion, likely enhanced by the polar PEG and/or anisole content of the SIG electrolyte as compared to neat Li(G4)TFSI.

The coulombic efficiency of the QSS cell averaged 96.1% over 100 cycles, somewhat less than the other designs, despite its lower capacity fade rate. This points towards redox shuttling as a likely culprit, caused by increased Li_2S_x solubility in the QSS system as compared to Li(G4)TFSI. Again, this is likely attributable to the PEG and/or anisole content of the SIG electrolytes, which provide Lewis-basic sites to coordinate Li^+ arising from Li_2S_x dissolution. Further optimization of the separator and better anode passivation may be able to reduce this effect.

Comparing the 2nd cycle charge/discharge voltages of these cells, several major differences are revealed. The OE cell exhibits classic four-stage discharge behavior (see Section 1.2.2), with an upper Stage I plateau at 2.4V and a lower Stage III plateau at 2.1V. A characteristic "dip" in voltage appears at the end of Stage II, which has been attributed to reduced electrolyte conductivity during the point of maximum Li_2S_x concentration.[283] Charge voltage exhibits similar stages in reverse, although the transitions between them are less well-defined due to the continuous presence of Li_2S. A voltage hysteresis of 150mV is evident between charge and discharge. Li(G4)TFSI electrolyte produces voltage behavior that is staged similarly to OE, but shifted downward/upward during discharge/charge by its much-larger internal resistance. The first discharge plateau also loses some of its "flatness," instead occurring over a range of 2.1-2.3V. This is a common feature in sparingly-solvating electrolytes, indicating the presence of competing conversion pathways.[189] The characteristic dip at the end of Stage II is more prominent and lasts longer, likely indicating a significant viscosity increase and/or poor Li_2S nucleation kinetics. A large "bump" is also present near the beginning of charge, indicating a large kinetic overpotential associated with re-oxidation of deposited Li_2S.

Once again, QSS cell behavior appears quite different: Stage I voltage is "smeared out" like in Li(G4)TFSI, but shifted upwards to 2.3-2.4V. On the other hand, Stage III occurs at the

same potential (~1.9V) as Li(G4)TFSI. These plateaus are connected by a long-lasting Stage II which contributes a significant fraction of total capacity and transitions smoothly to Stage III without a voltage minimum. This highly-unusual behavior is discussed in more detail below.

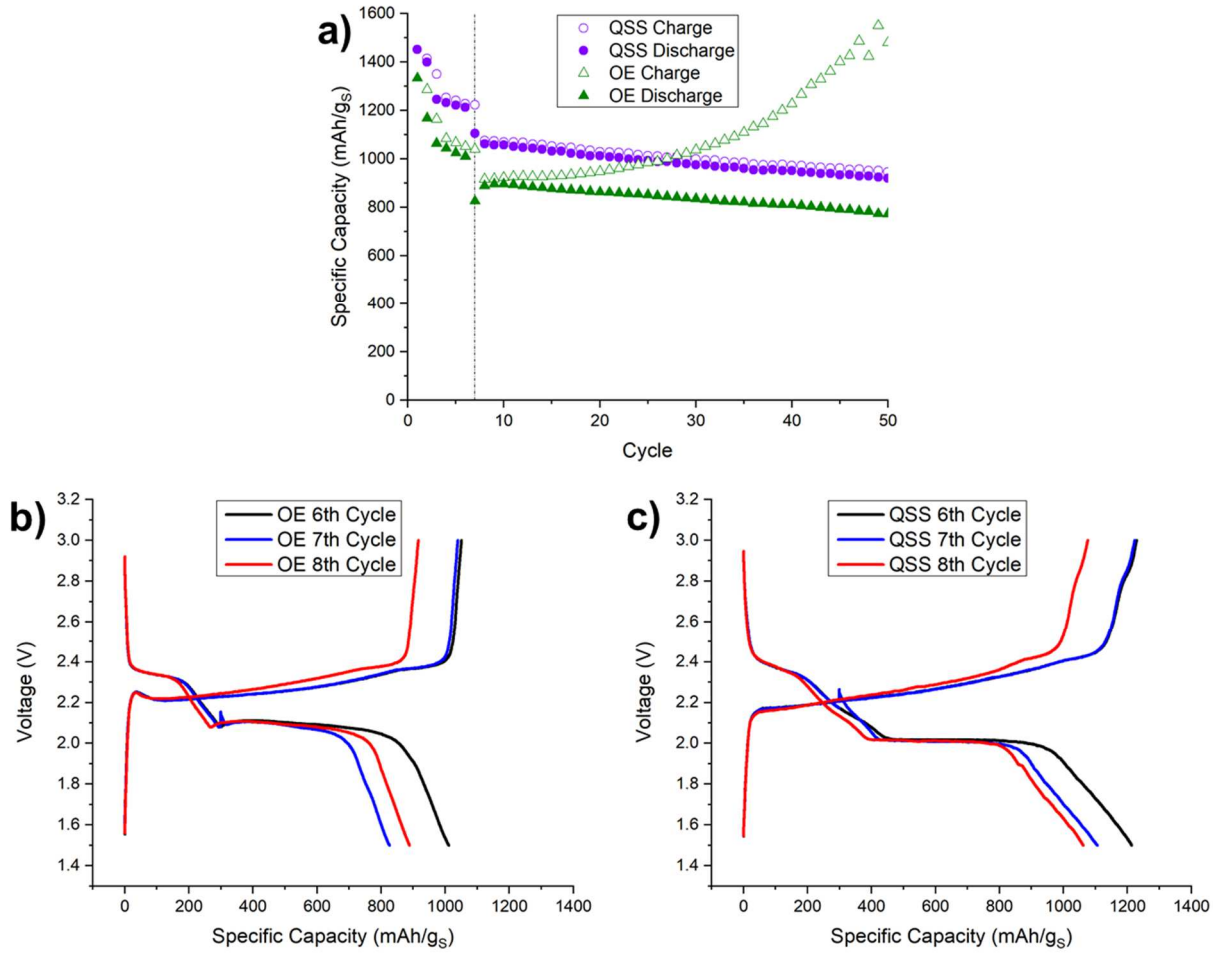

Figure 5.8. a) Self-discharge test of QSS cells *vs.* traditional cells with OE. 7th cycle discharge was interrupted at 300 mAh/g, and cells were rested for 100h before continuing. **b,c)** Voltage profiles during the 6th, 7th, and 8th cycles.

LSBs commonly struggle with self-discharge to a greater extent than LIBs, since dissolved Li_2S_x may gradually precipitate as insoluble Li_2S/Li_2S_2 *via* disproportionation and/or direct reduction at the anode. In order to test the ability of a QSS design to control this phenomenon, C/10 cycling of QSS and OE cells was interrupted with a 100 h rest during cycle 7, followed by

continued cycling. As a result, the OE-based design lost 185 mAh/g_S (18.3%) to self-discharge relative to the previous cycle, while the QSS cell lost only 108 mAh/g_S (8.9%). Interestingly, the OE cell recovered 63 mAh/g_S in the following cycle, bringing the total two-cycle loss to 12.1%, while the QSS cell lost an additional 44 mAh/g_S for a similar total of 12.5%. However, the OE charge/discharge capacities rapidly diverged after this point, strongly suggesting an accelerated redox shuttle effect. The QSS cell did not exhibit this behavior, instead cycling its remaining capacity stably with a coulombic efficiency of ~98%. This result is especially encouraging given the lack of anode-passivating additives in the QSS system. Hence, while we have observed that both designs are similarly susceptible to irreversible capacity loss during self-discharge, we have found that the QSS system is more resistant to continued degradation caused by the redistribution of sulfur species during prolonged rest.

5.3.4 *Origin of QSS Performance Characteristics*

While QSS LSBs have been demonstrated to possess improved capacity and retention over traditional designs, they also exhibit odd voltage profiles with henceforth-unseen characteristics. The voltage behavior of batteries under current flow has two fundamental determining factors: 1. the thermodynamic or open-circuit voltage (OCV) determined by the redox potentials of reactants at the electrode surface, and 2. overpotential caused by fluctuating internal resistances. Therefore, it was of-interest to determine whether the unique voltage profile of QSS cells results from the overpotentials of individual novel components, or whether DSIG-C1 causes significant changes to chemical pathway of sulfur conversion.

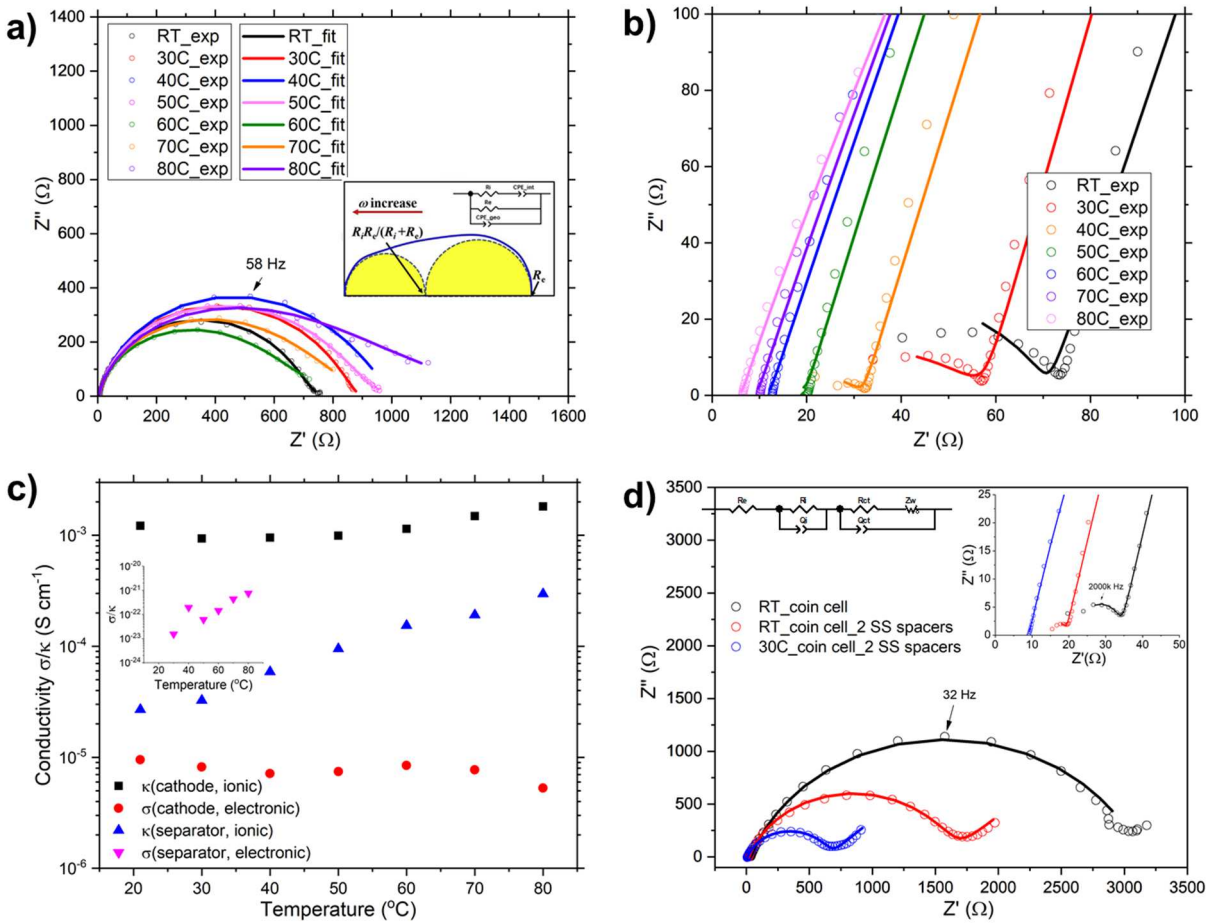

Figure 5.9. a) Nyquist plot of SS|S/C/SIG|SS impedance data at 30-80°C, with inset depicting the equivalent circuit model used for fitting and its expected shape. **b)** Nyquist plot of SS|SIG 1/Celgard|SS impedance data at 30-80°C. **c)** Summary of ionic/electronic conductivities measured for S/C/SIG and SIG 1/Celgard at 30-80°C. **d)** Nyquist plot showing effect of increased temperature and pressure on freshly-assembled QSS cell impedance.

As a first step, the ionic and electronic conductivities of S/C/DSIG-C1 cathodes and SIG 1/Celgard separators were separated and measured by EIS between blocking SS electrodes (**Figure 5.9**). Notably, the composite separator ionic conductivity was measured to be an order of magnitude lower in this experiment than previously, raising the serious possibility that these numbers are not quantitatively accurate, potentially due to poor interfacial contact with the SS electrodes. However, the qualitative trends still reveal useful information – namely, that the electronic conductivity of the cathode (10^{-5} S/cm) is significantly lower than its ionic conductivity

(10^{-3} S/cm). This situation is the opposite of what is typically found in LSB cathodes, and indicates a poorly-developed electron percolation network in S/C/DSIG-C1. More than likely, this is a side-effect of the fabrication process, since particle-particle distance remains mostly unchanged between the slurry and the final cathode. In contrast, a traditional cathode slurry densifies significantly during solvent evaporation. This may represent an intrinsic drawback which will require significant redevelopment of the cathode fabrication procedure to solve. However, some success was found in addressing this problem by increasing cathode pressure (**Figure 5.9d**).

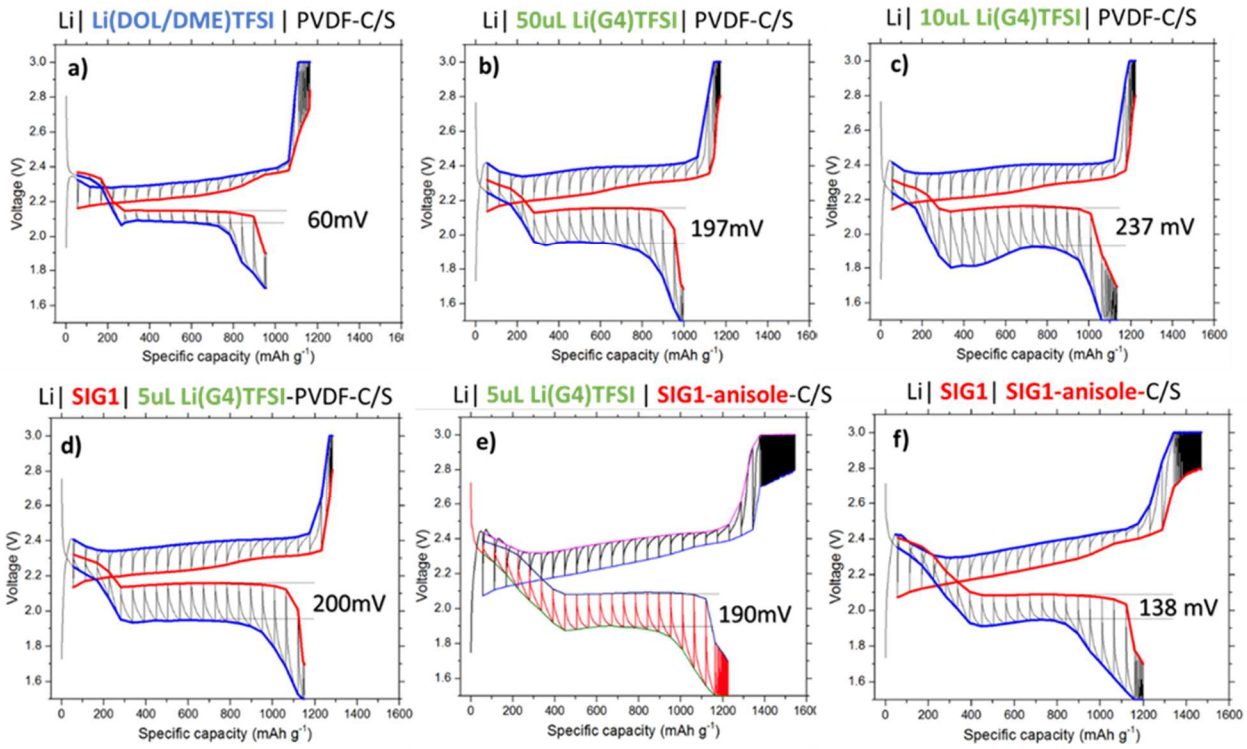

Figure 5.10. a-f) Comparison of galvanostatic intermittent titration technique (GITT) data for specified cell architectures – labeled with their Stage 3 discharge overpotential – demonstrating the effect of different design elements on overall cell voltage profile.

In order to directly more-directly observe the relative contributions of OCV and overpotential to QSS behavior, Galvanostatic Intermittent Titration Technique (GITT) tests were performed on Li-S cells with individual components systematically varied (**Figure 5.10a-f**). This

experiment allows direct measurement of cell overpotential as a function of state-of-charge, and from this, the shape of charge/discharge curves may be observed under open-circuit conditions. Since OCV depends solely on the electrochemical activities of reactive species within the cell, this provides insight into the chemistry of S/C/DSIG-C1 cathodes. For the sake of clear comparison, the points of least overpotential during Stage III of discharge are marked and labeled with values.

Unsurprisingly, the OE control cell (**Figure 5.10a**) exhibits the least overpotential, while the cell with a traditional cathode (S/C/PVDF) and a limited volume of SIL (**Figure 5.10c**) requires the most overpotential. This is due to large charge transfer resistance at both the anode/cathode of the latter cell and highlights the limitations of "dropping-in" electrolytes to cells that were not designed around their characteristics. Adding a large excess of SIL electrolyte (**Figure 5.10b**) alleviates overpotential slightly, most likely due to improved wetting of the cathode and a higher total capacity of sulfur species soluble in the electrolyte, which alleviates cathode charge transfer resistance somewhat. One the other hand, replacing the Li(G4)TFSI/Celgard separator with a SIG 1/Celgard separator (**Figure 5.10d**) gives a similar result without requiring an increase in total electrolyte volume, due to decreased resistance at both the anode and separator. This highlights a hidden utility of the integrated separator design: excess electrolyte is no longer required to ensure thorough wetting of the separator and anode.

Cells containing S/C/DSIG-C1 cathodes outperform all cell designs based on S/C/PVDF cathodes with Li(G4)TFSI electrolyte, with the lowest overpotential observed for the full QSS cell (**Figure 5.10f**). This may be partially attributed to improved cathode wetting achieved during fabrication, as well as the influence of polysulfide-solvating PEG and anisole, which may act to reduce charge-transfer overpotential in the cathode and suppress passivation, as previously postulated for PEG.[49] Suspiciously, the total overpotential (138mV) during Stage III is less than

that predicted from cathode electrical conductivity alone (142mV), further casting doubt on the accuracy of the conductivity measurement. If the "real" value of electrical conductivity is assumed to be an order of magnitude higher than measured (still quite low!) and combined with the expected single-anode resistance at this current density (~0.2mA/cm^2), it is possible to assert that cathode electrical resistance and anode/separator resistance contribute roughly half of the total observed overpotential (~70mV) in QSS cells. Since cathode ionic conductivity seems too large to be a major contributor, the remaining overpotential must be due to charge-transfer processes associated with sulfur conversion in an S/C/DSIG-C1 electrolyte.

Interestingly, OCV in cells with S/C/DSIG-C1 cathodes still exhibits the same unusual features as current-applied voltage, including a poorly-differentiated, sloped Stage I + II region which contributes ~400 mAh/g$_S$ to the total capacity. This value bears striking resemblance to the theoretical capacity of the reaction $S_8 + 4Li^+ + 4e^- \rightarrow Li_2S_4$ (418 mAh/g$_S$), the predicted end-product of Stage II. Comparing OCV regions between designs, it is clear that sulfur conversion does indeed begin at a higher potential in DSIG-C1 (2.4V vs 2.35V) compared to Li(G4)TFSI and end at a lower potential (2.075V vs 2.125V), indicating an altered conversion pathway. SIG 1/Celgard also has a subtle effect on OCV, shifting it upwards by ~25mV. This suggests an increased activity coefficient of Li^+ in SIG 1 compared to Li(G4)TFSI.

The current-applied discharge overpotential of S/C/DSIG-C1 cells does not appear to fluctuate until the end of Stage III (~800 mAh/g$_S$), where the onset of growing overpotential due to cathode passivation causes a broad downward slope. OCV continues to display a plateau, however, until 1100 mAh/g$_S$. In combination with the observance of near-theoretical Stage I + II capacity, these results suggest that cathode passivation is the major capacity-limiting factor in QSS

cells. Control of Li_2S morphology in SIG electrolytes may be an optimal target for future development.

Without detailed *in-situ* chemical characterization, it is difficult to suggest any specific changes to conversion pathway as the source of voltage behavior in S/C/DSIG-C1 cathodes. However, the trend of higher first-plateau voltage concurrent with lower second-plateau voltage would appear to indicate that medium-chain polysulfides *i.e.* Li_2S_4 are preferentially stabilized in DSIG-C1 electrolyte. This might also explain why near-complete conversion between S_8 and Li_2S_4 is observed. Regardless, the ability of QSS cells to approach total conversion of S_8 into intermediate products is a testament to the excellent integration of electrolyte and S/C composite achieved with by the *in-situ* fabrication method. Clearly, it is possible to optimize the cell performance of sparingly-solvating electrolytes by approaching LSB design from a molecular engineering perspective.

5.4 CONCLUSION

In conclusion, I have demonstrated a novel quasi-solid-state (QSS) LSB design which integrates solvate ionogel electrolyte (SIG) into the separator and cathode *via* an *in-situ* thermal crosslinking method. These fabrication methods ensure near-ideal contact of electrolyte with active materials while producing freestanding composites which can be laminated together to produce working cells. These QSS cells are found to outperform traditionally-constructed cells – with either organic electrolyte or Li(G4)TFSI electrolyte – over extended cycling at C/10 and 30°C, retaining 774 mAh/g_S after 100 cycles with an average coulombic efficiency of 96.5%, despite the absence of $LiNO_3$ or other anode-passivating components. These results represent, to my knowledge, the first-ever report of Li-S cell operation in a SIG electrolyte. Further work is suggested to deduce the conversion mechanism and reduce overall cell impedance.

Chapter 6. CONCLUSION

6.1 SUMMARY OF FINDINGS

This doctoral dissertation has focused on my efforts to develop and study free-standing solvate ionogel (SIG) electrolytes, successfully integrate them into working batteries, and demonstrate their effects on cell performance. I have focused in particular on aspects of SIG fabrication and performance relevant to lithium-sulfur batteries (LSBs), such as basic Li^+ transport properties and Li stripping/plating overpotential. Chapter 1 introduced the motivating factors behind this research, basic Li-S operating principles, and major functional challenges in the system. Chapter 2 reviewed the existing literature on Li-S chemistry and cell design, including common strategies to improve cell performance. Chapters 3-5, which cover my own research in detail, are summarized below.

6.1.1 *Solvate Ionogel Electrolytes with Fast Room-Temperature Lithium Transport*

Lithium solvate ionic liquids (SILs), made from an equimolar mixture of a chelating solvent (*e.g.* tetraglyme or "G4") with a non-coordinating lithium salt (*e.g.* LiTFSI), possess a unique combination of physical and electrochemical properties which make them imminently suited to tackle performance issues in LSBs. In particular, Li(G4)TFSI – having an ionic conductivity 1.6×10^{-3} S/cm at 30°C,[194] Li_2S_x solubility <100mM$_S$ for all polysulfide lengths,[214] thermal stability up to 200°C,[198] and liquid range down to -54°C[196] – appears especially promising for a sparingly-soluble cathode design. This electrolyte may also help to mitigate dendrite growth at the lithium metal anode, given the ability of highly-concentrated electrolytes to resist space-charge formation (see Section 2.2.1). Finally, unlike traditional RTILs, Li(G4)TFSI

can be produced cheaply and easily from tetraglyme (G4) and LiTFSI, both of which are already manufactured at-scale.

Li(G4)TFSI can be immobilized in a crosslinked polymer network to form a free-standing electrolyte known as a solvate ionogel (SIG), which presents an opportunity to improve the safety and energy density of devices, as well as introduce additional molecular functionality. However, only a small number of SIGs have been reported,[223–225] and the design rules in this system are unclear. In Chapter 3, based on my previously-published report,[218] I presented a series of SIGs containing Li(G4)TFSI gelated by radical crosslinking of poly(ethylene glycol) dimethacrylate (PEGDMA) in combination with functional methacrylates or an inert molecular solvent (1,4-dioxane). Through careful design of both polymer structure and liquid composition, I demonstrated the potential to control properties such as conductivity (κ) and lithium transference number (t_{Li+}) to exceed 2×10^{-3} S/cm and 0.5, respectively. Additionally, I uncovered a significant dependence of lithium transport on PEG chain length and crosslinking status in SIGs, which may be due to an interplay between competitive Li^+ binding and "diluent-like" mobility enhancement that changes for PEG above the entanglement limit (~2kDa). These novel SIGs may be used in lithium metal batteries, with best-performing formulas able to strip/plate lithium for >600h (100 cycles) at 0.1 mA/cm^2 without short-circuiting. My results also suggested future areas for SIG optimization, such as reduction of competitive Li^+ binding, reduction of lithium interfacial resistance, and improved toughness. The combination of simple fabrication, excellent Li^+ transport, and metallic lithium compatibility make SIGs attractive for "beyond Li-ion" battery designs, including LSBs.

6.1.2 *Probing the Effect of Polymer Structure and Liquid Composition on Solvate Ionogel Electrolytes*

Building upon my previous work, in Chapter 4 I further investigated the two molecular "handles" with which to tweak SIG properties: solid polymer structure and liquid diluent composition. The polymer structure may be altered by 1. adjusting network properties such as M_w between crosslinks and density of crosslinks, 2. adding/removing molecular functionality, or 3. changing the polymer backbone structure. Since my first reported focused primarily on the first two strategies, it seemed prudent to investigate the third, especially in regards to the question "Can competitive Li^+ binding be minimized without sacrificing the beneficial diluent effect?" Additionally, while 1,4-dioxane was selected for my initial study based on a limited survey of common solvents, it is by no means the best possible choice for DSIGs. Dioxane's low dielectric permittivity of 2.3 does not encourage efficient charge separation, and permittivity has been linked to conductivity in diluted RTILs, including Li(G4)TFSI. Dioxane also has a low-medium boiling point of 101°C, which is not ideal given that curing step of SIG fabrication involves a temperature hold at 80°C. I postulated that increasing both of these parameters should lead to a DSIG with better properties.

To these ends, I reported the fabrication and properties of a free-standing gel electrolyte based on Li(G4)TFSI and poly(propylene glycol) dimethacrylate (PPGDMA). The temperature-dependent ion transport and charge transfer properties of PEG- and PPG-based SIGs were measured in comparison to Li(G4)TFSI. Due to atacticity and/or steric hindrance, PPG was found to interact less-strongly with Li(G4)TFSI, as evidenced by lower values for the limiting conductivity κ_0, activation energy of ion transport $E_{a,ion}$, and lithium transference number t_{Li+}. Additionally, thermal measurements indicated less free glyme in PPG-based SIG, as compared to

PEG. Overall, slightly-improved room-temperature conductivity was observed for PPG-based SIG 1P (0.79 mS/cm) as compared to otherwise-identical, PEG-based SIG 1 (0.72 mS/cm). Additionally, measurement of temperature-dependent R_{int} in Li symmetric cells revealed that the reduced stripping/plating overpotential in SIGs compared to SILs originates from improved exchange current density i_o.

Finally, I made the first report of methoxybenzene *a.k.a.* anisole as a superior solvent diluent for Li(G4)TFSI, enhancing room-temperature conductivity by >700% at 1:1 dilution. Anisole was incorporated into the SIG 1 formula at 13.3vol% to produce DSIG C1, and the solvent was found to significantly decrease $E_{a,ion}$ and Vogel temperature T_0, resulting in a doubling of room-temperature conductivity from the original SIG 1 (1.44 mS/cm). Altogether, DSIG C1 showed tremendous promise as an electrolyte for LSBs.

6.1.3 *Quasi-Solid-State Lithium-Sulfur Batteries based on Solvate Ionogel Electrolytes*

All-solid-state designs are generally desirable for lithium secondary batteries, including LSBs, since they may improve safety, simplify fabrication, and eliminate structural "dead weight."[66] Additionally, the previous chapters of this dissertation discussed at-length the myriad specific advantages of Li(G4)TFSI-based solvate ionogels (SIGs) for LSBs, including spatial control of Li_2S_x diffusion, Li dendrite prevention, and elimination of flammable/gas-generating organic electrolytes. While SIGs have been demonstrated to possess good lithium transport properties and acceptable Li stripping/plating performance, I was unaware of any existing literature on the use of SIGs in an LSB system, potentially due to the difficulty of wetting highly-distributed sulfur in a S/C composite cathode with an ionogel electrolyte (by definition, immobile).

Therefore, in Chapter 5 I reported a novel fabrication method for separator and S/C cathode composites containing solvate ionogels, both of which demonstrate excellent bulk conductivity

due to intimate contact between components. These composites were combined with a Li metal anode to produce, for the first time, a quasi-solid-state (QSS) LSB based on SIG electrolyte. The electrochemical performance of this design was explored in detail, including its galvanostatic cycling performance and the origin of various overpotentials. A QSS design was found to outperform traditionally-constructed LSBs with both organic and SIL-based electrolytes, retaining 774 mAh/g_S (66% of initial capacity) after 100 cycles at C/10 and maintaining an average coulombic efficiency of 96.5% without any passivating additives. This design also resists self-discharge and its after-effects. Unusual voltage profiles were observed in QSS cells and found to originate from altered reaction pathways. The major sources of overpotential were found to be cathode charge transfer resistance and poor electronic conductivity, as well as interfacial resistance at lithium metal. These results demonstrate the viability of ionogel-based LSBs and suggest a path to high-performance using integrated molecular design.

6.2 Suggested Extensions of This Work

6.2.1 *High-Loading, Low E/S QSS Cells*

While the QSS cell results presented here demonstrate promising performance and serve as an effective proof-of-concept, a commercially-viable LSB must possess a cathode mass loading of >4 mg_S/cm^2, an E/S ratio of <3 mL/mg_S, and minimal lithium metal beyond what is required to match cathode capacity. My cathode fabrication strategy is certainly amenable to producing high loadings, which I have done; however, the resulting film thicknesses can reach 0.6-1mm due to low overall sulfur content in the slurry. Furthermore, due to the coupling of electrolyte composition and slurry composition in my process, it is difficult to dramatically adjust electrolyte content while maintaining a flowable slurry consistency. On the other hand, if processing challenges can be solved, this *in-situ* fabrication approach may help to minimize the negative effects of low E/S ratio

due to optimized electrolyte/sulfur contact. A "wet sand" approach may prove more successful than a slurry-based approach; regardless, there is plenty of room for future QSS cell optimization.

6.2.2 *Detailed Study of Conversion Chemistry in (D)SIGs*

The chemical origin of S/C/DSIG-C1 cathode performance characteristics has not been thoroughly characterized, due to a lack of readily-available techniques. Solid-state structures might be probed by X-ray absorption near-edge spectroscopy (XANES) or X-ray diffraction (XRD),[284] while more specialized electrochemical experiments may be able to extract parameters such as cathode exchange current and Li_2S_x solubility in DSIG-C1 for differing values of *x*. In particular, Li_2S formation and utilization must be studied in order to prevent early passivation of cathode surfaces, which has been implicated as one of the major remaining hurdles in LSB research.[24]

6.2.3 *Alternate SIG Polymer/Crosslinker Structures*

The results detailed in this dissertation suggest that SIG gelating agents can promote efficient $[Li(G4)]^+[TFSI]^-$ charge separation by displacing $TFSI^-$ in the coordination shell of Li^+; however, closely-spaced coordinating species on the polymer backbone may displace G4, immobilizing Li^+ entirely. Therefore, an ideal gelating agent might contain strongly-polar moieties which are nonetheless prevented from chelating Li^+ due to steric hindrance, atacticity, or limited conformational freedom. As examples, poly(tetrahydrofuran)[116] or poly-N-[2,2-dimethyl-1,3-dioxolane)methyl]acrylamide[285] might be good candidate materials for testing. Alternately, I have observed that Li(G4)TFSI can be made miscible with perfluoropolyethers in the presence of a partially-fluorinated polar solvent such as TTFE or 1,1,1-trifluorotoluene. These polymers are almost totally nonpolar, but also quite flexible, and remain non-viscous liquids down to cryogenic temperatures. A crosslinked, highly-fluorinated SIG could possess interesting properties.

Additionally, I came up with the concept of a SIG 1/Celgard composite separator due to the poor tensile toughness of SIGs, especially those based on P_{750}. If SIGs can be strengthened significantly without sacrificing ionic conductivity $>10^{-3}$ S/cm, this may eliminate the need for a porous separator entirely. Multifunctional crosslinkers such as trimethylolpropane trimethacrylate could present a possible route to achieving this, in addition to interpenetration of the crosslinked SIG with a higher-M_w, chemically-compatible polymer.[143]

6.2.4 *Single-Ion-Conducting SIGs*

In a similar fashion to the SIG 4 material reported in Chapter 3, it should be possible to create SIGs with non-coordinating anions tethered to the polymer chain. When paired with a $[Li(G4)]^+$, this would have the effect of discouraging Li dendrite growth while simultaneously boosting t_{Li+}. Taken to the extreme, a single-ion-conducting SIG could be imagined in which all anions are tethered, but Li^+ maintains high mobility due to the shielding effect of G4 coordination.

6.2.5 *Reduction of Li|SIG Overpotential*

Combined results from Chapters 4 and 5 have implicated low exchange current density and cell polarization as the two largest factors in the relatively high Li stripping/plating overpotential observed for SIGs. While the latter may be improved by optimizing t_{Li+}, the route to improving exchange current density is less clear, as it is unknown what its primary determining factors are in SIG electrolytes. Reduced microviscosity and improved ionicity are almost certain to help, although the impact of higher current density on Li morphology must also be considered.[277] In a similar vein, SEI-improving additives or Li pretreatment strategies must be developed which are compatible with SIG electrolytes. This would not only improve the coulombic efficiency of real cells, but may also have the effect of decreasing SEI-related resistance at the Li|SIG interface.

BIBLIOGRAPHY

[1] U.S. Energy Information Administration, "International Energy Statistics," can be found under https://www.eia.gov/beta/international/data/browser/, **n.d.**

[2] U.S. Energy Information Administration, *International Energy Outlook 2019*, **2019**.

[3] C. Pillot, *The Rechargeable Battery Market 2017-2025*, **2018**.

[4] Y. Akira, S. Kenichi, N. Takayuki, *Secondary Battery*, **1987**, US4668595 (A).

[5] R. Fu, T. Remo, R. Margolis, R. Fu, T. Remo, R. Margolis, *Natl. Renew. Energy Lab.* **2018**, 32.

[6] Battery University, "Safety Concerns with Li-ion Batteries," can be found under https://batteryuniversity.com/learn/article/safety_concerns_with_li_ion, **n.d.**

[7] K. Turcheniuk, D. Bondarev, V. Singhal, G. Yushin, *Nature* **2018**, *559*, 467.

[8] A. Scott, *C&EN Glob. Enterp.* **2019**, *97*, 18.

[9] J. W. Choi, D. Aurbach, *Nat. Rev. Mater.* **2016**, *1*, 16013.

[10] B. Jaskula, *Mineral Commodity Summary, Lithium*, **2019**.

[11] L. E. Apodaca, *Mineral Commodity Summary, Sulfur*, **2019**.

[12] P. G. Bruce, S. A. Freunberger, L. J. Hardwick, J.-M. Tarascon, *Nat. Mater.* **2012**, *11*, 19.

[13] D. Howell, in *U.S. Dep. Energy Veh. Technol. Off. 2017 Annu. Merit Rev. Peer Eval. Meet.*, Washington, D.C., **2017**.

[14] R. D. Rauh, F. S. Shuker, J. M. Marston, S. B. Brummer, *J. Inorg. Nucl. Chem.* **1977**, *39*, 1761.

[15] R. Steudel, T. Chivers, *Chem. Soc. Rev.* **2019**, *48*, 3279.

[16] M. Vijayakumar, N. Govind, E. Walter, S. D. Burton, A. Shukla, A. Devaraj, J. Xiao, J. Liu, C. Wang, A. Karim, S. Thevuthasan, *Phys. Chem. Chem. Phys.* **2014**, *16*, 10923.

[17] J. McMurry, *Organic Chemistry*, Cengage Learning, Mason, Ohio, **2008**.

[18] J. Gao, M. A. Lowe, Y. Kiya, H. D. Abruña, *J. Phys. Chem. C* **2011**, *115*, 25132.

[19] S. S. Zhang, *J. Power Sources* **2013**, *231*, 153.

[20] R. Steudel, *Angew. Chemie Int. Ed. English* **1975**, *14*, 655.

[21] C. Barchasz, F. Molton, C. Duboc, J.-C. Leprêtre, S. Patoux, F. Alloin, *Anal. Chem.* **2012**, *84*, 3973.

[22] H. Pan, J. Chen, R. Cao, V. Murugesan, N. N. Rajput, K. S. Han, K. Persson, L. Estevez, M. H. Engelhard, J. G. Zhang, K. T. Mueller, Y. Cui, Y. Shao, J. Liu, *Nat. Energy* **2017**, *2*, 813.

[23] F. Y. Fan, Y.-M. Chiang, *J. Electrochem. Soc.* **2017**, *164*, A917.

[24] J. Chen, W. A. Henderson, H. Pan, B. R. Perdue, R. Cao, J. Z. Hu, C. Wan, K. S. Han, K. T. Mueller, J. G. Zhang, Y. Shao, J. Liu, *Nano Lett.* **2017**, *17*, 3061.

[25] J. N. Chazalviel, *Phys. Rev. A* **1990**, *42*, 7355.

[26] X. B. Cheng, R. Zhang, C. Z. Zhao, Q. Zhang, *Chem. Rev.* **2017**, *117*, 10403.

[27] J.-G. Zhang, W. Xu, W. A. Henderson, *Lithium Metal Anodes and Rechargeable Lithium Metal Batteries*, Springer International Publishing, **2017**.

[28] K. H. Chen, K. N. Wood, E. Kazyak, W. S. Lepage, A. L. Davis, A. J. Sanchez, N. P. Dasgupta, *J. Mater. Chem. A* **2017**, *5*, 11671.

[29] H. Danuta, U. Juliusz, *Electric Dry Cells and Storage Batteries*, **1962**, US3043896A.

[30] M. L. B. Rao, *Organic Electrolyte Cells*, **1968**, US3413154A.

[31] R. D. Rauh, K. M. Abraham, G. F. Pearson, J. K. Surprenant, S. B. Brummer, *J. Electrochem. Soc.* **1979**, *126*, 523.

[32] E. Peled, A. Gorenshtein, M. Segal, Y. Sternberg, *J. Power Sources* **1989**, *26*, 269.

[33] B. Jin, J. U. Kim, H. B. Gu, *J. Power Sources* **2003**, *117*, 148.

[34] Y. Jung, S. Kim, *Electrochem. commun.* **2007**, *9*, 249.

[35] R. Kumar, J. Liu, J. Y. Hwang, Y. K. Sun, *J. Mater. Chem. A* **2018**, *6*, 11582.

[36] X. Ji, K. T. Lee, L. F. Nazar, *Nat. Mater.* **2009**, *8*, 500.

[37] D. Lv, J. Zheng, Q. Li, X. Xie, S. Ferrara, Z. Nie, L. B. Mehdi, N. D. Browning, J. G. Zhang, G. L. Graff, J. Liu, J. Xiao, *Adv. Energy Mater.* **2015**, *5*, 1.

[38] A. Swiderska-Mocek, E. Rudnicka, *J. Power Sources* **2015**, *273*, 162.

[39] L. Ma, H. L. Zhuang, S. Wei, K. E. Hendrickson, M. S. Kim, G. Cohn, R. G. Hennig, L. A. Archer, *ACS Nano* **2016**, *10*, 1050.

[40] H. M. Kim, H.-H. Sun, I. Belharouak, A. Manthiram, Y.-K. Sun, *ACS Energy Lett.* **2016**, *1*, 136.

[41] D. Lu, Q. Li, J. Liu, J. Zheng, Y. Wang, S. Ferrara, J. Xiao, J. G. Zhang, J. Liu, *ACS Appl. Mater. Interfaces* **2018**, *10*, 23094.

[42] Z. Wei Seh, W. Li, J. J. Cha, G. Zheng, Y. Yang, M. T. McDowell, P.-C. Hsu, Y. Cui, *Nat. Commun.* **2013**, *4*, 1331.

[43] Z. W. Seh, J. H. Yu, W. Li, P.-C. Hsu, H. Wang, Y. Sun, H. Yao, Q. Zhang, Y. Cui, *Nat. Commun.* **2014**, *5*, 5017.

[44] P. Y. Gu, Y. Zhao, J. Xie, N. Binte Ali, L. Nie, Z. J. Xu, Q. Zhang, *ACS Appl. Mater. Interfaces* **2016**, *8*, 7464.

[45] Y. Yang, G. Yu, J. J. Cha, H. Wu, M. Vosgueritchian, Y. Yao, Z. Bao, Y. Cui, *ACS Nano* **2011**, *5*, 9187.

[46] H. Zhao, Y. Wei, R. Qiao, C. Zhu, Z. Zheng, M. Ling, Z. Jia, Y. Bai, Y. Fu, J. Lei, X. Song, V. S. Battaglia, W. Yang, P. B. Messersmith, G. Liu, *Nano Lett.* **2015**, *15*, 7927.

[47] Y. Zhong, X. Xu, Y. Liu, W. Wang, Z. Shao, *Polyhedron* **2018**, *155*, 464.

[48] Z. Jin, K. Xie, X. Hong, Z. Hu, X. Liu, *J. Power Sources* **2012**, *218*, 163.

[49] M. J. Lacey, F. Jeschull, K. Edström, D. Brandell, *Chem. Commun.* **2013**, *49*, 8531.

[50] M. Kim, S.-H. Kang, J. Manuel, X. Zhao, K. K. Cho, J. H. Ahn, *Mater. Res. Bull.* **2015**, *69*, 29.

[51] G. Ai, Y. Dai, Y. Ye, W. Mao, Z. Wang, H. Zhao, Y. Chen, J. Zhu, Y. Fu, V. Battaglia, J. Guo, V. Srinivasan, G. Liu, *Nano Energy* **2015**, *16*, 28.

[52] P. Bhattacharya, M. I. Nandasiri, D. Lv, A. M. Schwarz, J. T. Darsell, W. A. Henderson, D. A. Tomalia, J. Liu, J.-G. Zhang, J. Xiao, *Nano Energy* **2016**, *19*, 176.

[53] L. Fan, H. L. Zhuang, K. Zhang, V. R. Cooper, Q. Li, Y. Lu, *Adv. Sci.* **2016**, *3*, 1600175.

[54] Q. Zhang, Y. Wang, Z. W. Seh, Z. Fu, R. Zhang, Y. Cui, *Nano Lett.* **2015**, *15*, 3780.

[55] C. J. Hart, M. Cuisinier, X. Liang, D. Kundu, A. Garsuch, L. F. Nazar, *Chem. Commun.* **2015**, *51*, 2308.

[56] Q. Pang, X. Liang, C. Y. Kwok, L. F. Nazar, *Nat. Energy* **2016**, *1*, 1.

[57] H. Yao, K. Yan, W. Li, G. Zheng, D. Kong, Z. W. Seh, V. K. Narasimhan, Z. Liang, Y. Cui, *Energy Environ. Sci.* **2014**, *7*, 3381.

[58] M. Ling, L. Zhang, T. Zheng, J. Feng, J. Guo, L. Mai, G. Liu, *Nano Energy* **2017**, *38*, 82.

[59] W. Hua, Z. Yang, H. Nie, Z. Li, J. Yang, Z. Guo, C. Ruan, X. Chen, S. Huang, *ACS Nano* **2017**, *11*, 2209.

[60] Y. Li, I. A. Murphy, Y. Chen, F. Lin, X. Wang, S. Wang, D. Hubble, S. H. Jang, K. T. Muller, C. Wang, A. K. Y. Jen, J. Yang, *J. Mater. Chem. A* **2019**, *7*, 13372.

[61] X. Liang, C. Hart, Q. Pang, A. Garsuch, T. Weiss, L. F. Nazar, *Nat. Commun.* **2015**, *6*, 1.

[62] X. Yao, N. Huang, F. Han, Q. Zhang, H. Wan, J. P. Mwizerwa, C. Wang, X. Xu, *Adv. Energy Mater.* **2017**, *7*, 1602923.

[63] G. G. Eshetu, X. Judez, C. Li, M. Martinez-Ibañez, I. Gracia, O. Bondarchuk, J. Carrasco, L. M. Rodriguez-Martinez, H. Zhang, M. Armand, *J. Am. Chem. Soc.* **2018**, *140*, 9921.

[64] S. Das, P. Ngene, P. Norby, T. Vegge, P. E. de Jongh, D. Blanchard, *J. Electrochem. Soc.* **2016**, *163*, A2029.

[65] E. Umeshbabu, B. Zheng, Y. Yang, *Recent Progress in All-Solid-State Lithium−Sulfur Batteries Using High Li-Ion Conductive Solid Electrolytes*, Springer Singapore, **2019**.

[66] J. Janek, W. G. Zeier, *Nat. Energy* **2016**, *1*, 16141.

[67] A. C. Luntz, J. Voss, K. Reuter, *J. Phys. Chem. Lett.* **2015**, *6*, 4599.

[68] T. Kobayashi, Y. Imade, D. Shishihara, K. Homma, M. Nagao, R. Watanabe, T. Yokoi, A. Yamada, R. Kanno, T. Tatsumi, *J. Power Sources* **2008**, *182*, 621.

[69] M. Nagao, A. Hayashi, M. Tatsumisago, *Energy Technol.* **2013**, *1*, 186.

[70] F. Y. Fan, M. S. Pan, K. C. Lau, R. S. Assary, W. H. Woodford, L. A. Curtiss, W. C. Carter, Y.-M. Chiang, *J. Electrochem. Soc.* **2016**, *163*, A3111.

[71] Q. Zou, Y. C. Lu, *J. Phys. Chem. Lett.* **2016**, *7*, 1518.

[72] Q. He, Y. Gorlin, M. U. M. Patel, H. A. Gasteiger, Y. C. Lu, *J. Electrochem. Soc.* **2018**, *165*, A4027.

[73] Q. Pang, C. Y. Kwok, D. Kundu, X. Liang, L. F. Nazar, *Joule* **2019**, *3*, 136.

[74] P. D. Frischmann, L. C. H. Gerber, S. E. Doris, E. Y. Tsai, F. Y. Fan, X. Qu, A. Jain, K. A. Persson, Y. M. Chiang, B. A. Helms, *Chem. Mater.* **2015**, *27*, 6765.

[75] L. C. H. Gerber, P. D. Frischmann, F. Y. Fan, S. E. Doris, X. Qu, A. M. Scheuermann, K. Persson, Y. M. Chiang, B. A. Helms, *Nano Lett.* **2016**, *16*, 549.

[76] S. S. Zhang, *J. Power Sources* **2016**, *322*, 99.

[77] Z. W. Seh, H. Wang, P.-C. Hsu, Q. Zhang, W. Li, G. Zheng, H. Yao, Y. Cui, *Energy Environ. Sci.* **2014**, *7*, 672.

[78] Z. Wang, Y. Chen, V. Battaglia, G. Liu, *J. Mater. Res.* **2014**, *29*, 1027.

[79] D.-J. Lee, M. Agostini, J.-W. Park, Y.-K. Sun, J. Hassoun, B. Scrosati, *ChemSusChem* **2013**, *6*, 2245.

[80] J. H. Kim, T. Kim, Y. C. Jeong, K. Lee, K. T. Park, S. J. Yang, C. R. Park, *Adv. Energy Mater.* **2015**, *5*, 1.

[81] Q. Zou, Z. Liang, G. Y. Du, C. Y. Liu, E. Y. Li, Y. C. Lu, *J. Am. Chem. Soc.* **2018**, *140*, 10740.

[82] H. Pan, K. S. Han, M. Vijayakumar, J. Xiao, R. Cao, J. Chen, J. Zhang, K. T. Mueller, Y. Shao, J. Liu, *ACS Appl. Mater. Interfaces* **2017**, *9*, 4290.

[83] M.-K. Song, Y. Zhang, E. J. Cairns, *AIChE J.* **2015**, *61*, 2749.

[84] G. Li, J. Sun, W. Hou, S. Jiang, Y. Huang, J. Geng, *Nat. Commun.* **2016**, *7*, 10601.

[85] H. Yuan, J.-Q. Huang, H.-J. Peng, M.-M. Titirici, R. Xiang, R. Chen, Q. Liu, Q. Zhang, *Adv. Energy Mater.* **2018**, *8*, 1802107.

[86] Y. Chu, X. Cui, Q. Pan, *ACS Appl. Energy Mater.* **2018**, *1*, 6919.

[87] M. Hagen, D. Hanselmann, K. Ahlbrecht, R. Maça, D. Gerber, J. Tübke, *Adv. Energy Mater.* **2015**, *5*, 1401986.

[88] D. Eroglu, K. R. Zavadil, K. G. Gallagher, *J. Electrochem. Soc.* **2015**, *162*, A982.

[89] T. Cleaver, P. Kovacik, M. Marinescu, T. Zhang, G. Offer, *J. Electrochem. Soc.* **2018**, *165*, A6029.

[90] T. Zhang, M. Marinescu, S. Walus, P. Kovacik, G. J. Offer, *J. Electrochem. Soc.* **2018**, *165*, A6001.

[91] W. J. Chung, J. J. Griebel, E. T. Kim, H. Yoon, A. G. Simmonds, H. J. Ji, P. T. Dirlam, R. S. Glass, J. J. Wie, N. A. Nguyen, B. W. Guralnick, J. Park, Á. Somogyi, P. Theato, M. E. Mackay, Y. E. Sung, K. Char, J. Pyun, *Nat. Chem.* **2013**, *5*, 518.

[92] H. Kim, J. Lee, H. Ahn, O. Kim, M. J. Park, *Nat. Commun.* **2015**, *6*, 1.

[93] H. Chen, C. Wang, C. Hu, J. Zhang, S. Gao, W. Lu, L. Chen, *J. Mater. Chem. A* **2015**, *3*, 1392.

[94] Y. Liang, Z. Tao, J. Chen, *Adv. Energy Mater.* **2012**, *2*, 742.

[95] S. Xin, L. Gu, N. H. Zhao, Y. X. Yin, L. J. Zhou, Y. G. Guo, L. J. Wan, *J. Am. Chem. Soc.* **2012**, *134*, 18510.

[96] Z. Li, L. Yuan, Z. Yi, Y. Sun, Y. Liu, Y. Jiang, Y. Shen, Y. Xin, Z. Zhang, Y. Huang, *Adv. Energy Mater.* **2014**, *4*, 1301473.

[97] Y. Yang, G. Zheng, Y. Cui, *Energy Environ. Sci.* **2013**, *6*, 1552.

[98] D.-H. Lim, M. Agostini, F. Nitze, J. Manuel, J.-H. Ahn, A. Matic, *Sci. Rep.* **2017**, *7*, 6327.

[99] S. Zhang, W. Guo, F. Yang, P. Zheng, R. Qiao, Z. Li, *Batter. Supercaps* **2019**, *2*, 627.

[100] A. Eftekhari, *Sustain. Energy Fuels* **2017**, *1*, 14.

[101] A. Abouimrane, D. Dambournet, K. W. Chapman, P. J. Chupas, W. Weng, K. Amine, *J. Am. Chem. Soc.* **2012**, *134*, 4505.

[102] X. Li, J. Liang, K. Zhang, Z. Hou, W. Zhang, Y. Zhu, Y. Qian, *Energy Environ. Sci.* **2015**, *8*, 3181.

[103] X. B. Cheng, R. Zhang, C. Z. Zhao, F. Wei, J. G. Zhang, Q. Zhang, *Adv. Sci.* **2015**, *3*, 1.

[104] D. Lin, Y. Liu, Y. Cui, *Nat. Nanotechnol.* **2017**, *12*, 194.

[105] C. Monroe, J. Newman, *J. Electrochem. Soc.* **2005**, *152*, A396.

[106] Q. Wang, J. Jin, X. Wu, G. Ma, J. Yang, Z. Wen, *Phys. Chem. Chem. Phys.* **2014**, *16*, 21225.

[107] X. Yu, Z. Bi, F. Zhao, A. Manthiram, *ACS Appl. Mater. Interfaces* **2015**, *7*, 16625.

[108] S. Gu, X. Huang, Q. Wang, J. Jin, Q. Wang, Z. Wen, R. Qian, *J. Mater. Chem. A* **2017**, *5*, 13971.

[109] T. Abe, F. Sagane, M. Ohtsuka, Y. Iriyama, Z. Ogumi, *J. Electrochem. Soc.* **2005**, *152*, A2151.

[110] T. Swamy, R. Park, B. W. Sheldon, D. Rettenwander, L. Porz, S. Berendts, R. Uecker, W. C. Carter, Y.-M. Chiang, *J. Electrochem. Soc.* **2018**, *165*, A3648.

[111] P. Barai, K. Higa, V. Srinivasan, *Phys. Chem. Chem. Phys.* **2017**, *19*, 20493.

[112] K. M. Abraham, Z. Jiang, B. Carroll, *Chem. Mater.* **1997**, *9*, 1978.

[113] I. Gurevitch, R. Buonsanti, A. A. Teran, B. Gludovatz, R. O. Ritchie, J. Cabana, N. P. Balsara, *J. Electrochem. Soc.* **2013**, *160*, A1611.

[114] R. Khurana, J. L. Schaefer, L. A. Archer, G. W. Coates, *J. Am. Chem. Soc.* **2014**, *136*, 7395.

[115] R. He, T. Kyu, *Macromolecules* **2016**, *49*, 5637.

[116] D. G. Mackanic, W. Michaels, M. Lee, D. Feng, J. Lopez, J. Qin, Y. Cui, Z. Bao, *Adv. Energy Mater.* **2018**, *8*, 1800703.

[117] L. Liu, Y. X. Yin, J. Y. Li, S. H. Wang, Y. G. Guo, L. J. Wan, *Adv. Mater.* **2018**, *30*, 1.

[118] Z. Liang, D. Lin, J. Zhao, Z. Lu, Y. Liu, C. Liu, Y. Lu, H. Wang, K. Yan, X. Tao, Y. Cui, *Proc. Natl. Acad. Sci.* **2016**, *113*, 2862.

[119] D. Lin, J. Zhao, J. Sun, H. Yao, Y. Liu, K. Yan, Y. Cui, *Proc. Natl. Acad. Sci.* **2017**, *114*, 4613.

[120] S. Li, H. Wang, J. Cuthbert, T. Liu, J. F. Whitacre, K. Matyjaszewski, *Joule* **2019**, *3*, 1637.

[121] F. Ding, W. Xu, G. L. Graff, J. Zhang, M. L. Sushko, X. Chen, Y. Shao, M. H. Engelhard, Z. Nie, J. Xiao, X. Liu, P. V. Sushko, J. Liu, J. G. Zhang, *J. Am. Chem. Soc.* **2013**, *135*, 4450.

[122] Y. Lu, Z. Tu, L. A. Archer, *Nat. Mater.* **2014**, *13*, 961.

[123] Y. Lu, S. K. Das, S. S. Moganty, L. A. Archer, *Adv. Mater.* **2012**, *24*, 4430.

[124] Y. Lu, K. Korf, Y. Kambe, Z. Tu, L. A. Archer, *Angew. Chemie - Int. Ed.* **2014**, *53*, 488.

[125] S. Choudhury, R. Mangal, A. Agrawal, L. A. Archer, *Nat. Commun.* **2015**, *6*, 1.

[126] Y. Lu, M. Tikekar, R. Mohanty, K. Hendrickson, L. Ma, L. A. Archer, *Adv. Energy Mater.* **2015**, *5*, 1402073.

[127] J. Song, H. Lee, M.-J. Choo, J.-K. Park, H.-T. Kim, *Sci. Rep.* **2015**, *5*, 14458.

[128] Y. Yamada, A. Yamada, *J. Electrochem. Soc.* **2015**, *162*, A2406.

[129] K. M. Diederichsen, E. J. McShane, B. D. McCloskey, *ACS Energy Lett.* **2017**, *2*, 2563.

[130] S. Zhang, N. Sun, X. He, X. Lu, X. Zhang, *J. Phys. Chem. Ref. Data* **2006**, *35*, 1475.

[131] P. C. Howlett, D. R. MacFarlane, A. F. Hollenkamp, *Electrochem. Solid-State Lett.* **2004**, *7*, A97.

[132] P. C. Howlett, N. Brack, A. F. Hollenkamp, M. Forsyth, D. R. MacFarlane, *J. Electrochem. Soc.* **2006**, *153*, A595.

[133] S. Ferrari, E. Quartarone, P. Mustarelli, A. Magistris, S. Protti, S. Lazzaroni, M. Fagnoni, A.

Albini, *J. Power Sources* **2009**, *194*, 45.

[134] A. I. Bhatt, A. S. Best, J. Huang, A. F. Hollenkamp, *J. Electrochem. Soc.* **2010**, *157*, A66.

[135] H. Yoon, P. C. Howlett, A. S. Best, M. Forsyth, D. R. MacFarlane, *J. Electrochem. Soc.* **2013**, *160*, A1629.

[136] L. Grande, J. Von Zamory, S. L. Koch, J. Kalhoff, E. Paillard, S. Passerini, *ACS Appl. Mater. Interfaces* **2015**, *7*, 5950.

[137] M. Montanino, M. Moreno, M. Carewska, G. Maresca, E. Simonetti, R. Lo Presti, F. Alessandrini, G. B. Appetecchi, *J. Power Sources* **2014**, *269*, 608.

[138] Y. An, P. Zuo, X. Cheng, L. Liao, G. Yin, *Electrochim. Acta* **2011**, *56*, 4841.

[139] J. Yuan, D. Mecerreyes, M. Antonietti, *Prog. Polym. Sci.* **2013**, *38*, 1009.

[140] T. M. Pappenfus, W. A. Henderson, B. B. Owens, K. R. Mann, W. H. Smyrl, *J. Electrochem. Soc.* **2004**, *151*, A209.

[141] G. B. Appetecchi, G. T. Kim, M. Montanino, M. Carewska, R. Marcilla, D. Mecerreyes, I. De Meatza, *J. Power Sources* **2010**, *195*, 3668.

[142] C. Gerbaldi, J. R. Nair, S. Ferrari, A. Chiappone, G. Meligrana, S. Zanarini, P. Mustarelli, N. Penazzi, R. Bongiovanni, *J. Memb. Sci.* **2013**, *436*, 232.

[143] A. S. Shaplov, D. O. Ponkratov, P. S. Vlasov, E. I. Lozinskaya, L. V. Gumileva, C. Surcin, M. Morcrette, M. Armand, P.-H. Aubert, F. Vidal, Y. S. Vygodskii, *J. Mater. Chem. A* **2015**, *3*, 2188.

[144] J. Fu, Q. Lu, D. Shang, L. Chen, Y. Jiang, Y. Xu, J. Yin, X. Dong, W. Deng, S. Yuan, *J. Mater. Sci.* **2018**, *53*, 8420.

[145] T. Frömling, M. Kunze, M. Schönhoff, J. Sundermeyer, B. Roling, *J. Phys. Chem. B* **2008**, *112*, 12985.

[146] H. F. Xiang, B. Yin, H. Wang, H. W. Lin, X. W. Ge, S. Xie, C. H. Chen, *Electrochim. Acta* **2010**, *55*, 5204.

[147] K. Yoshida, M. Tsuchiya, N. Tachikawa, K. Dokko, M. Watanabe, *J. Electrochem. Soc.* **2012**, *159*, A1005.

[148] H. Shobukawa, H. Tokuda, M. A. B. H. Susan, M. Watanabe, *Electrochim. Acta* **2005**, *50*, 3872.

[149] Y. Yang, J. Xiong, S. Lai, R. Zhou, M. Zhao, H. Geng, Y. Zhang, Y. Fang, C. Li, J. Zhao, *ACS Appl. Mater. Interfaces* **2019**, *11*, 6118.

[150] Z. L. Brown, S. Jurng, C. C. Nguyen, B. L. Lucht, *ACS Appl. Energy Mater.* **2018**, *1*, 3057.

[151] J. Yu, N. Gao, J. Peng, N. Ma, X. Liu, C. Shen, K. Xie, Z. Fang, *Front. Chem.* **2019**, *7*, 494.

[152] J. Wang, F. Lin, H. Jia, J. Yang, C. W. Monroe, Y. Nuli, *Angew. Chemie - Int. Ed.* **2014**, *53*, 10099.

[153] Q. Ma, B. Tong, Z. Fang, X. Qi, W. Feng, J. Nie, Y.-S. Hu, H. Li, X. Huang, L. Chen, Z. Zhou, *J. Electrochem. Soc.* **2016**, *163*, A1776.

[154] J. Ko, Y. S. Yoon, *Ceram. Int.* **2019**, *45*, 30.

[155] C. Wang, Y. S. Meng, K. Xu, *J. Electrochem. Soc.* **2019**, *166*, A5184.

[156] J. W. Park, K. Ueno, N. Tachikawa, K. Dokko, M. Watanabe, *J. Phys. Chem. C* **2013**, *117*, 20531.

[157] G. Salitra, E. Markevich, A. Rosenman, Y. Talyosef, D. Aurbach, A. Garsuch, *ChemElectroChem*

2014, *1*, 1492.

[158] H. Kim, F. Wu, J. T. Lee, N. Nitta, H. T. Lin, M. Oschatz, W. Il Cho, S. Kaskel, O. Borodin, G. Yushin, *Adv. Energy Mater.* **2015**, *5*, 1.

[159] Z. Lin, Z. Liu, W. Fu, N. J. Dudney, C. Liang, *Adv. Funct. Mater.* **2013**, *23*, 1064.

[160] Q. Pang, X. Liang, A. Shyamsunder, L. F. Nazar, *Joule* **2017**, *1*, 871.

[161] Y. V. Mikhaylik, *Electrolytes for Lithium Sulfur Cells*, **2008**, US7354680.

[162] J. Scheers, S. Fantini, P. Johansson, *J. Power Sources* **2014**, *255*, 204.

[163] S. S. Zhang, *Electrochim. Acta* **2012**, *70*, 344.

[164] S. Xiong, K. Xie, Y. Diao, X. Hong, *J. Power Sources* **2013**, *236*, 181.

[165] S. Xiong, K. Xie, Y. Diao, X. Hong, *J. Power Sources* **2014**, *246*, 840.

[166] A. Jozwiuk, B. B. Berkes, T. Weiß, H. Sommer, J. Janek, T. Brezesinski, *Energy Environ. Sci.* **2016**, *9*, 2603.

[167] N. Azimi, Z. Xue, I. Bloom, M. L. Gordin, D. Wang, T. Daniel, C. Takoudis, Z. Zhang, *ACS Appl. Mater. Interfaces* **2015**, *7*, 9169.

[168] C. Zu, N. Azimi, Z. Zhang, A. Manthiram, *J. Mater. Chem. A* **2015**, *3*, 14864.

[169] Y. B. Yang, Y. X. Liu, Z. Song, Y. H. Zhou, H. Zhan, *ACS Appl. Mater. Interfaces* **2017**, *9*, 38950.

[170] G. Li, Y. Gao, X. He, Q. Huang, S. Chen, S. H. Kim, D. Wang, *Nat. Commun.* **2017**, *8*, 850.

[171] Y. Yan, Y.-X. Yin, S. Xin, J. Su, Y.-G. Guo, L.-J. Wan, *Electrochim. Acta* **2013**, *91*, 58.

[172] Y. Yang, M. T. McDowell, A. Jackson, J. J. Cha, S. S. Hong, Y. Cui, *Nano Lett.* **2010**, *10*, 1486.

[173] B. Li, S. Li, J. Xu, S. Yang, *Energy Environ. Sci.* **2016**, *9*, 2025.

[174] Y. Shen, J. Zhang, Y. Pu, H. Wang, B. Wang, J. Qian, Y. Cao, F. Zhong, X. Ai, H. Yang, *ACS Energy Lett.* **2019**, *4*, 1717.

[175] J.-W. Park, K. Yamauchi, E. Takashima, N. Tachikawa, K. Ueno, K. Dokko, M. Watanabe, *J. Phys. Chem. C* **2013**, *117*, 4431.

[176] J. N. Israelachvili, *Intermolecular and Surface Forces*, Academic Press, Waltham, MA, **2011**.

[177] W. A. Henderson, M. Herstedt, V. G. Young, S. Passerini, H. C. De Long, P. C. Trulove, *Inorg. Chem.* **2006**, *45*, 1412.

[178] T. A. Pascal, K. H. Wujcik, J. Velasco-Velez, C. Wu, A. A. Teran, M. Kapilashrami, J. Cabana, J. Guo, M. Salmeron, N. Balsara, D. Prendergast, *J. Phys. Chem. Lett.* **2014**, *5*, 1547.

[179] T. A. Pascal, K. H. Wujcik, D. R. Wang, N. P. Balsara, D. Prendergast, *Phys. Chem. Chem. Phys.* **2017**, *19*, 1441.

[180] H. Tokuda, S. Tsuzuki, M. A. B. H. Susan, K. Hayamizu, M. Watanabe, *J. Phys. Chem. B* **2006**, *110*, 19593.

[181] A. Andriola, K. Singh, J. Lewis, L. Yu, *J. Phys. Chem. B* **2010**, *114*, 11709.

[182] M. Schmeisser, P. Illner, R. Puchta, A. Zahl, R. Van Eldik, *Chem. - A Eur. J.* **2012**, *18*, 10969.

[183] W. R. Fawcett, *J. Phys. Chem.* **1993**, *97*, 9540.

[184] M. J. Muldoon, C. M. Gordon, I. R. Dunkin, *J. Chem. Soc. Perkin Trans. 2* **2001**, 433.

[185] L. Suo, Y.-S. Hu, H. Li, M. Armand, L. Chen, *Nat. Commun.* **2013**, *4*, 1481.

[186] Y. Yamada, K. Furukawa, K. Sodeyama, K. Kikuchi, M. Yaegashi, Y. Tateyama, A. Yamada, *J. Am. Chem. Soc.* **2014**, *136*, 5039.

[187] X. Ren, S. Chen, H. Lee, D. Mei, M. H. Engelhard, S. D. Burton, W. Zhao, J. Zheng, Q. Li, M. S. Ding, M. Schroeder, J. Alvarado, K. Xu, Y. S. Meng, J. Liu, J.-G. Zhang, W. Xu, *Chem* **2018**, *4*, 1877.

[188] K. A. See, H. L. Wu, K. C. Lau, M. Shin, L. Cheng, M. Balasubramanian, K. G. Gallagher, L. A. Curtiss, A. A. Gewirth, *ACS Appl. Mater. Interfaces* **2016**, *8*, 34360.

[189] M. Cuisinier, P. E. Cabelguen, B. D. Adams, A. Garsuch, M. Balasubramanian, L. F. Nazar, *Energy Environ. Sci.* **2014**, *7*, 2697.

[190] C. W. Lee, Q. Pang, S. Ha, L. Cheng, S. D. Han, K. R. Zavadil, K. G. Gallagher, L. F. Nazar, M. Balasubramanian, *ACS Cent. Sci.* **2017**, *3*, 605.

[191] *,† Wesley A. Henderson, ‡ Neil R. Brooks, ‡ and William W. Brennessel, J. . Victor G. Young, **2003**, DOI 10.1021/CM034351Z.

[192] W. A. Henderson, N. R. Brooks, V. G. Young, *Chem. Mater.* **2003**, *15*, 4685.

[193] W. A. Henderson, *J. Phys. Chem. B* **2006**, *110*, 13177.

[194] T. Tamura, K. Yoshida, T. Hachida, M. Tsuchiya, M. Nakamura, Y. Kazue, N. Tachikawa, K. Dokko, M. Watanabe, *Chem. Lett.* **2010**, *39*, 753.

[195] C. Austen Angell, Y. Ansari, Z. Zhao, *Faraday Discuss.* **2012**, *154*, 9.

[196] K. Ueno, K. Yoshida, M. Tsuchiya, N. Tachikawa, K. Dokko, M. Watanabe, *J. Phys. Chem. B* **2012**, *116*, 11323.

[197] K. Yoshida, M. Nakamura, Y. Kazue, N. Tachikawa, S. Tsuzuki, S. Seki, K. Dokko, M. Watanabe, *J. Am. Chem. Soc.* **2011**, *133*, 13121.

[198] K. Yoshida, M. Tsuchiya, N. Tachikawa, K. Dokko, M. Watanabe, *J. Phys. Chem. C* **2011**, *115*, 18384.

[199] C. Zhang, K. Ueno, A. Yamazaki, K. Yoshida, H. Moon, T. Mandai, Y. Umebayashi, K. Dokko, M. Watanabe, *J. Phys. Chem. B* **2014**, *118*, 5144.

[200] K. Ueno, R. Tatara, S. Tsuzuki, S. Saito, H. Doi, K. Yoshida, T. Mandai, M. Matsugami, Y. Umebayashi, K. Dokko, M. Watanabe, *Phys. Chem. Chem. Phys.* **2015**, *17*, 8248.

[201] W. Shinoda, Y. Hatanaka, M. Hirakawa, S. Okazaki, S. Tsuzuki, K. Ueno, M. Watanabe, *J. Chem. Phys.* **2018**, *148*, 193809.

[202] Z. Yu, C. Fang, J. Huang, B. G. Sumpter, R. Qiao, *ACS Appl. Mater. Interfaces* **2018**, *10*, 32151.

[203] D. R. MacFarlane, M. Forsyth, E. I. Izgorodina, A. P. Abbott, G. Annat, K. Fraser, *Phys. Chem. Chem. Phys.* **2009**, *11*, 4962.

[204] H. Tokuda, S.-J. Baek, M. Watanabe, *Electrochemistry* **2005**, *73*, 620.

[205] P. Jankowski, M. Dranka, W. Wieczorek, P. Johansson, *J. Phys. Chem. Lett.* **2017**, *8*, 3678.

[206] T. Mandai, K. Yoshida, S. Tsuzuki, R. Nozawa, H. Masu, K. Ueno, K. Dokko, M. Watanabe, *J. Phys. Chem. B* **2015**, *119*, 1523.

[207] T. Mandai, P. Johansson, *J. Phys. Chem. C* **2016**, *120*, 21285.

[208] L. D. Reed, A. Arteaga, E. J. Menke, *J. Phys. Chem. B* **2015**, *119*, 12677.

[209] C. Zhang, A. Yamazaki, J. Murai, J. W. Park, T. Mandai, K. Ueno, K. Dokko, M. Watanabe, *J. Phys. Chem. C* **2014**, *118*, 17362.

[210] T. Tamura, T. Hachida, K. Yoshida, N. Tachikawa, K. Dokko, *J. Power Sources* **2010**, *195*, 6095.

[211] H. Moon, R. Tatara, T. Mandai, K. Ueno, K. Yoshida, N. Tachikawa, T. Yasuda, K. Dokko, M. Watanabe, *J. Phys. Chem. C* **2014**, *118*, 20246.

[212] H. Wang, M. Matsui, H. Kuwata, H. Sonoki, Y. Matsuda, X. Shang, Y. Takeda, O. Yamamoto, N. Imanishi, *Nat. Commun.* **2017**, *8*, 15106.

[213] D. Y. Oh, Y. J. Nam, K. H. Park, S. H. Jung, S. J. Cho, Y. K. Kim, Y. G. Lee, S. Y. Lee, Y. S. Jung, *Adv. Energy Mater.* **2015**, *5*, 1.

[214] K. Dokko, N. Tachikawa, K. Yamauchi, M. Tsuchiya, A. Yamazaki, E. Takashima, J.-W. Park, K. Ueno, S. Seki, N. Serizawa, M. Watanabe, *J. Electrochem. Soc.* **2013**, *160*, A1304.

[215] H. Lu, Y. Yuan, Z. Hou, Y. Lai, K. Zhang, Y. Liu, *RSC Adv.* **2016**, *6*, 18186.

[216] K. Ueno, J. Park, A. Yamazaki, T. Mandai, N. Tachikawa, K. Dokko, M. Watanabe, *J. Phys. Chem. C* **2013**, *117*, 20509.

[217] S. Zhang, A. Ikoma, Z. Li, K. Ueno, X. Ma, K. Dokko, M. Watanabe, *ACS Appl. Mater. Interfaces* **2016**, *8*, 27803.

[218] D. Hubble, J. Qin, F. Lin, I. A. Murphy, S. H. Jang, J. Yang, A. K. Y. Jen, *J. Mater. Chem. A* **2018**, *6*, 24100.

[219] F. Wohde, M. Balabajew, B. Roling, *J. Electrochem. Soc.* **2016**, *163*, A714.

[220] K. Ueno, J. Murai, K. Ikeda, S. Tsuzuki, M. Tsuchiya, R. Tatara, T. Mandai, Y. Umebayashi, K. Dokko, M. Watanabe, *J. Phys. Chem. C* **2016**, *120*, 15792.

[221] T. Matsuda, Y. Mishima, S. Azizian, H. Matsubara, T. Takiue, M. Aratono, *Colloid Polym. Sci.* **2007**, *285*, 1601.

[222] M. Kirchhöfer, J. von Zamory, E. Paillard, S. Passerini, *Int. J. Mol. Sci.* **2014**, *15*, 14868.

[223] Y. Kitazawa, K. Iwata, S. Imaizumi, H. Ahn, S. Y. Kim, K. Ueno, M. J. Park, M. Watanabe, *Macromolecules* **2014**, *47*, 6009.

[224] Y. Kitazawa, K. Iwata, R. Kido, S. Imaizumi, S. Tsuzuki, W. Shinoda, K. Ueno, T. Mandai, H. Kokubo, K. Dokko, M. Watanabe, *Chem. Mater.* **2018**, *30*, 252.

[225] A. J. D'Angelo, M. J. Panzer, *J. Phys. Chem. B* **2017**, *121*, 890.

[226] R. Kido, K. Ueno, K. Iwata, Y. Kitazawa, S. Imaizumi, T. Mandai, K. Dokko, M. Watanabe, *Electrochim. Acta* **2015**, *175*, 5.

[227] J. Evans, C. A. Vincent, P. G. Bruce, *Polymer (Guildf).* **1987**, *28*, 2324.

[228] B. L. Papke, M. A. Ratner, D. F. Shriver, *J. Electrochem. Soc.* **1982**, *129*, 1434.

[229] F. E. Malherbe, H. J. Bernstein, *J. Am. Chem. Soc.* **1952**, *74*, 4408.

[230] M. D. Tikekar, S. Choudhury, Z. Tu, L. A. Archer, *Nat. Energy* **2016**, *1*, 1.

[231] P.-G. de Gennes, *Scaling Concepts in Polymer Physics*, Cornell University Press, Ithaca, NY, **1979**.

[232] M. Zrinyi, F. Horkay, *Polymer (Guildf).* **1987**, *28*, 1139.

[233] Y. Huang, I. Szleifer, N. A. Peppas, *Macromolecules* **2002**, *35*, 1373.

[234] J. E. Mark, Ed. , *Polymer Data Handbook*, Oxford University Press, New York, NY, **1999**.

[235] Z. Chen, P. A. Fitzgerald, G. G. Warr, R. Atkin, *Phys. Chem. Chem. Phys.* **2015**, *17*, 14872.

[236] M. Rubinstein, R. H. Colby, A. V. Dobrynin, J. F. Joanny, *Macromolecules* **1996**, *29*, 398.

[237] Y. Ding, J. Zhang, L. Chang, X. Zhang, H. Liu, L. Jiang, *Adv. Mater.* **2017**, *29*, 1704253.

[238] "Poly(ethylene glycol)," can be found under http://polymerdatabase.com/polymers/polyethyleneglycol.html, **2015**.

[239] X. Zhao, *Proc. Natl. Acad. Sci.* **2017**, *114*, 8138.

[240] A. E. Likhtman, M. Ponmurugan, *Macromolecules* **2014**, *47*, 1470.

[241] M. Chintapalli, K. Timachova, K. R. Olson, S. J. Mecham, D. Devaux, J. M. Desimone, N. P. Balsara, *Macromolecules* **2016**, *49*, 3508.

[242] A. S. Shaplov, D. O. Ponkratov, P.-H. Aubert, E. I. Lozinskaya, C. Plesse, A. Maziz, P. S. Vlasov, F. Vidal, Y. S. Vygodskii, *Polymer (Guildf).* **2014**, *55*, 3385.

[243] A. A. Teran, M. H. Tang, S. A. Mullin, N. P. Balsara, *Solid State Ionics* **2011**, *203*, 18.

[244] R. D. Hancock, *J. Chem. Educ.* **1992**, *69*, 615.

[245] P. Flodin, P. Lagerkvist, *J. Chromatogr. A* **1981**, *215*, 7.

[246] W. Li, Z. Zhang, B. Han, S. Hu, Y. Xie, G. Yang, *J. Phys. Chem. B* **2007**, *111*, 6452.

[247] P. M. Bayley, G. H. Lane, N. M. Rocher, B. R. Clare, A. S. Best, D. R. MacFarlane, M. Forsyth, *Phys. Chem. Chem. Phys.* **2009**, *11*, 7202.

[248] D. Bamford, A. Reiche, G. Dlubek, F. Alloin, J. Y. Sanchez, M. A. Alam, *J. Chem. Phys.* **2003**, *118*, 9420.

[249] K. N. Wood, E. Kazyak, A. F. Chadwick, K. H. Chen, J. G. Zhang, K. Thornton, N. P. Dasgupta, *ACS Cent. Sci.* **2016**, *2*, 790.

[250] B. Tjaden, S. J. Cooper, D. J. Brett, D. Kramer, P. R. Shearing, *Curr. Opin. Chem. Eng.* **2016**, *12*, 44.

[251] S. Gupta, Physico-Chemical Properties of Polypropylene Glycols, University of Greenwich, **2015**.

[252] A. A. Chuiko, V. S. Sperkach, V. M. Ogenko, T. P. Tantsyura, L. N. Ganyuk, L. V. Dubrovina, A. L. Stribulevich, *Polym. Sci. U.S.S.R.* **1991**, *33*, 1061.

[253] I. Bahar, B. Erman, L. Monnerie, *Macromolecules* **1989**, *22*, 2396.

[254] C. Wu, W. F. Koch, K. W. Pratt, *J. Res. Natl. Inst. Stand. Technol.* **1991**, *96*, 191.

[255] S. V Mentus, *Zeitschrift für Naturforsch. A* **1982**, *38*, 252.

[256] M. M. Doeff, *J. Electrochem. Soc.* **1999**, *146*, 2024.

[257] S. Tsuzuki, W. Shinoda, M. Matsugami, Y. Umebayashi, K. Ueno, T. Mandai, S. Seki, K. Dokko, M. Watanabe, *Phys. Chem. Chem. Phys.* **2015**, *17*, 126.

[258] R. J. Sengwa, *Polym. Int.* **2004**, *53*, 744.

[259] R. Sengwa, K. Kaur, R. Chaudhary, *Polym. Int.* **2000**, *49*, 599.

[260] S. B. Aziz, T. J. Woo, M. F. Z. Kadir, H. M. Ahmed, *J. Sci. Adv. Mater. Devices* **2018**, *3*, 1.

[261] J. Vila, P. Ginés, J. M. Pico, C. Franjo, E. Jiménez, L. M. Varela, O. Cabeza, *Fluid Phase Equilib.* **2006**, *242*, 141.

[262] P. Pal, A. Ghosh, *J. Appl. Phys.* **2019**, *126*, 135102.

[263] K. M. Diederichsen, H. G. Buss, B. D. McCloskey, *Macromolecules* **2017**, *50*, 3831.

[264] K. B. Oldham, J. C. Myland, *Fundamentals of Electrochemical Science*, Academic Press, San Diego, CA, **1994**.

[265] A. Shyamsunder, W. Beichel, P. Klose, Q. Pang, H. Scherer, A. Hoffmann, G. K. Murphy, I. Krossing, L. F. Nazar, *Angew. Chemie Int. Ed.* **2017**, *56*, 6192.

[266] M. Helen, M. Fichtner, M. A. Reddy, **2019**, *1900183*, 1.

[267] B. Liang, S. Li, Q. Jiang, S. Tang, X. Chen, *Lithium Ion Battery Electrode Preventing Overcharging and Lithium Ion Battery*, **2016**, CN105552429A.

[268] M. S. Park, S. B. Ma, D. J. Lee, D. Im, S.-G. Doo, O. Yamamoto, *Sci. Rep.* **2014**, *4*, 3815.

[269] V. A. Rana, H. A. Chaube, *J. Mol. Liq.* **2012**, *173*, 71.

[270] F. Cataldo, *Eur. Chem. Bull.* **2015**, *4*, 92.

[271] W. L. Weng, *J. Chem. Eng. Data* **1999**, *44*, 788.

[272] BASF, *1,3-Dioxolane*, **2013**.

[273] S. Tang, H. Zhao, *RSC Adv.* **2014**, *4*, 11251.

[274] H. Moon, T. Mandai, R. Tatara, K. Ueno, A. Yamazaki, K. Yoshida, S. Seki, K. Dokko, M. Watanabe, *J. Phys. Chem. C* **2015**, *119*, 3957.

[275] T. R. Kubendran, *J. Chem. Eng. Data* **2004**, *49*, 421.

[276] M. Chiku, W. Tsujiwaki, E. Higuchi, H. Inoue, *Electrochemistry* **2012**, *80*, 740.

[277] J. Lopez, A. Pei, J. Y. Oh, G. J. N. Wang, Y. Cui, Z. Bao, *J. Am. Chem. Soc.* **2018**, *140*, 11735.

[278] H. Ogawa, A. Unemoto, I. Honma, *Electrochemistry* **2012**, *80*, 765.

[279] M. Baloch, A. Vizintin, R. K. Chellappan, J. Moskon, D. Shanmukaraj, R. Dedryvère, T. Rojo, R. Dominko, *J. Electrochem. Soc.* **2016**, *163*, A2390.

[280] Celgard LLC, **2009**.

[281] J. Landesfeind, J. Hattendorff, A. Ehrl, W. A. Wall, H. A. Gasteiger, *J. Electrochem. Soc.* **2016**, *163*, A1373.

[282] D. Lv, Y. Shao, T. Lozano, W. D. Bennett, G. L. Graff, B. Polzin, J. Zhang, M. H. Engelhard, N. T. Saenz, W. A. Henderson, P. Bhattacharya, J. Liu, J. Xiao, *Adv. Energy Mater.* **2015**, *5*, 1.

[283] T. Zhang, M. Marinescu, L. O'Neill, M. Wild, G. Offer, *Phys. Chem. Chem. Phys.* **2015**, *17*, 22581.

[284] J. Conder, R. Bouchet, S. Trabesinger, C. Marino, L. Gubler, C. Villevieille, *Nat. Energy* **2017**, *2*, 1.

[285] B. F. L. Lai, Y. Zou, D. E. Brooks, J. N. Kizhakkedathu, *Biomaterials* **2010**, *31*, 5749.

VITA

Dion D. Hubble was born in Tulsa, OK and graduated from Seven Lakes High School in Katy, TX. He performed undergraduate research under the direction of Prof. Partha Mukherjee from 2012-2014 before graduating Magna Cum Laude from Texas A&M University in 2014 with a Bachelor's of Science in Chemical Engineering. Soon afterwards, Dion moved to Seattle to enter the brand-new Molecular Engineering Ph.D. program at the University of Washington, becoming one of eight students in the first-ever cohort. He completed his Master's of Science in this program in 2016, followed by a Doctor of Philosophy in Molecular Engineering in 2019. He was the recipient of a National Defense Science and Engineering Graduate (NDSEG) Fellowship in 2016 and received an honorable mention for the National Science Foundation Graduate Research Fellowship Program (NSF GRFP) in the same year.

Dion has participated in various types of engineering research since 2012, ranging from chemical-enhanced oil recovery to silicon anodes with conjugated polymer binders, but over time has developed a passion for organic chemistry, energy storage, and the intersection of the two at a molecular scale. Under the advisorship of Prof. Alex Jen and project co-PI Prof. Jihui Yang, he successfully co-led an effort to acquire $1.25mil/3yr in grant funding for research into advanced Li-S battery designs. Following this, he established the Jen battery materials fabrication/testing laboratory from scratch and developed the many of the procedures used during this project. He has given several notable presentations, including an invited talk on this dissertation at Pacific Northwest National Laboratory in September 2019. At the time of this writing, he had authored or co-authored five peer-reviewed scientific publications. Dion is looking forward to what the future will bring and thanks you for reading this far.